

Quantifying the Cracking Behaviour of Strain Hardening Cement-based Composites

by

Pieter Daniel Nieuwoudt

Thesis presented for the degree of

Masters of Science in Engineering



At the Stellenbosch University

Supervisor:

Prof W.P. Boshoff

March 2012

DECLARATION

By submitting this thesis electronically, I declare that the entirety of the work contained therein is my own, original work, that I am the authorship owner thereof (unless to the extent explicitly otherwise stated) and that I have not previously in its entirety or in part submitted it for obtaining any qualification.

Signature:

Date: March 2012

Copyright © 2014 Stellenbosch University

All rights reserved

SUMMARY

Strain Hardening Cement Based Composite (SHCC) is a type of High Performance Fibre Reinforced Cement-based Composite (HPFRCC). SHCC contains randomly distributed short fibres which improve the ductility of the material and can resist the full tensile load at strains up to 5 %. When SHCC is subjected to tensile loading, fine multiple cracking occurs that portrays a pseudo strain hardening effect as a result. The multiple cracking is what sets SHCC aside from conventional Reinforced Concrete (RC). Conventional RC forms one large crack that results in durability problems. The multiple cracks of SHCC typically have an average crack width of less than 80 μm (Adendorff, 2009), resulting in an improved durability compared to conventional RC.

The aim of this research project is to quantify the cracking behaviour of SHCC which can be used to quantify the durability of SHCC. The cracking behaviour is described using a statistical distribution model, which represents the crack widths distribution and a mathematical expression that describes the crack pattern. The cracking behaviour was determined by measuring the cracks during quasi-static uni-axial tensile tests. The cracking data was collected with the aid of a non-contact surface strain measuring system, namely the ARAMIS system.

An investigation was performed on the crack measuring setup (ARAMIS) to define a crack definition that was used during the determination of the cracking behaviour of SHCC. Several different statistical distributions were considered to describe the distribution of the crack widths of SHCC. A mathematical expression named the Crack Proximity Index (*CPI*) which represents the distances of the cracks to each other was used to describe the crack pattern of SHCC.

The Gamma distribution was found to best represent the crack widths of SHCC. It was observed that different crack patterns can be found at the same tensile strain and that the *CPI* would differ even though the same crack width distribution was found. A statistical distribution model was therefore found to describe the *CPI* distribution of SHCC at different tensile strains and it was established that the Log-normal distribution best describes the *CPI* distribution of SHCC.

After the cracking behaviour of SHCC was determined for quasi-static tensile loading, an investigation was performed to compare it to the cracking behaviour under flexural loading. A difference in the crack widths, number of cracks and crack pattern was found between bending and tension. Therefore it was concluded that the cracking behaviour for SHCC is different under flexural loading than in tension.

OPSOMMING

“Strain Hardening Cement-based Composite” (SHCC) is ‘n tipe “High Performance Fibre Reinforced Cement-based Composite” (HPFRCC). SHCC bevat kort vesels wat ewekansig verspreid is, wat die duktiliteit van die material verbeter en dit kan die maksimum trekkrag weerstaan tot en met ‘n vervorming van 5 %. Wanneer SHCC belas word met ‘n trekkrag, vorm verskeie fyn krake wat ‘n sogenaamde vervormingsverharding voorstel. Die verskeie krake onderskei SHCC van normale bewapende beton. Normale bewapende beton vorm een groot kraak met die gevolg dat duursaamheidsprobleme ontstaan. Die gemiddelde kraakwydte van SHCC is minder as 80 μm (Adendorff, 2009) en het dus ‘n beter duursaamheid as normale bewapende beton.

Die doel van die navorsingsprojek is om die kraak gedrag van SHCC te kwantifiseer en wat dan gebruik kan word om die duursaamheid van SHCC te kwantifiseer. Die kraak gedrag is beskryf deur ‘n statistiese verspreiding model wat die kraak wydtes se verspreiding voorstel en ‘n wiskundige uitdrukking wat die kraak patroon beskryf. Die kraak gedrag was bepaal deur die krake te meet tydens die semi-statische een-asige trek toetse. Die kraak data was met behulp van ‘n optiese vervormings toestel, naamlik die ARAMIS, versamel.

‘n Ondersoek is gedoen op die kraak meetings opstelling (ARAMIS), om ‘n kraak definisie te definieer wat gebruik is om die kraak gedrag te bepaal. Daar is gekyk na verskeie statistiese verdelings om die kraak wydtes van SHCC te beskryf. Die kraak patroon van SHCC is beskryf met ‘n wiskundige uitdrukking genoem die “Crack Proximity Index” (*CPI*) wat die krake se afstande van mekaar voorstel.

Dit is bevind dat die Gamma verdeling die kraak wydtes van SHCC die beste beskryf. Daar is waargeneem dat verskillende kraak patrone by dieselfde vervorming verkry kan word en dat die *CPI* kan verskil al is die kraak wydte verdeling dieselfde. ‘n Statistiese verdelingsmodel is dus gevind om die *CPI* verdeling van SHCC te beskryf by verskillende vervormings, en daar is vasgestel dat die Log-normaal verdeling die *CPI* verdeling van SHCC die beste beskryf.

Nadat die kraak gedrag van SHCC bepaal is vir semi-statische trek-belasting, is ‘n ondersoek gedoen waar die trek-kraak gedrag vergelyk is met buig-kraak gedrag. ‘n Verskil in die kraak

wydtes, aantal krake en kraak patroon is gevind tussen buiging en trek. Dus is die gevolgtrekking gemaak dat die kraak gedrag van SHCC verskillend is in buiging as in trek.

ACKNOWLEDGMENTS

I would like to thank the following people for their assistance and support,

- Prof W.P. Boshoff, my study leader, for his guidance. His broad knowledge on Strain Hardening Cement-based Composites helped me to understand the concepts and the identification of problems.
- My parents and friends for their continuous support throughout this thesis.
- The staff of the laboratory of the Civil Engineering Department at the University of Stellenbosch for their help and understanding on the experimental work.

Table of Contents

CHAPTER 1	INTRODUCTION.....	1
1.1	Background	1
1.2	Aim and Scope	3
1.3	Outline of Contents	3
CHAPTER 2	LITERATURE STUDY.....	5
2.1	Strain Hardening Cement-Based Composites.....	5
2.1.1	Background and Constituents of SHCC	5
2.1.2	Material Behaviour of SHCC.....	6
2.1.3	Cracking Behaviour	10
2.2	Statistics	12
2.2.1	Statistical tools and methods of statistical analysis	12
2.2.2	Statistical distributions.....	16
2.2.3	Methods to Estimate the Adequacy and Accuracy	20
CHAPTER 3	INVESTIGATION OF CRACK MEASUREMENT SETUP	23
3.1	Crack Measurement Setup	23
3.2	Research Program	27
3.3	Specimen Preparation.....	27
3.4	Test Setup.....	33
3.5	Experimental Test Program.....	34
3.6	Evaluation of Crack Width.....	35
3.7	Results	37
3.8	Discussion	41
CHAPTER 4	QUANTIFYING THE CRACKING BEHAVIOUR OF SHCC.....	43

4.1	Research Program	43
4.1.1	Stochastic Description of the Crack Width Distribution	43
4.1.2	Mathematical Description of the Crack Pattern.....	44
4.2	Experimental Test Program.....	44
4.2.1	Stochastic Description of the Crack Width Distribution	45
4.2.2	Mathematical Description of the Crack Pattern.....	45
4.3	Results	45
4.3.1	Experimental results.....	45
4.3.2	Stochastic Description of the Crack Width Distribution	50
4.3.3	Mathematical Description of the Crack Pattern.....	53
4.4	Discussion	60
CHAPTER 5 APPLICATION OF QUASI-STATIC TENSILE MODELS ON BENDING		
	62	
5.1	Test Setup.....	62
5.2	Experimental Test Program.....	65
5.3	Results	66
5.4	Bending Cracking Behaviour vs. Tensile Cracking Behaviour	66
5.5	Bending Crack Pattern vs. Tensile Crack Pattern	70
5.6	Discussion	71
CHAPTER 6 CONCLUSIONS AND FUTURE DEVELOPMENTS.....		74
6.1	Conclusions	74
6.2	Future Developments	75
CHAPTER 7 REFERENCES.....		76
APPENDIX A MIX DESIGN.....		78
APPENDIX B THE CRACKING BEHAVIOUR DATA OF QUASI-STATIC TENSILE TESTS.....		82
APPENDIX C FOUR POINT BENDING RESULTS.....		98

NOMENCLATURE

a	Lower bound value of Beta distribution
α	The skewness of a distribution
α	Auxiliary parameter for Gamma distribution
b	Upper bound of Beta distribution
$B(c,d)$	Beta function for parameters c and d
β	Auxiliary parameter for Gamma distribution
c	Shape parameter for Beta distribution
C	Complementary energy
CWD_f	Crack Width Distribution function
C_{wi}	Crack width for a certain crack i
CP_i	Crack Proximity for a certain crack i relative to the other cracks j
d	Shape parameter for Beta distribution
d	Consecutive distances from the crack i to the other cracks j
δ	Displacement
δ_p	Critical crack opening in the σ - δ curve
δ_m	Griffith crack middle opening width
δ_{ss}	Steady-state crack width
ε_1	Tensile strain at the first crack
ε_{ult}	Ultimate tensile strain
ε_m	The tensile strain at which crack saturation took place
g	Auxiliary parameter in lower and upper bounds of Beta distribution
J_{tip}	Crack tip toughness
$\Gamma(\alpha)$	Gamma function of the parameter α
μ	The mean of a distribution
$P(X \leq x)$	The probability that a random variable X will be less or equal to x
ν	The coefficient of variation

n	The number of cracks
N	Sample size
R^2	The coefficient of determination
S	Sample space
SS_E	Error sum of squares
SS_T	Total corrected sum of squares
σ	The stress
σ	The standard deviation of a distribution
σ^2	The variance of a distribution
σ_{ult}	The ultimate strength
σ_1	The first cracking strength
σ_{cu}	The peak stress in the σ - δ curve
σ_{ss}	The steady-state cracking stress
U	Standardised random variable
$\varphi(x)$	The probability density function
$\Phi(x)$	The distribution function
x	The assigned value to the random variable X
X	Random variable X
y_i	Observed values out of the sample distribution
\hat{y}_i	Theoretical values calculated out of the statistical distribution model
CPI	Crack Proximity Index
PVA	Polyvinyl Alcohol
$SHCC$	Strain Hardening Cement-based Composites

CHAPTER 1

INTRODUCTION

1.1 Background

Concrete, due to its ability to be cast into any shape or size and its durability, is the most widely used construction material for structures. Concrete has a relatively high compressive strength compared to other building materials and has a low tensile strength of about one tenth of its compression strength. In concrete structures where the concrete is subjected to tensile loading, steel reinforcement is used to compensate for its low tensile strength. During the use of concrete cracking still occurs in the tensile regions, even with the use of steel reinforcement. These cracks lead to durability problems because they can act as path ways allowing water and gaseous substances to penetrate the concrete. These substances lead to corrosion of the steel reinforcement, which in turn leads to structural degradation.

Advanced concrete technology has lead to the development of a new cement-based composite by the addition of fibres. Strain Hardening Cement-based Composites (SHCC) is part of the High Performance Fibre Reinforced Cement-based Composites (HPFRCC) group and was developed to overcome the weaknesses of conventional Reinforced Concrete (RC). SHCC shows high ductility, has a high tensile strength and can withstand a full tensile load up to a strain of 5 %, whereas conventional concrete can only withstand a full tensile load up to an average strain of 0.015 %. SHCC undergoes strain hardening and during this phase closely spaced micro cracks form. These multiple micro cracks may reduce the problem of water and gaseous substances penetrating the material thus improving the durability of structures. This improvement in the durability of SHCC is justified by the reduction in the permeability (Lepech & Li, 2009). Lepech and Li (2009) showed that for cracked SHCC strained to 1.5 %, the permeability was nearly five orders of magnitude smaller than similarly strained conventional reinforced concrete. The permeability of cracked SHCC strained up to 3 % did

not change significantly for uni-axial tension. There was also no significant change in the permeability between cracked and un-cracked SHCC.

SHCC is more costly than conventional concrete, but because of its improved durability it will be more economical during its service life time (Lepech & Li, 2009). SHCC has many advantages over conventional concrete. Some of the advantages are improved ductility, higher tensile strength (Lin & Li, 1997) and self healing of the multiple cracks (Lepech & Li, 2009). These advantages of SHCC need to be exploited and further developed. Because of the improved ductility of SHCC, it can be used as a construction material for buildings in areas which are subjected to earth quake loadings and it can be used as a repair material. Where SHCC is used as a repair material, the large localised crack is replaced with multiple small micro cracks, which improves the durability and the service life time of the structure (Lepech & Li, 2009).

Recent research has been done on SHCC to describe its mechanical behaviour (Silva et al., 2010), time-dependant behaviour and tensile creep behaviour (Boshoff, 2007), but little work has been done to quantify the durability of SHCC based on the crack patterns. Boshoff and Adendorff (2010) presented a method to quantify the durability of SHCC for specific loading conditions and mentioned that further development and investigation needs to be done in:

- The quantification of the cracking behaviour of SHCC.
- The effect that the multiple cracks has on the permeability of SHCC.

These two topics need to be linked to each other and can then be used to quantify the durability of SHCC.

The cracking behaviour of SHCC is characterised by a statistical distribution model which describes the distribution of the crack widths of SHCC and provides a mathematical expression that quantifies the crack pattern. Boshoff and Adendorff (2010) stated that, although the average crack width is below a certain threshold where no penetration of substances can take place, it is probable that some of the cracks are larger than the threshold where substance can penetrate the material. Thus a statistical distribution is needed to describe the distribution of the crack widths of SHCC. The method of using the maximum crack width is also inadequate because the probability of finding a larger crack width increases when observing a larger area of cracks. It has been shown that the crack pattern has

an effect on the durability of cement-based composites (Kato et al., 2005) and is thus an important characteristic when quantifying the cracking behaviour of SHCC.

1.2 Aim and Scope

The aim of this research project is to find a statistical distribution model which best describes the distribution of the crack widths and to find a mathematical expression that quantifies the crack pattern of SHCC. The tests that were conducted to collect cracking data were quasi-static uni-axial tensile tests. A non-contact surface strain measuring system called ARAMIS was used to collect the data. Different statistical tools and methods were applied to find the most effective statistical distribution out of a chosen group of statistical distributions to describe the distribution of the crack widths of SHCC.

An investigation was also performed to compare the cracking behaviour under tensile loading in relation to the cracking behaviour under flexural loading. This was done to verify whether the cracking behaviour under tensile loading is similar to the cracking behaviour under flexural loading.

The results determined from this research project can be used in cooperation with other future research topics that precede the discipline of quantifying the durability of SHCC, to help create a model which can be used to quantify the durability of a structure.

1.3 Outline of Contents

Chapter 2 gives a short summary into the background of the development of SHCC. It describes the behaviour of SHCC on different material levels in order to explain the mechanisms behind the cracking behaviour. It also gives a description into the statistical tools and methods used to find the statistical distribution which best describes the distribution of the crack widths.

In Chapter 3 an investigation is done into the crack measuring test setup called the ARAMIS. In this chapter a crack definition used to calculate the crack widths from the ARAMIS data collected during the experimental tests is defined.

In Chapter 4 the cracking behaviour of SHCC is quantified. First some descriptive statistical parameters are quantified and then by applying statistical tools and methods, a statistical distribution model is presented to describe the distribution of the crack widths. A mathematical expression is also presented to quantify the crack pattern in this chapter.

In Chapter 5 the statistical distribution model presented in Chapter 4 under quasi-static tensile loading, is applied to bending. The crack pattern of the flexural loading is compared to the crack pattern of the tensile loading that is quantified in Chapter 4. The reason why the cracking behaviour under tensile loading is compared to the cracking behaviour under flexural loading is to verify whether the cracking behaviours are similar in tension to that in bending.

In Chapter 6 a brief summary of the conclusions that are made in this research project are given. Also given in this chapter are points that can be exploited in future research to help developed and improve the use of SHCC.

CHAPTER 2

LITERATURE STUDY

2.1 Strain Hardening Cement-Based Composites

This section gives a background study of SHCC and its constituents, by looking at the material behaviour on different material levels and to explain the mechanisms behind the cracking behaviour. A background study is also given on research that has been recently done on the cracking behaviour.

2.1.1 Background and Constituents of SHCC

SHCC development began in the early 1990's and because of its high ductility was first used as a repair material (Li et al., 2000). Throughout the years SHCC has developed significantly and is now considered part of the High Performance Fibre Reinforced Cement-based Composites (HPFRCC) family. With a fibre content of approximately 2 % by volume the average crack width of SHCC can be limited to less than 80 μm during quasi-static tensile tests (Adendorff et al., 2010). The high ductility of SHCC is due to the phase of multiple cracking that occurs. The ability of SHCC to limit the crack widths below a certain threshold reduces the ingress of water and gaseous substances (Lepech & Li, 2009) that improves the durability of the structure.

SHCC contains the following constituents: cement, fly ash, aggregates, water and Polyvinyl Alcohol (PVA) fibres. Super Plasticiser and a Viscosity Modification Agent are added to obtain the correct workability. The constituents and type are summarised in Table 2.1. The fibres added make up 2 % of the total volume of the mixture and the strain hardening response is dependent on the correct proportions of the constituents. It is important that the

right mix proportions of local constituents must be established in order to get a good strain hardening response as the author has established that there is a high variability in strength and strain capacity and composite performance if the same mix proportions are applied in different research groups.

Table 2.1: SHCC constituents defined by type as used in this research.

Constituents	Type
Cement	CEM I 42.5N
Fly Ash	-
Sand	Silica sand; Partical size < 300 μm
Water	-
Fibres	PVA-RECS 15; Length = 12 mm; Diameter = 40 μm
Viscous Modification Agent	Aqua Beton; from Chryso
Super Plasticiser	Premia 310; from Chryso

2.1.2 Material Behaviour of SHCC

In order to explain the material behaviour of SHCC, it is studied at different material levels, namely Macroscopic, Single Crack and Microscopic Level.

2.1.2.1 Macroscopic Level

SHCC is a ductile cement-based composite which exhibits strain hardening after the first crack appears and is found that the stress increases as the strain increases (Li et al., 2001) as shown in Figure 2.1. In Figure 2.1 it can clearly be seen that the tensile stress-strain curve exists out of three phases. The first phase is the linear elastic phase which represents the material behaviour of the cement-based matrix before cracking. During this phase the fibres have little effect on the tensile strength of the material. The second phase is the strain hardening phase and during this phase multiple cracks are formed. The third phase is the tensile softening phase. At this phase the material starts to fail as the result of the localisation of one or more cracks. Failure of the specimen can take place because of fibre pullout or fibre

rupture; these two phenomenons are explained in Sections 2.1.2.2 and 2.1.2.3. An ultimate strain capacity of 4 % or more can be reached before failure (Mechtcherine et al., 2007). The second phase is what sets SHCC apart from ordinary concrete and even normal FRC (Fibre Reinforced Concrete).

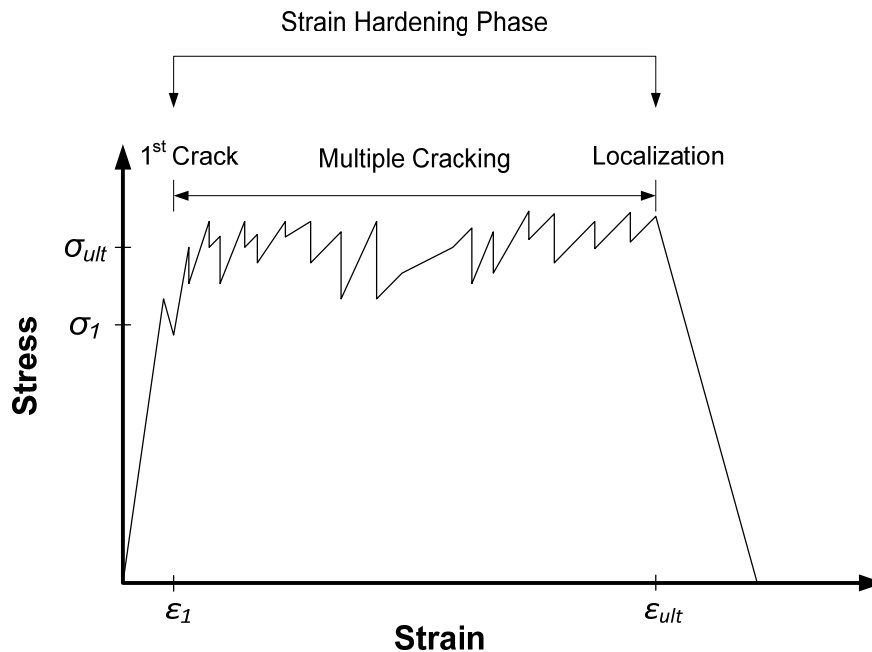


Figure 2.1: Tensile stress-strain graph illustration of SHCC.

Ordinary concrete localises with one large crack and has no ductility. Although FRC shows some ductility, no multiple cracking takes place. Phase two is important to quantify the cracking behaviour of SHCC. It should be kept in mind that for different tensile strain rates, different cracking behaviours are found (Adendorff et al., 2010). This will be discussed in Section 2.1.2.3.

For multiple cracking to occur there are two requirements (Lin & Li, 1997). The first requirement is that the crack bridging stress of the fibres must be more than the matrix cracking strength. The second requirement is that Steady-state cracking must occur; this will be explained in Section 2.1.2.2. The matrix will crack at the weakest point when subjected to tensile loading. The first crack will be bridged by the fibres and will happen at a tensile stress of σ_1 and tensile strain of ϵ_1 as shown in Figure 2.1. As the strain increases the stress increases until the 2nd crack forms, and the fibres will bridge the 2nd crack. If this process continues, multiple cracking will take place until a point is reached where the load is more

than the crack bridging stress of the fibres. This will happen at a tensile stress of σ_{ult} and a tensile strain of ε_{ult} as shown in Figure 2.1. At this point a localised crack will form and as the strain increases the stress decreases. For multiple cracking to occur the following requirement must be fulfilled.

$$\sigma_1 \leq \sigma_{ult} \quad \text{Eq. 2.1}$$

Equation 2.1 states that for multiple cracking to occur the ultimate strength of SHCC must be larger than the first cracking strength, with σ_1 the first cracking strength and σ_{ult} the ultimate strength of SHCC.

2.1.2.2 Single Crack Level

As mentioned in the previous section for multiple cracking to occur two requirements must be fulfilled. The second and more important requirement is that Steady-state cracking must occur. In fact if the second requirement is fulfilled the first requirement is also normally fulfilled (Li, 2003). Li (2003) also stated that the most fundamental property of developing SHCC is the fibre bridging property, generally referred to as the stress versus crack opening (σ - δ) relation, shown in Figure 2.2. To understand the property strain-hardening of SHCC, the roles of the fibres during crack bridging need to be recognised. During crack bridging the fibres play a load bearing and energy absorption role. Steady-state cracking is part of the energy absorption role that the fibres play during crack bridging. The hatched area marked as C in Figure 2.2 indicates the complementary energy of SHCC under tensile loading. The complementary energy is related to the strain-hardening properties of SHCC (Li, 2003).

When the fibre/matrix bond is too weak fibre pullout will occur resulting in the failure of the material and an σ - δ curve with a low peak strength σ_{cu} . When the fibre/matrix bond is too strong the fibres cannot slip and will result in fibre rupture with a small value of critical opening δ_p . In both these cases the complementary energy will be small in comparison to the tip toughness J_{tip} ; the energy needed from the matrix crack toughness to resist the bridged crack (Li, 2003). In Figure 2.2 the shaded area indicates J_{tip} . The crack will therefore have no bridging properties where fibre rupture took place and where fibre rupture did not take place the fibres will thus have to carry more stress, as the result of the fibres that ruptured. This happens in the widest part of the crack where the maximum opening δ_m exceeds δ_p , see Figure 2.3 a). Ultimately this will result in the rest of the fibres rupturing and total failure. This type

of crack development is called a Griffith Crack and is shown in Figure 2.3 a). If the complementary energy is large in comparison to the tip toughness, the Steady-state Crack opening δ_{ss} will remain smaller than δ_p and the crack will remain flat as it propagates, see Figures 2.2 and 2.3 b). This type of crack development will lead to Steady-state Cracking, which means multiple cracking will occur. Figure 2.3 b) demonstrates a Steady-state Flat Crack.

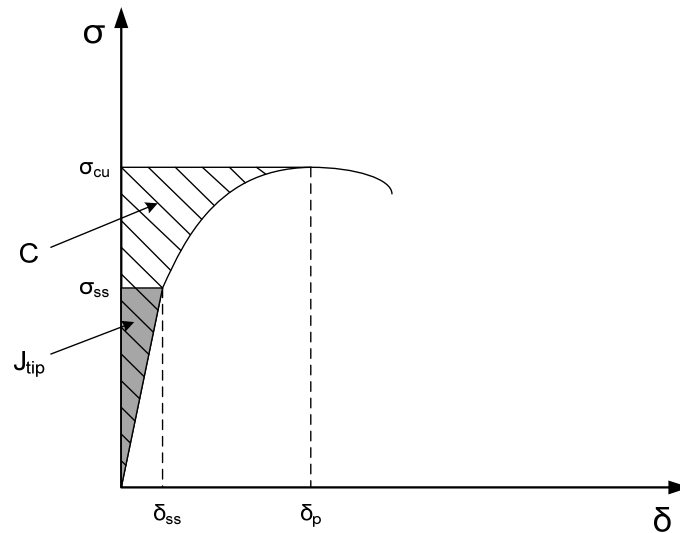


Figure 2.2: The σ - δ curve. The hatched area marked as C represents the complementary energy (Li, 2003).

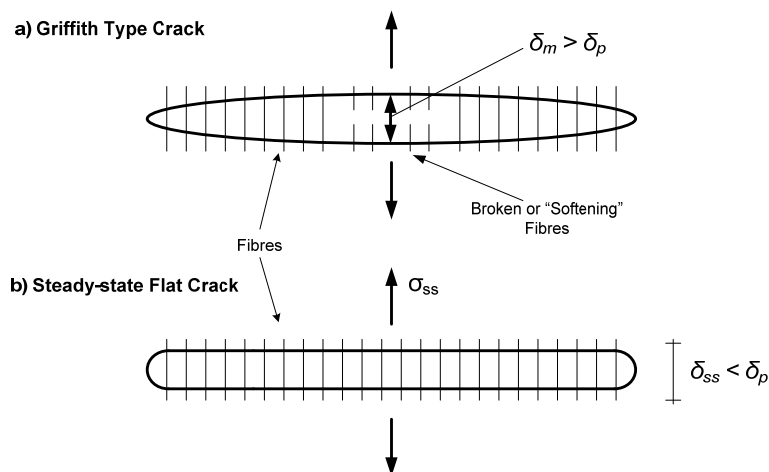


Figure 2.3: Steady state crack analysis (Li, 2003). a) Griffith Type Crack. b) Steady-state Flat Crack.

Fibre length, strength, volume of total mix and the fibre/matrix bond are all parameters that determine the shape of the σ - δ curve. The PVA fibres typically used today are tailored so that the energy criteria will be satisfied in the fibre/matrix bond.

2.1.2.3 Microscopic Level

The Microscopic Level explains the meaning of a single fibre in the matrix. The fibres used in this research project are PVA (Polyvinyl Alcohol) fibres. The fibres have a diameter of 40 μm and a length of 12 mm. Their tensile strength and stiffness are 1560 MPa and 40 GPa respectively. Boshoff (2007) showed that the tensile strength of the fibres decreases when the fibres are embedded in the matrix. This is due to the surface damage that takes place to the fibres when pulled out of the matrix and it is this damage that causes the slip hardening effect to take place. The slip hardening effect is a phenomenon that takes place when the fibre is pulled out of the matrix, causing strips of the fibre to come off the fibre (Lin & Li, 1997). These strips get stuck between the fibre and the matrix causing the frictional resistance to increase. Boshoff (2007) also showed that the probability of fibre rupture increased as the pull out rate increased and with longer embedment lengths. This explains the reason why different cracking behaviours are found at different tensile strain rates. Strain hardening takes place when the fibres do not rupture but rather when fibre slippage takes place. Boshoff (2007) indicated that for an embedment length larger than 1.4 mm fibre rupture will take place during the fibre pull out test. For fibre slippage to take place the bond between the fibre and the matrix needs to be broken. PVA fibres are tailored so that fibre slippage will take place and produce strain hardening in cement-based materials. For more information on the fibre pull out test refer to Boshoff (2007).

2.1.3 Cracking Behaviour

As mentioned before, Phase Two in the stress-strain graph shown in Figure 2.1 is important in quantifying the cracking behaviour of SHCC, because this is where multiple cracking takes place. Li (1992) indicated that the strain-hardening phase has two separate phases, as indicated in Figure 2.4. Region I on the stress-strain graph is where multiple cracks form. Region II is where crack saturation has taken place and as the stress increases the existing

cracks widen. Li (1992) suggested that for design purposes the strain should be limited to ϵ_m , as defined in Figure 2.4.

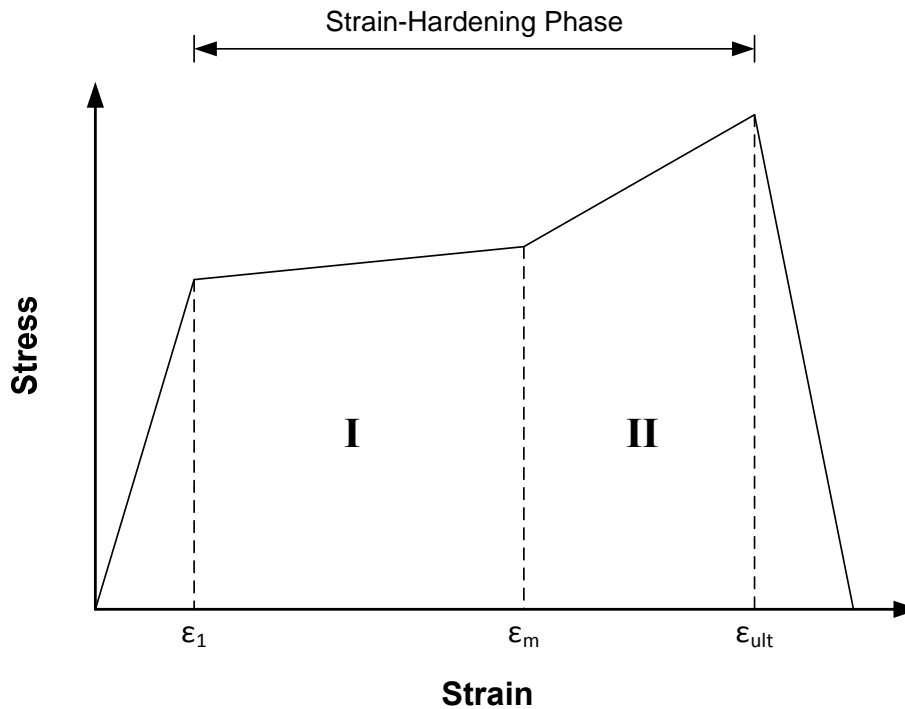


Figure 2.4: Tensile response of FRCC (Li, 1992).

Boshoff (2007) conducted rate dependant tensile tests on dogbone specimens and found that the first cracking strength increases as the strain rate increases, especially when the strain rates are close to dynamic strain rates. However the ultimate tensile stress remained fairly steady as the strain rate increased. Boshoff (2007) explained that the difference between these trends was attributed to two different mechanisms that controlled these values. The first cracking strength is dependent on the cement-based matrix strength which is rate dependant. The ultimate cracking strength is dependent on fibre strength which in turn is rate dependant as described in Section 2.1.2.3 as well as the fibre matrix interface. In addition Boshoff (2007) also found that the strain rate has no effect on the ductility and the E-modulus, but that the strain rate did have an effect on the crack spacing. Boshoff (2007) showed that the crack spacing increases as the tensile strain rate increases.

Adendorff (2009) described the cracking behaviour of SHCC in terms of the average crack width, number of cracks and some descriptive statistical properties. He described the cracking behaviour for two types of loading conditions, quasi-static uni-axial tensile tests and for sustained tensile tests. He also showed that for uni-axial tensile loading the average crack width did not differ significantly for different loading rates; however the number of cracks increased significantly, thus for the average crack width to remain the same, the number of cracks needed to increase. The average crack width under uni-axial tensile tests remained below 80 μm for five different strain rates, ranging from 0.00001/s to 0.1/s, (Adendorff, 2009). However, under sustained loading tests Adendorff (2009) showed that the average crack increased significantly after a certain time, at this point the number of cracks stabilised, which means no new cracks were formed but that the existing cracks widened. In these tests the average crack width for sustained loading remained below 300 μm whilst the loading varied from 40 % - 80 % of the ultimate tensile stress. From the above it can be deduced that the cracking behaviour differs under different loading conditions. In this research project the cracking behaviour for uni-axial tensile loading will be quantified.

2.2 Statistics

This section gives a description of the statistical parameters and continuous distribution models that were used to quantify the cracking behaviour of SHCC. The continuous distribution models that are used in this research project were selected because they are the most frequently used distribution models in this type of research and therefore are the most appropriate to analyse the cracking data. A description is given on how to select which distribution model from the chosen group of distributions is the most suitable to describe the observed values. Also given is a description on how to check the accuracy of this model.

2.2.1 Statistical tools and methods of statistical analysis

In this section a general overview of descriptive statistics is given. When an experiment is conducted the outcome of the results that are measured can differ slightly, no matter how accurate the experiment is designed and conducted. It should be noted that the variations in the experiments that were conducted are due to the variations in the material used and not in

the measuring setup. These experiments are said to include a random component and it can thus be said that an experiment can have different results every time the same experiment is repeated; such an experiment is called a random experiment (Montgomery & Runger, 2007) and (Holicky, 2009). The set of possible outcomes of a random experiment is called the sample space of the experiment, denoted as S . There are two types of sample spaces, namely discrete sample spaces and continuous sample spaces. A sample space is discrete if the set of outcomes is finite or countable infinite, and a sample space is continuous if it contains any value of a given interval or domain. Because the values of the outcome of a random experiment are not known in advance the outcomes are referred to as random variables. Thus a random variable X is defined as a variable which assigns a value x to each outcome in the sample space of a random experiment, which is unknown in advance. The total of all the possible outcomes of a random variable X is called a population and is described by a distribution which determines the probability that a random variable X attains a given set of values. The distribution function $\Phi(x)$ is the probability that a random variable X will be less than or equal to x , thus

$$\Phi(x) = P(X \leq x) \quad \text{Eq. 2.2}$$

The probability density function $\varphi(x)$ of a continuous random variable x is the derivative of the distribution function.

$$\varphi(x) = \frac{d\Phi(x)}{dx} \quad \text{Eq. 2.3}$$

Equations 2.2 and 2.3 define the distribution function $\Phi(x)$ and the probability density function $\varphi(x)$. The general property of the probability density function $\varphi(x)$ is that the integral over its full interval equals to 1.

The random variable X can also be described by various parameters namely the mean, standard deviation, skewness and kurtosis. These parameters are the so-called moment parameters. The mean also called the expected value or average (μ) is defined as the first moment about the origin, expressed as follows:

$$\mu = \int x\varphi(x)dx \quad \text{Eq. 2.4}$$

The mean corresponds with the x coordinate of the centre of gravity of the surface surrounded by the horizontal axis x and the probability density function $\varphi(x)$. The mean of a sample with size N can be determined as follows:

$$\mu = \frac{1}{N} \sum_i x_i \quad \text{Eq. 2.5}$$

The variance (σ^2) is a measure of dispersion of a random variable X relative to the mean and is given by the second central moment, expressed as follows:

$$\sigma^2 = \int (x - \mu)^2 \varphi(x) dx \quad \text{Eq. 2.6}$$

The variance of a sample with size N can be determined as follows:

$$\sigma^2 = \frac{1}{N-1} \sum_i (x_i - \mu)^2 \quad \text{Eq. 2.7}$$

The standard deviation (σ) is the square root of the variance, $\sqrt{\sigma^2} = \sigma$.

The third central moment is the measuring of asymmetry or skewness (α) of a population and is expressed as follows:

$$\alpha = \frac{1}{\sigma^3} \int (x - \mu)^3 \varphi(x) dx \quad \text{Eq. 2.8}$$

The skewness for a sample with size N can be determined as follows:

$$\alpha = \frac{N}{(N-1)(N-2)\sigma^3} \sum_i (x_i - \mu)^3 \quad \text{Eq. 2.9}$$

When the skewness is positive the distribution is said to be skewed to the right which means that the peak of the distribution is to the left and the tail of the distribution is to the right. When the skewness is negative the distribution is said to be skewed to the left which means that the peak of the distribution is to the right and the tail of the distribution is to the left. Figure 2.5 demonstrates a distribution skewed to the right and a distribution skewed to the left.

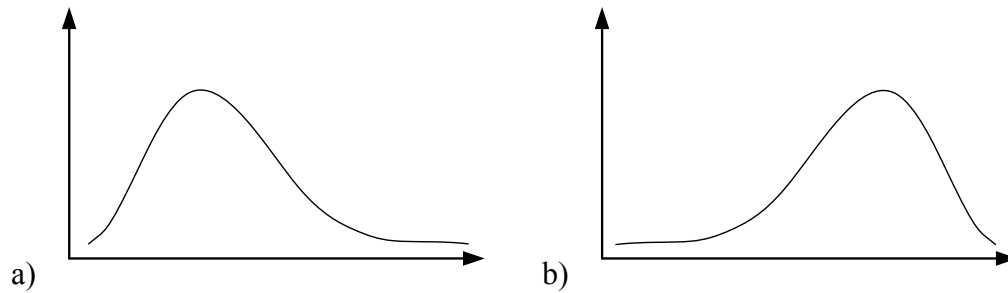


Figure 2.5: a) A distribution skewed to the right (positive skewness). b) A distribution skewed to the left (negative skewness).

If the value of the skewness is less than -1 or greater than +1, then the distribution is highly skewed. If the skewness value is between -1 and -0.5 or +0.5 and +1, then the distribution is moderately skewed and if the skewness value is between -0.5 and +0.5, then the distribution is said to be approximately symmetric, (Bulmer, 1965). It should be emphasised that the skewness is sensitive to extreme deviations ($x_i - \mu$) and may easily be affected by outliers. Holicky (2009) suggests that a sample size of $N > 30$ should be used for estimating the skewness of a population. For sample sizes smaller than 30, the estimation of the skewness would not be that accurate.

The kurtosis (ε) is the measurement of steepness or the concentration of values around the mean and is given by the fourth central moment, expressed as follows:

$$\varepsilon = \frac{1}{\sigma^4} \int (x - \mu)^4 \varphi(x) dx - 3 \quad \text{Eq. 2.10}$$

The kurtosis for a sample with size N can be determined as follows:

$$\varepsilon = \frac{N(N+1)}{(N-1)(N-2)(N-3)\sigma^4} \sum_i (x_i - \mu)^4 - 3 \frac{(N-1)^2}{(N-2)(N-3)} \quad \text{Eq. 2.11}$$

The kurtosis is rarely used, because the kurtosis is significantly affected by outliers (Holicky, 2009). As the kurtosis was not needed to describe the cracking behaviour of SHCC and due to its sensitivity to outliers the kurtosis was not included in this research project.

Another dimensionless parameter describing a particular characteristic which is used to measure the relative dispersion is the coefficient of variation. The coefficient of variation is the ratio of the standard deviation to the mean given as follows:

$$v = \frac{\sigma}{\mu} \quad \text{Eq. 2.12}$$

The parameters described above are used in this research to analyse the sample data to determine the shape and scale parameters for the different statistical distributions for each test.

2.2.2 Statistical distributions

This section provides a description of the most important statistical distribution models used. The Beta distribution will also be explained here although the results were not included in this research project. The reason for this being omitted is that a divergence in the shape parameters and limit parameters were found, which led to inaccurate results.

2.2.2.1 Normal distribution

The Normal distribution, also called the Laplace-Gauss distribution, is the most widely used distribution model (Montgomery & Runger, 2007). The Normal distribution is a symmetrical distribution and the variable X is defined on an unlimited interval $-\infty < x < \infty$, which may not be suitable in certain applications. The Normal distribution is dependent on two parameters only, namely the mean (μ) and standard deviation (σ). This distribution is suitable for a symmetric random variable with a relatively low variance (for a coefficient of variation $v < 0.3$) but may fail for random variables that are asymmetric with a great variance and skewness $\alpha > 0.5$, which means that this distribution has a limited use for describing the cracking behaviour of SHCC. The probability density function for the Normal distribution with mean μ_X and standard deviation σ_X is as follows:

$$\varphi(x) = \frac{1}{\sigma_X \sqrt{2\pi}} \exp \left[-\frac{1}{2} \left(\frac{x - \mu_X}{\sigma_X} \right)^2 \right] \quad \text{Eq. 2.13}$$

The skewness and kurtosis defined by Equations 2.8 and 2.10 are zero for any Normal distribution. Sometimes the random variable X is standardized to a random variable U . The random variable U is derived from the actual variable X as follows:

$$U = \frac{X - \mu_X}{\sigma_X} \quad \text{Eq. 2.14}$$

In Equation 2.14 μ_X and σ_X denote the mean and standard deviation of the actual variable X . The mean (μ_U) and standard deviation (σ_U) of the random variable U is 0 and 1 respectively. The probability density function for a Normal distribution with standardized random variable U is as follows:

$$\varphi(u) = \frac{1}{\sqrt{2\pi}} \exp\left(-\frac{u^2}{2}\right) \quad \text{Eq. 2.15}$$

2.2.2.2 Log-normal distribution

The Log-normal distribution is an asymmetric distribution defined on a one-sided limited interval $x_0 < x < \infty$ or $-\infty < x < x_0$. The Normal distribution is defined on an unlimited interval which may not be suitable for some applications. The Log-normal distribution partly eliminates this problem with an upper or lower boundary x_0 . The Log-normal distribution is dependent on three parameters, namely the mean (μ_x), the standard deviation (σ_x) and the skewness (α_x) and is thus referred to as the three-parameter Log-normal distribution. When the skewness is unknown or uncertain, the lower or upper bounds x_0 can be used. In this research project the three parameter Log-normal distribution with a lower boundary was chosen, because of the sensitivity of the skewness to gross errors or outliers of the sample.

A random variable X has a Log-normal distribution if the transformed random variable Y given in Equation 2.16 has a Normal distribution.

$$Y = \ln |X - x_0| \quad \text{Eq. 2.16}$$

The probability density function for the three parameter Log-normal distribution with lower boundary at x_0 is as follows:

$$\varphi(x) = \frac{1}{(x-x_0)\sigma_y\sqrt{2\pi}} \exp\left[-\frac{(\ln(x-x_0)-\mu_y)^2}{2\sigma_y^2}\right] \quad \text{Eq. 2.17}$$

The mean μ_y and standard deviation σ_y can be calculated from the mean, standard deviation and the lower boundary of the sample.

2.2.2.3 Gamma distribution

The Gamma distribution is another type of one-sided limited distribution and is a special case of the Pearson's distribution of Type III with the lower boundary at zero. The probability density function of the Gamma distribution is dependent on two parameters, namely the mean (μ) and the standard deviation (σ). Two auxiliary parameters β and α are often used to simplify the notation. The probability density function for the Gamma distribution is as follows:

$$\varphi(x) = \frac{[x-x_0]^{\alpha-1}}{\beta^\alpha \Gamma(\alpha)} \exp\left[-\frac{(x-x_0)}{\beta}\right], \beta = \frac{\sigma^2}{\mu}, \alpha = \left(\frac{\mu}{\sigma}\right)^2 \quad \text{Eq. 2.18}$$

The two parameters β and α are often called the scale and shape parameters, respectively. In Equation 2.18, $\Gamma(\alpha)$ is the Gamma function of the parameter α and is determined as follows:

$$\Gamma(\alpha) = \int_0^\infty x^{\alpha-1} e^{-x} dx, \text{ for } x > 0 \quad \text{Eq. 2.19}$$

The parameters β and α can be calculated from the first three moment parameters, or the mean, standard deviation and lower boundary x_0 can be used. When the parameters β and α were calculated the lower boundary was chosen over the skewness parameter.

2.2.2.4 Beta distribution

The Beta distribution, also called the Pearson's distribution of Type I, is defined on a two-sided interval $\langle a, b \rangle$. The Beta distribution has four parameters and is used in cases where the random variable is limited. The Beta distribution is difficult to apply because of the four

parameters that need to be determined from data which is not always available. The Beta distribution is usually written in the form as follows:

$$\varphi(x) = \frac{(x-a)^{c-1}(x-b)^{d-1}}{B(c,d)(b-a)^{c+d-1}} \quad \text{Eq. 2.20}$$

The parameters c and d are the so-called shape parameters and $B(c,d)$ is the Beta function and can be determined as follow:

$$c = \frac{\mu-a}{b-a} \left(\frac{(\mu-a)(b-\mu)}{\sigma^2} - 1 \right), d = \frac{b-\mu}{b-a} \left(\frac{(\mu-a)(b-\mu)}{\sigma^2} - 1 \right) \quad \text{Eq. 2.21}$$

$$B(c, d) = \frac{\Gamma(c)\Gamma(d)}{\Gamma(c+d)} \quad \text{Eq. 2.22}$$

The lower and upper bounds are given as:

$$a = \mu - cg\sigma, b = \mu + dg\sigma, g = \sqrt{\frac{c+d+1}{cd}} \quad \text{Eq. 2.23}$$

The parameter g is an auxiliary parameter to simplify the notations in Equation 2.23.

For application of the Beta distribution it is often convenient to use the Beta distribution with the lower bound $a = 0$. For this case the Beta distribution is defined if the skewness satisfies the condition as follows:

$$\alpha \leq 2\nu \quad \text{Eq. 2.24}$$

With ν defined in Equation 2.12. The input parameters are the mean (μ), standard deviation (σ) and skewness ($\alpha \leq 2\nu$). The upper limit with the lower bound $a = 0$ is given as:

$$b = \frac{\mu(c+d)}{c} \quad \text{Eq. 2.25}$$

In Equations 2.26 and 2.27 c and d are give as:

$$c = -\frac{\alpha (2\nu-\alpha)^2 - (4+\alpha^2)}{2\nu (\nu\alpha+2)^2 - (4+\alpha^2)} \quad \text{Eq. 2.26}$$

$$d = \frac{\alpha (2v-\alpha)^2 - (4+\alpha^2) 2+\alpha v}{2 (v\alpha+2)^2 - (4+\alpha^2) \alpha - 2v} \quad \text{Eq. 2.27}$$

If the skewness does not fulfil the condition in Equation 2.24, then a divergence in the parameters defined in Equations 2.25-2.27 are found. The Beta distribution was not included in the investigation of the cracking behaviour of SHCC, because it was found that the skewness for some sample tests did not fulfil the condition in Equation 2.24 which led to inaccurate results.

2.2.3 Methods to Estimate the Adequacy and Accuracy

In this section a description on how to check the accuracy and adequacy of a distribution model for a given set of observed values is given. The two methods that will be explained are the Quantile-Quantile plot and the Coefficient of Determination.

2.2.3.1 Quantile-Quantile plot

A Quantile-Quantile plot is where the observed values of a variable are plotted against theoretical quantiles, which is calculated out of a distribution model. The Quantile-Quantile plot is useful for finding the best fitting distribution within a chosen group of distributions. To evaluate whether the theoretical values calculated out of the distribution follow the same trend as the observed values, it is observed how the data points fall on the line, $y = x$. The theoretical distribution that best represents the observed values will best reproduce the line, $y = x$. Figure 2.6 shows two Quantile-Quantile plots for two different distributions for the same data. It can clearly be seen in Figure 2.6 that the Normal distribution is not an adequate probability distribution model for the observed values, but the Log-normal distribution is.

It is not always that easy to identify which distribution is the best distribution to represent the observed values, Figure 2.7 demonstrates this. Thus a different method is required which can quantitatively express which statistical distribution is an adequate model for the observed values. This method is explained in the next section.

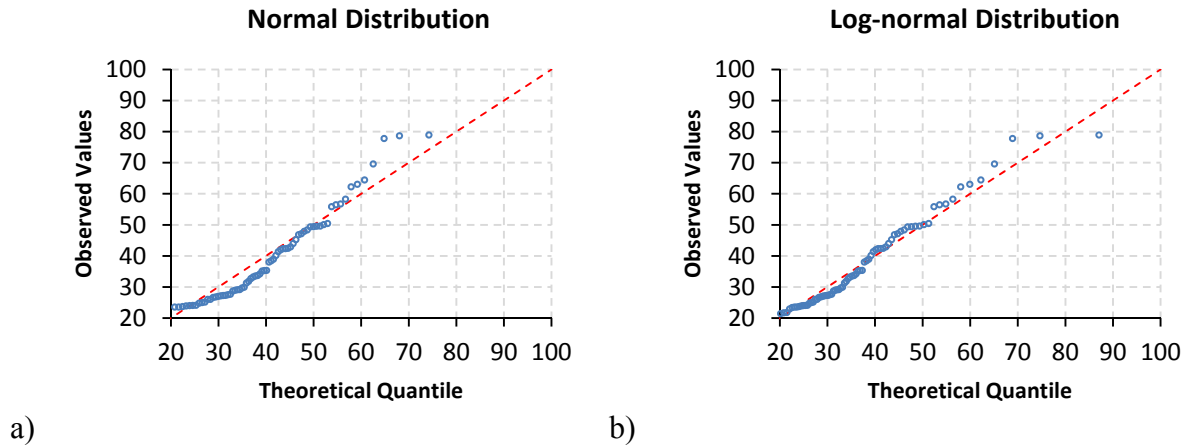


Figure 2.6: a) Quantile-Quantile plot for a normal distribution. b) Quantile-Quantile plot for a log-normal distribution.

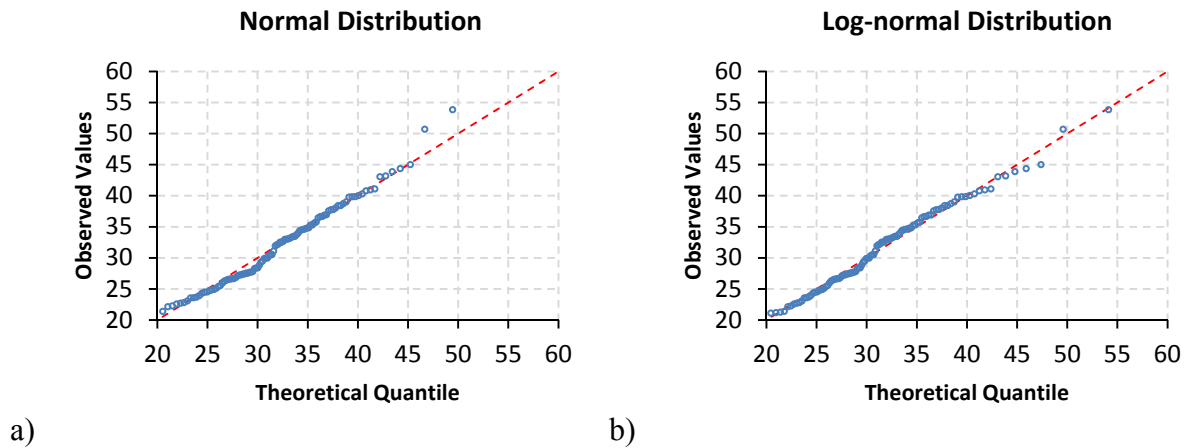


Figure 2.7: a) Quantile-Quantile plot for a normal distribution. b) Quantile-Quantile plot for a log-normal distribution.

2.2.3.2 Coefficient of Determination

The Coefficient of Determination is a method to quantitatively judge the adequacy of the distribution model. The Coefficient of Determination is the amount of variability in the data explained by the regression model. The Coefficient of Determination is determined as follow,

$$R^2 = 1 - \frac{SS_E}{SS_T} = 1 - \frac{\sum_{i=0}^n (y_i - \hat{y}_i)^2}{\sum_{i=0}^n (y_i - \bar{y})^2} \tag{Eq. 2.28}$$

Where y_i is the observed values out of the sample distribution and \hat{y}_i is the theoretical values calculated out of the distribution model. The term SS_E is the Error Sum of Squares and the term SS_T is the Total Corrected Sum of Squares of y . The Coefficient of Determination is defined on the interval, $0 \leq R^2 \leq 1$. The higher the value of R^2 the more adequate is the distribution model. In Figure 2.8 the same two Quantile-Quantile plots are shown as in Figure 2.7, but with the Coefficient of Determination.

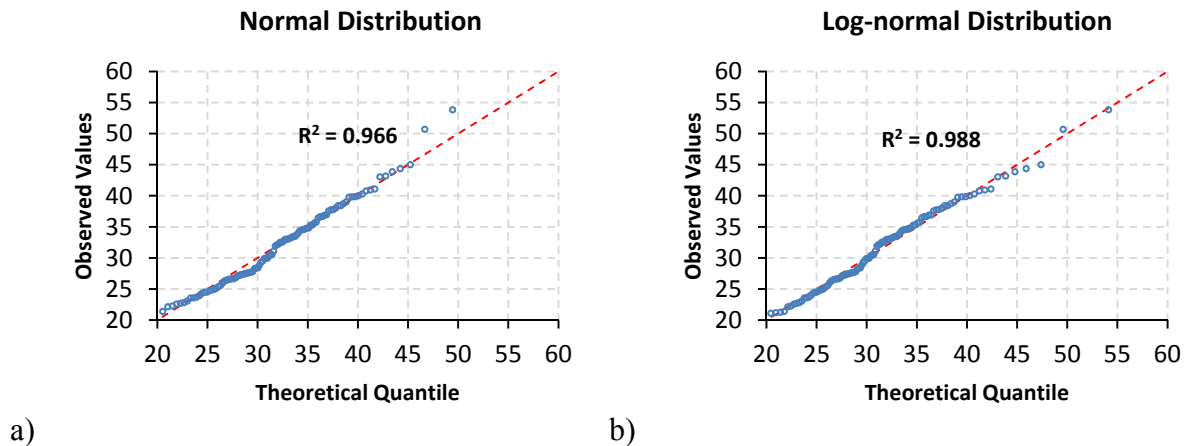


Figure 2.8: a) Quantile-Quantile plot for a normal distribution with R^2 b) Quantile-Quantile plot for a log-normal distribution with R^2 .

In Figure 2.7 it was difficult to see which distribution best represents the observed values, but the Coefficient of Determination (R^2) shows that the Log-normal distribution is the most suitable distribution based on the acceptance of the Coefficient of Determination concept. The only problem with the Coefficient of Determination is that it does not give an indication of which values are over or under estimated. This can easily be seen on the Quantile-Quantile plots.

CHAPTER 3

INVESTIGATION OF CRACK

MEASUREMENT SETUP

There are a few methods that can be used to determine the number of cracks and crack widths of SHCC. Digital Image Correlation and Digital Image Processing are two methods that are known that can be used to collect cracking data for SHCC. The method used to collect cracking data in this research project was Digital Image Correlation. An investigation was performed on the Crack Measurement Setup to determine how accurate the setup calculates the number of cracks and crack widths on the test specimens.

3.1 Crack Measurement Setup

Because SHCC undergoes multiple cracking it is a difficult task to measure the crack widths. The method used for this research project was non-contact Digital Image Correlation. A few non-contact digital image correlation systems exist in the industry of which the ARAMIS system is one; this system was used to measure the crack widths during the tests. The system was developed by GOM Optical Measuring Techniques that is established in Germany. The system consists out of various hardware components and the ARAMIS software version 6.1. The hardware components are a high-performance Personal Computer (PC), a sensor that contains two cameras, sensor controller for power supply to the cameras and to control the image recording and a tripod for secure and steady holding of the sensor during measuring. The system can measure both large and small objects ranging from 1 mm to 2000 mm with the same sensor and can measure deformations ranging from 0.01 % to 100 %. The system

can be used as a 2D or 3D measuring system. During measuring the system takes digital images and stores them so that once the tests are concluded the deformations can be computed by the ARAMIS software. The maximum frame rate depends on the type of sensor and PC used. The PC and sensor available could take images varying from 15 images per second to 1 image per hour. In this research project a frame rate of 1 image per second was used.

After the images were taken they were analysed by the ARAMIS software to calculate the deformations on the test specimen at the stage when the image were taken. The first image taken was referred to as the reference stage and this was taken before the test was started in the un-deformed state. The deformations were determined relative to the reference stage and before the ARAMIS software can analyse the data and calculate the deformations, an area must be defined on the reference stage where the deformations must be calculated. In Figure 3.1, the green area is the area that was defined to be analysed and is referred to as the masked area in the ARAMIS system.

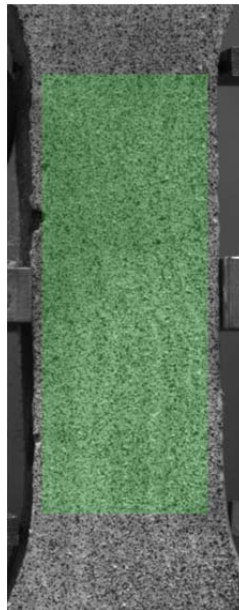


Figure 3.1: Example of a masked area that was defined in the ARAMIS system.

The ARAMIS software package divides the masked area in a grid as shown in Figure 3.2 a). The grid was created from facets that exist of a certain number of pixels. The facet size and step size must be defined before the stages can be analysed by the operator (user). The step size is the number of pixels between two adjacent grid points. Figure 3.2 b) shows a facet size

of 15 x 15 pixels with a 2 pixels overlap. With a 2 pixel overlap the grid points have a step size of 13 pixels. The step size equals the facet size minus the pixels overlap. During the analysis the masked area in the reference stage was given a coordinate system. The coordinates for the corners and centre of each facet was calculated for the reference stage according to the coordinate system. The stochastic pattern on the surface of the object provides identifiable object characteristics. These object characteristics were observed and used to determine the deformation of each facet for each stage in relation to the reference stage. In Section 3.3 it is explained how to apply the stochastic pattern. With the deformed facets the coordinates of the grid points were calculated.

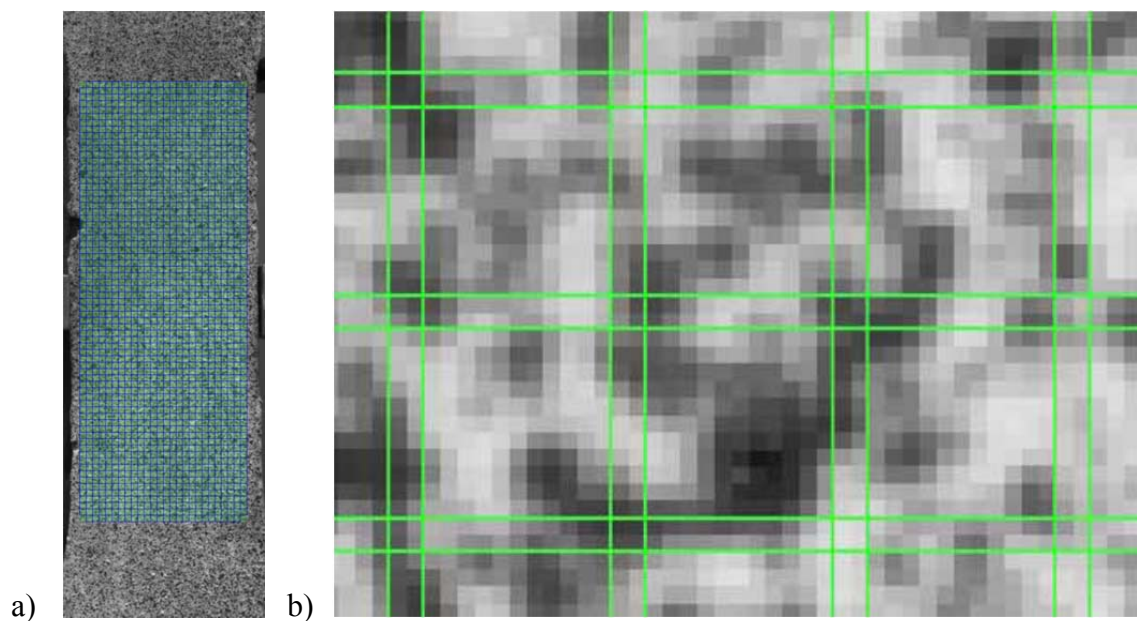


Figure 3.2: a) Example of masked area with strain grid. b) Enlarge view of 15 x 15 facets with a 2 pixels overlap (ARAMIS help file).

During testing the stochastic pattern sometimes failed because of the multiple cracking that forms on the specimen and the ARAMIS system is therefore unable to calculate the coordinates at that point. The ARAMIS software then applies linear interpolation to calculate those coordinates where the stochastic pattern had failed. The implementation of linear interpolation was found to be an inadequate manner to represent the data that was lost during measuring because of the stochastic pattern that failed. The reason why the linear interpolation was found to be inadequate was that a single crack that formed on a specimen may be divided into more than one crack by the ARAMIS data. Thus an alternative solution

was found to solve this problem and will be explained in Section 3.8. The method of how the cracks were determined and the crack widths were calculated is explained in Section 3.6

ARAMIS provides a number of methods to export the un-deformed coordinates along with the deformed coordinates for each stage. The method used for this research project was the section line method. This method allows the user to export the coordinates on a number of lines which were defined by the user. The line was divided in a number of points and the coordinates of these points were calculated from the grid points. The un-deformed and deformed coordinates of these sections lines for each stage were then exported to a file which was used to calculate the crack widths.

After the ARAMIS software package had analysed the masked area, the software shows a 2D or 3D contour view of the deformations of the analysed area. Figure 3.3 a) shows the cracks formed on the gauge length of the specimen at a certain overall deformation and Figure 3.3 b) shows the principal strains calculated by the ARAMIS software at the same deformation as Figure 3.3 a).

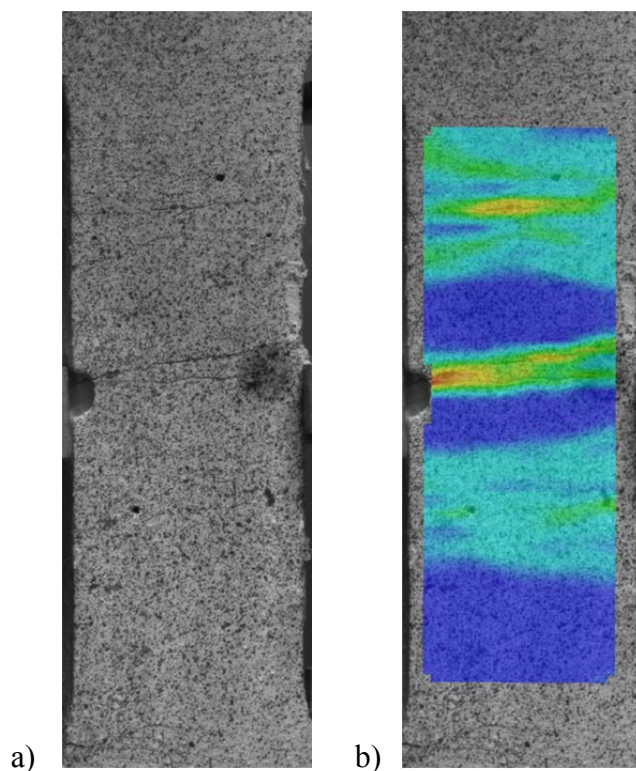


Figure 3.3: a) A picture of the cracks that formed on the specimen, b) The principal strains contours calculated by the ARAMIS system.

3.2 Research Program

An investigation of the ARAMIS system is included within the scope of this research program. Uni-axial tensile tests were performed on tensile specimens to obtain cracking data and all these tests were performed at a tensile loading rate of 0.02 mm/s. This investigation was implemented so that the minimum number of section lines required for calculating the crack widths could be determined. As explained in the previous section the facet size and step size are user inputs, thus these two parameters are unknown input parameters and need to be resolved in order to get accurate cracking data. Four different facet sizes and step sizes were investigated and these are shown in Table 3.2 in Section 3.5. An alternative solution for interpolation as discussed in the previous section also needs to be found. Out of this investigation a crack definition was defined that was used to calculate the crack widths on the tensile specimens and was used to quantify the cracking behaviour of SHCC.

3.3 Specimen Preparation

A mix was designed so that an average strain capacity of more than 4 % would be reached at a tensile loading rate of 0.02 mm/s. In Appendix A the different mixes that were tested during the mix design are given. Mix 3 gave the best strain hardening during the comparison of the different mixes and was thus chosen as the correct mix for the trials. During testing the specimen failed after 2 to 5 minutes. All the constituents that were used during the trials were supplied by local suppliers except the fibres, which were supplied by Kuraray in Japan. The following ratios between the constituents gave the best results and were selected for the trials: water/binder ratio of 36 %, aggregate/binder ratio of 50 %, viscous modification agent/cement ratio of 0.263 % and super plasticiser/cement ratio of 0.395 %. The binder is of CEM I 42.5N supplied by PPC South Africa and fly ash marked as Dura Pozz by Ash Resources. For aggregate Silica Consol sand number 2 was used, which is a fine sand with particle size smaller than 300 μm . Figure 3.4 shows the grading of the aggregate. Table 3.1 gives a summary of the mixing proportions.

The proportions given in Table 3.1 were adjusted to provide a 10 litre mix. Three 10 litre (volume) batches were mixed and each 10 litre mix was used to cast twelve dogbones as well as a flow table test. The mix constituents were weighed to the nearest gram except for the

admixtures, namely the Super Plasticiser and Viscous Modification Agent, which were weighed to the nearest milligram. A pan mixer was used to mix the constituents. The pan was cleaned with a wet cloth before the dry constituents were added to ensure that the pan was saturated with water to ensure that no water will be lost during the mixing process.

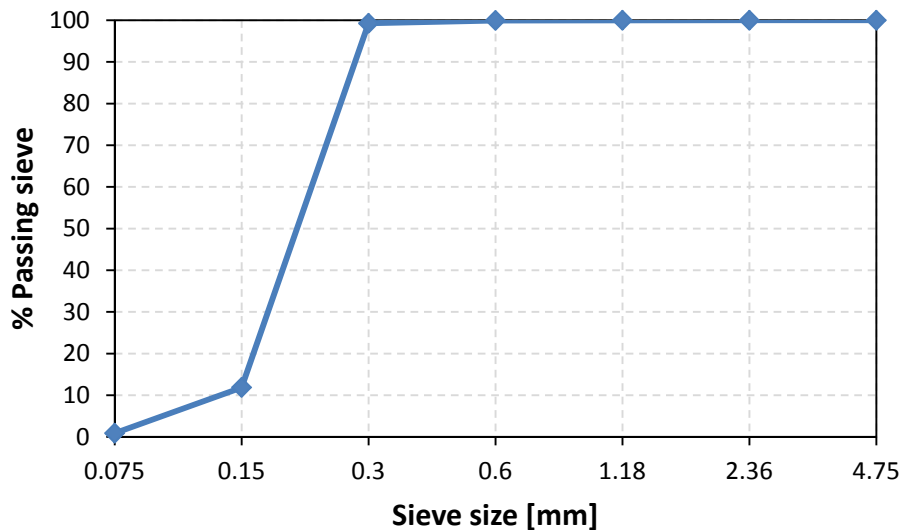


Figure 3.4: Aggregate grading: Silica Console sand no. 2.

Table 3.1: SHCC constituents and mix proportions.

Constituents	Ratio/Type	Mix proportions (kg/m ³)
Water/binder ratio	0.36	-
Aggregate/binder ratio	0.5	-
Cement	CEM I 42.5N	380
Fly Ash	Ratio of 1 : 0.56 to mass of cement	679
Sand	Silica sand; Particle size < 300 μm ; Silica Console sand no. 2	530
Water	-	380
Fibres	PVA-RECS 15; Length = 12 mm; Diameter = 40 μm ; 2% by volume	26
Viscous Modification Agent	Aqua Beton; from Chryso 0.263 % of cement	1
Super Plasticiser	Premia 310; from Chryso 0.395 % of cement	1.5

The mixing process was as follows: Half of the sand was added into the mixing pan and then the cement, fly ash and viscous modification agent was added on top of the first half of the sand. The balance of the sand was then added on top. This ensured that the cement and fly ash was trapped between the two sand layers in order to eliminate the loss of the fine particles of cement and fly ash during the mixing process. Once this was completed the dry constituents were mixed together for a period of 1 minute. After 1 minute of mixing had been completed water was slowly added to the mixture and all the constituents were mixed for a second period of 1 minute. On completion of the second mixing period of 1 minute the super plasticiser was added and a third period of 1 minute mixing was followed. When the third interval of 1 minute of mixing was completed, the mixer was stopped and an inspection was performed to check that all the constituents were uniformly mixed throughout. If satisfied with the results of the inspection the mix was continued and the PVA fibres were added over a period of 1 minute to ensure that they were evenly distributed throughout the whole mix. Once the fibres had been added the mixing was continued for further a period of 5 minutes whilst the moulds were being prepared for casting. Figure 3.5 shows the mixing procedure and mixing times schematically.

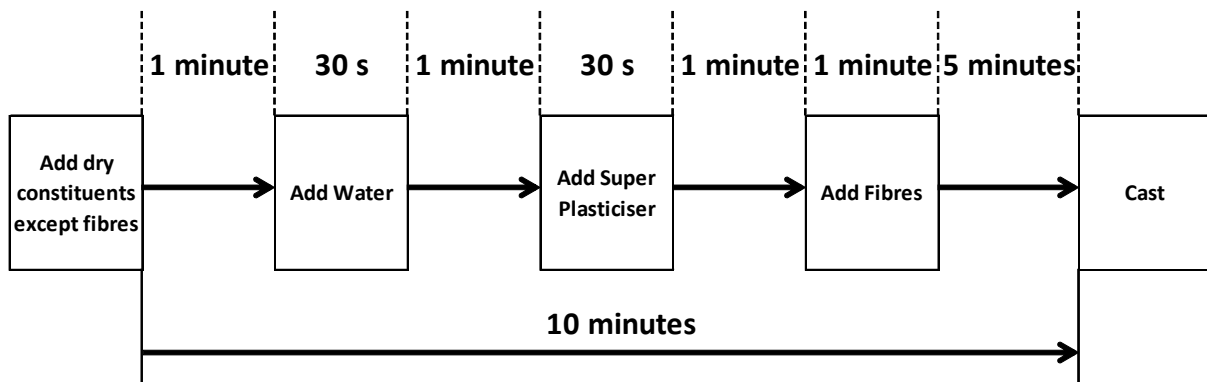


Figure 3.5: Mixing procedure with the times.

Upon completion of mixing the various constituents a rheology test was conducted on the mix with a flow table, to ensure that the workability of the final mix was correct. The rheology test was conducted in accordance with the procedure as set out in British Standard EN 1015-3:1999. Included in the apparatus used for this test is a circular steel cone with a top and bottom diameter of 70 mm and 100 mm respectively and a wall thickness of 5 mm; refer to Figure 3.6 for a picture of the flow table apparatus. The cone is placed on the circular table

of the apparatus that is connected to a rotating shaft. The cone is then filled to one third of its volume and tamped ten times in a circular motion with a tamper. The tamper consists out of a rigid, non-absorptive circular rod and a tampering face of 40 mm in diameter. The cone was then filled to the top and tamped another 10 times in the same manner. Once the tamping was complete the cone was removed leaving the test sample on the table and the shaft was rotated 15 times with a speed of one cycle per second. Whilst the table is being rotated it lifts to a specific height and is then suddenly dropped, with the result that the cement-based composite spreads over the table. On completion of the 15 cycles the flowed mix was measured at right angles of each other and the average of the two measurements was calculated. Previous laboratory tests showed that the average diameter of the flowed mix should be between 150 mm and 160 mm to obtain the correct workability of the composite. If this requirement was achieved then the mix was approved, if not the mix was discarded.



Figure 3.6: The flow table apparatus used for testing the rheology.

Upon the successful completion of the flow test the mix was cast in the dogbone moulds. The moulds were lined with mould release oil to assist with the removal of the specimens from the moulds. Figure 3.7 shows a mould that was used to cast the test specimens. The moulds are made of steel and have removable lids. At both ends of the mould there are two 16 mm diameter pins that form holes through the specimen that helped with the clamping process during testing. Figure 3.8 shows the dimensions of the specimen.

The mix was then cast into the dogbone moulds that were then vibrated for at least 1 minute to remove air pockets. The moulds, without the lids, were then moved to the climatic room where they were then left for an hour and a half to allow most of the entrapped air to dissipate. Upon completion of the hour and a half dissipation time the surfaces of the specimens were levelled with a trowel, this also removed any air bubbles trapped under the specimen surfaces, and the lids were put on. The moulds were then kept in the climatic room for three days at a temperature of $24^{\circ}\text{C} \pm 2^{\circ}\text{C}$ and a relative humidity of $65\% \pm 10\%$. Finally after three days in the climatic room, the specimens were stripped out of the moulds and water cured for a further 11 days in curing baths.



Figure 3.7: A steel mould with lid used for casting the dogbone specimens.

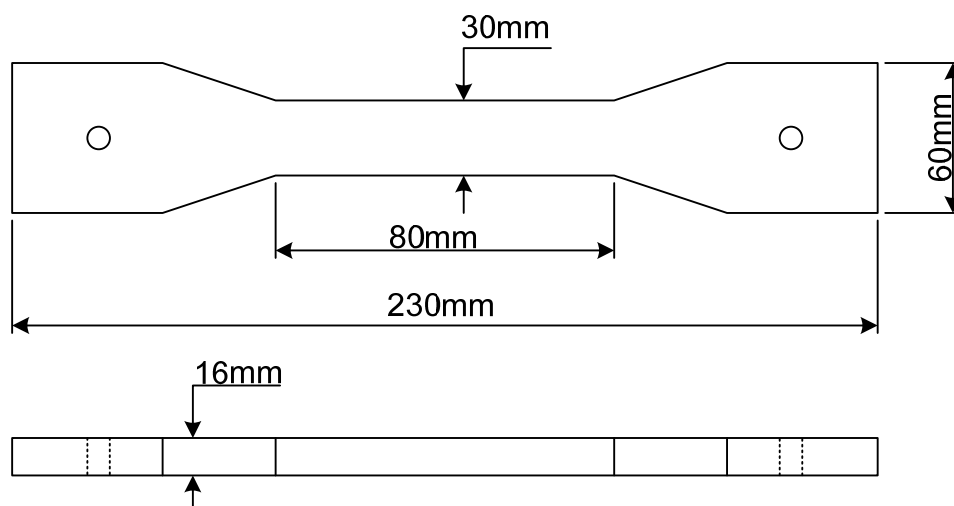


Figure 3.8: Dimensions of the test specimens.

When the 11 days of water curing process was completed, the specimens were subjected to the planned tests. Prior to this testing, the specimens surfaces were dried using compressed air after being removed from the curing baths. When dried the gauge length surfaces of the specimens were painted with a 1 mm layer of ground limestone mixed with water. This thin layer of limestone was dried with compressed air to quicken the drying process where after a stochastic pattern was sprayed on the dried limestone surface with black aerosol paint. This stochastic pattern is required by the non-contact surface deformation measuring system, ARAMIS, which was used to measure the crack widths as explained in Section 3.1. Figure 3.9 shows a specimen painted with limestone and a stochastic pattern and Figure 3.10 shows an enlarged view of a stochastic pattern.



Figure 3.9: Specimen with painted layer of limestone.



Figure 3.10: Enlarged view of stochastic speckle pattern on specimen.

3.4 Test Setup

Uni-axial quasi-static tensile tests were conducted in a Zwick Z250 Universal Materials Testing Machine. The tests were controlled by the displacement rate of the cross head of the Zwick. Two clamps specifically designed to test these dogbone specimens were used to clamp the specimens in the machine, see Figure 3.11. The top clamp has a hinged support with two rotational degrees of freedom and remains stationary during testing. The bottom clamp is a rotationally fixed support and can only displace vertical during testing. The clamps were designed in this manner so that only a tension force would be applied to the dogbone specimen and no additional moments.



Figure 3.11: The clamps used for the uni-axial tensile tests in the Zwick.

The Zwick Z250 universal Materials Testing Machine has its own load cell with a capacity of 250 kN, but a separate 5 kN HBM load cell was used to measure the tensile force to ensure more accurate loading readings. The linear displacement over the 80 mm gauge length was measured with a HBM DD1 Clamp-on Strain Transducer, see Figure 3.12. The load cell and DD1 was connected to a spider 8 high frequency multi-channel electronic PC unit to synchronise the load from the HBM 5 kN load cell and the linear displacement from the DD1.

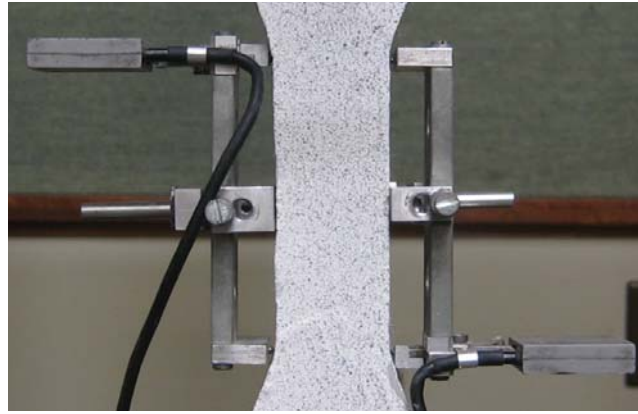


Figure 3.12: The HBM DD1 Clamp-on Strain Transducer.

The crack widths on the 80 mm gauge length were measured with the ARAMIS system, see Figure 3.13. The ARAMIS system is connected to a different computer and to link the load with the strain calculated from the ARAMIS system, the synchronised times from the two computers were used.



Figure 3.13: The ARAMIS system.

3.5 Experimental Test Program

Four specimens were tested at a tensile loading rate of 0.02 mm/s. Each specimen was loaded until a strain of about 2.65 % and then the specimen was unloaded so that a residual strain of about 1.38 % was obtained. The ARAMIS system was used to measure the cracks formed on the gauge length of the specimen. The reason for the specimens being loaded and unloaded in

this manner was to enable the number of cracks on the specimen in the unloaded state to be counted through a microscope and then compare it to the number of cracks calculated from the ARAMIS data. The ARAMIS data for each specimen were analysed in four different facet and step sizes to determine which sizes must be used to get the most accurate cracking data, refer to Section 3.1 for the definition of facet and step sizes. Table 3.2 shows the facet and step sizes that were used to analyse the ARAMIS data for each test.

Table 3.2: The four different facet and step sizes.

Facet Size [Pixels]	Step Size [Pixels]
15	13
26	13
30	26
45	39

3.6 Evaluation of Crack Width

The ARAMIS data was used to calculate crack widths from an observed area on the gauge length of the specimen of approximately $70 \text{ mm} \pm 5 \text{ mm}$ in length and $20 \text{ mm} \pm 5 \text{ mm}$ in width; see Figure 3.14. This observed area was divided into a number of section lines and on these section lines coordinate points were given in both the deformed state and un-deformed state as explained in Section 3.1. The method used to determine the number of section lines that were used is explained later on in this section. These coordinate points were a predetermined distance away from each other. A crack width could only be calculated when the crack crossed one or more section lines and the crack widths were calculated between two adjacent points. The following method was used to calculate the cracks widths; firstly the distance between two adjacent points in the deformed state was calculated and secondly the distance between the same two points was calculated in the un-deformed state. The deformation between the two points was the difference between the distances in the deformed and un-deformed state. Due to the micro cracking formed in the linear elastic phase of the stress-strain response of the specimens during uni-axial tensile loading, the deformation between two points was limited with a lower bound value. The lower bound value was chosen as $20 \text{ }\mu\text{m}$. The linear elastic phase is the linear part of the stress-average strain

response of the gauge length of the dogbone specimen. In Section 3.8 it is explained how the lower bound value was determined. A crack width was calculated as the difference in distance between two adjacent points in the deformed and un-deformed state given that the local deformation between the two points was more than $20\ \mu\text{m}$.

To determine the number of section lines needed to get accurate cracking data, the number of cracks per metre was plotted against the number of section lines. Figure 3.15 shows two graphs with the number of cracks per metre against the number of section lines used for three test specimens at 0.3 % and 1.5 % strain respectively. Because the facet size and step size values to obtain the best cracking data had not yet been established, the default values were used during the analyses, namely facet size of 15 pixels and step size of 13 pixels.

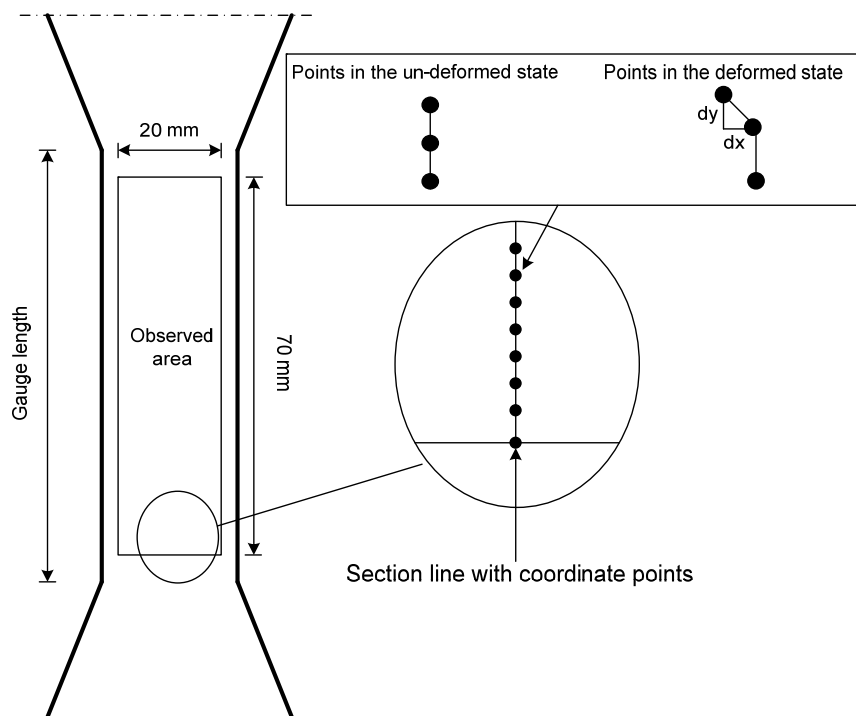


Figure 3.14: Observed area on gauge length of a specimen with an enlarged view of the coordinates on a section line to demonstrate the un-deformed and deformed state of the coordinates.

The red line in Figure 3.15 a) and b) is the average number of cracks per metre calculated from the results of the three test specimens at different number of section lines at a specific strain. From Figure 3.15 a) and b) it can be seen that the number of cracks per metre starts to stabilise at five section lines and it can therefore be assumed that the cracking data calculated when five section lines are used, will give more or less the same results as what nineteen section lines would give. The workload connected to five section lines was significantly less

than that for nineteen section lines and from this point on it was decided to limit the number of section lines required to calculate the crack widths to five.

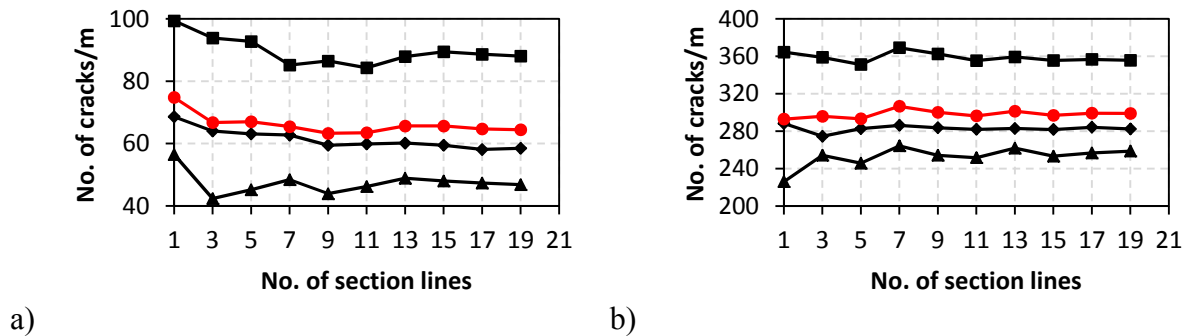


Figure 3.15: a) The number of cracks plotted against the number of section lines at 0.3 % strain. b) The number of cracks plotted against the number of section lines at 1.5 % strain.

3.7 Results

In Figure 3.16 the stress-strain responses for the four test specimens are given. The stress was calculated by dividing the force that was recorded from the load cell, with the cross sectional area of the gauge length. The strain was calculated over the gauge length of 80 mm and was recorded by the DD1 Clamp-on Strain Transducer. The specimens in Figure 3.16 were not loaded until failure, but were only loaded until a strain capacity of about 2.65 % was reached and then unloaded so that a residual strain of about 1.38 % was obtained.

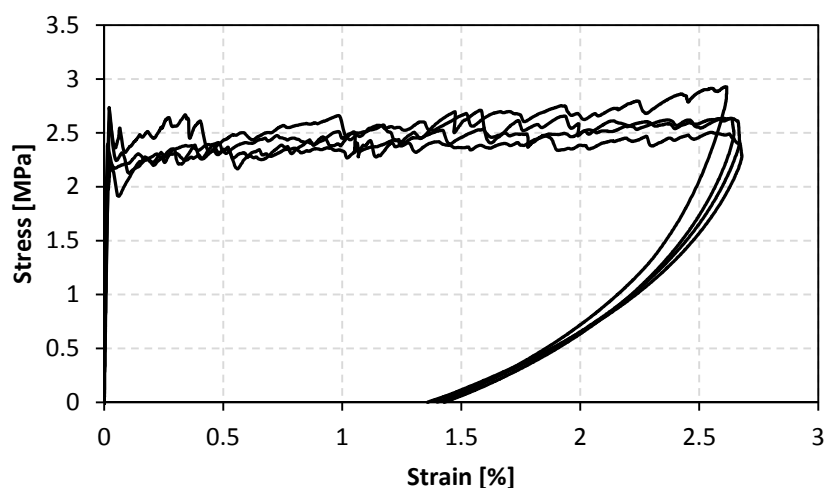


Figure 3.16: Stress-strain response of the four test specimens with a residual strain of about 1.38 %.

The ARAMIS system was used to measure the deformation on the gauge length area when the tests were conducted on the four specimens. In addition a crack definition was required in order to calculate the crack widths and the number of cracks from the ARAMIS data. The number of section lines used over the observed area was five; refer to Section 3.6 on how the number of section lines used was determined. The lower bound value used to specify when a crack has formed between two adjacent points also needed to be defined, refer to Section 3.6 for the explanation of the lower bound value. To determine this lower bound value there was looked at the maximum deformation during the linear elastic phase of the stress-strain response. This was done for the four different facet and step sizes defined in Section 3.5. Table 3.3 gives a summary of the maximum deformation calculated out of the ARAMIS data in the linear elastic phase for the four different facet and step sizes.

Table 3.3: Maximum deformation during linear elastic phase.

Facet and Step Size [Pixels]	Test no.	Maximum deformation during linear elastic phase [μm]				Average	Used
		1	2	3	4	[μm]	[μm]
Facet 15 step 13		7.748	14.600	17.830	29.360	17.384	20
Facet 26 step 13		6.720	6.377	10.330	18.490	10.480	20
Facet 30 step 26		6.124	4.980	15.300	26.530	13.230	15
Facet 45 step 39		8.860	3.071	14.410	24.140	12.620	15

In Table 3.3 the average maximum deformation during the linear elastic phase are given as well as the lower bound values that were used for each facet and step size during the analyses of the ARAMIS data. In Section 3.8 it is explained how the lower bound value that was used was determined.

Once the lower bound values were defined for each facet size and step size the number of cracks were calculated from the ARAMIS data for each specimen for the different facet and step sizes at a residual strain of 1.38 %. These values were then compared against the number of cracks that were counted on the specimen by a microscope at the same residual strain. The number of cracks calculated on the specimens with a given facet and step size that were the closest to the number of cracks that were microscopically counted on the specimens was used as the facet size and step size to calculate the crack widths. In order to reduce the workload the number of cracks were only calculated on the middle section line and subsequently the cracks that were counted on the specimen by microscope were counted at the same position

where the middle section line were situated. Table 3.4 gives a summary of the number of cracks calculated from ARAMIS data for each test for the different facet and step sizes as well as the number of cracks that were counted on each specimen with a microscope at a residual strain of 1.38 %.

Table 3.4: Summary of number of cracks calculated out of the ARAMIS data on the middle section line and the number of cracks counted on the specimen with a microscope at a residual strain of 1.38 %.

ARAMIS SYSTEM		No. of cracks on middle Section line calculated by Aramis			
Test no.		1	2	3	4
Facet 15 step 13		16	17	19	23
Facet 26 step 13		16	13	20	28
Facet 30 step 26		23	21	22	25
Facet 45 step 39		15	14	17	16
Microscope		no. of cracks counted on middle of specimen with a microscope			
Test no.		1	2	3	4
		15	11	22	28

Figure 3.17 shows the crack distribution for Test 2, which was calculated by using the ARAMIS data with a facet size of 26 pixels and step size of 13 pixels, included is a photo of the cracks that formed on the specimen counted by microscope. The cracks are drawn in by hand because they are too small to see with the naked eye.

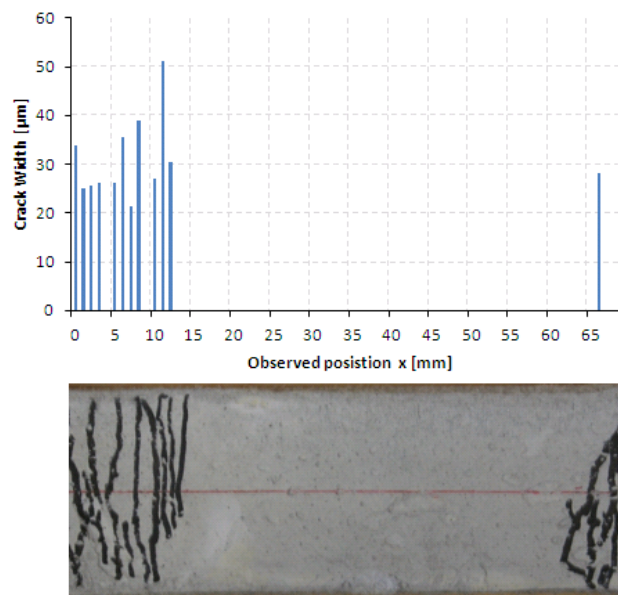


Figure 3.17: The crack distribution calculated from the ARAMIS data (top) and a photo of the cracks that were counted on the specimen through a microscope (bottom).

Once the facet size and step size were selected an investigation was conducted into the accuracy of the ARAMIS system in measuring the width of cracks. This was done by comparing the crack width calculated from the ARAMIS data against a measurement in AutoCAD. The photo, on which the measurement was done in AutoCAD, was scaled to the correct size. Figure 3.18 a) shows the crack that was measured in AutoCAD and Figure 3.18 b) shows an enlarge view of the crack. Table 3.5 gives a summary of the crack width calculated from the ARAMIS data and the crack width measured in AutoCAD.

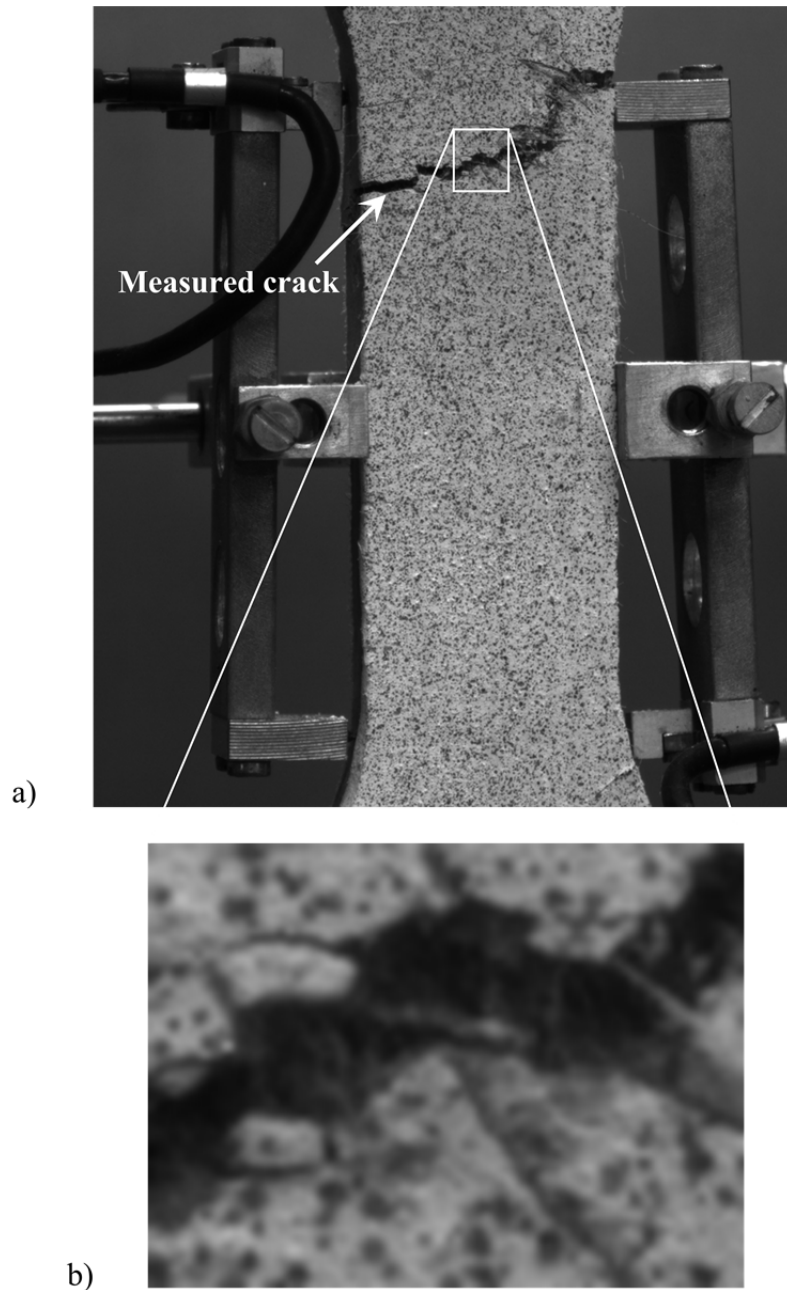


Figure 3.18: a) The test specimen with the developed crack that was measured. b) An enlarged view of the measured crack.

Table 3.5: Summary of crack widths determined with ARAMIS system and AutoCAD software.

	Stage Number	Crack Width [μm]
ARAMIS System	266	1531.511
AutoCAD software program	266	1253

3.8 Discussion

From Table 3.4 it can be seen that the facet size of 26 pixels and step of 13 pixels gave the best results in terms of the number of cracks calculated out of the ARAMIS data and were subsequently chosen as the facet size and step size. Figure 3.17 shows the crack distribution for facet size of 26 pixels and step size of 13 pixels with a photo showing where the cracks formed on the gauge length of the specimen. It can be observed from Figure 3.17 that the ARAMIS system calculates the number of cracks and the position of the cracks fairly accurately for a facet size of 26 pixels and step size of 13 pixels. The lower bound was chosen as 20 μm for facet size of 26 pixels and step size of 13 pixels, see Table 3.3. Even though the average maximum crack width in Table 3.3 during the linear elastic phase was only 10.479 μm , the lower bound was still chosen as 20 μm because it gave more accurate results in terms of the number of cracks formed.

In Table 3.5 the crack width calculated by the ARAMIS system was compared against a measurement done on the same crack using an AutoCAD software program. The AutoCAD software program measurement was lower than the crack width calculated from the ARAMIS data. The reason for this may be due to an inaccurate measurement technique used to measure the crack width in the AutoCAD software program. When the photo is enlarged in the AutoCAD software program the quality of the photo deteriorates with the result that there was discontinuity of the crack edges and it was therefore difficult to establish where the crack edges were, see Figure 3.18 b). Another explanation for the difference in the measurements may be that the crack width calculated from the ARAMIS data was between two points and may include micro crack widths that were not included in the measurement done in the AutoCAD software program.

The problem with interpolation, as mentioned in Section 3.1, was resolved when a facet size of 26 pixels and larger was used. This means that a larger area was observed to identify a point in the deformed state with the result that the point will be identified more accurately. It was found that when using a facet size of 26 pixels and larger no interpolation was required

after the data was analysed. Figure 3.19 a) shows an observed area analysed with a facet size of 15 pixels and step size of 13 pixels and Figure 3.19 b) shows the same observed area as in Figure 3.19 a) analysed with a facet size of 26 pixels and step size of 13 pixels. In Figure 3.19 a) some of the coordinates were lost due to failure of the stochastic sprinkle pattern and because the facet size was so small, it could not identify the points. In Figure 19 b) no interpolation was needed because the facet size is large enough to identify the points.

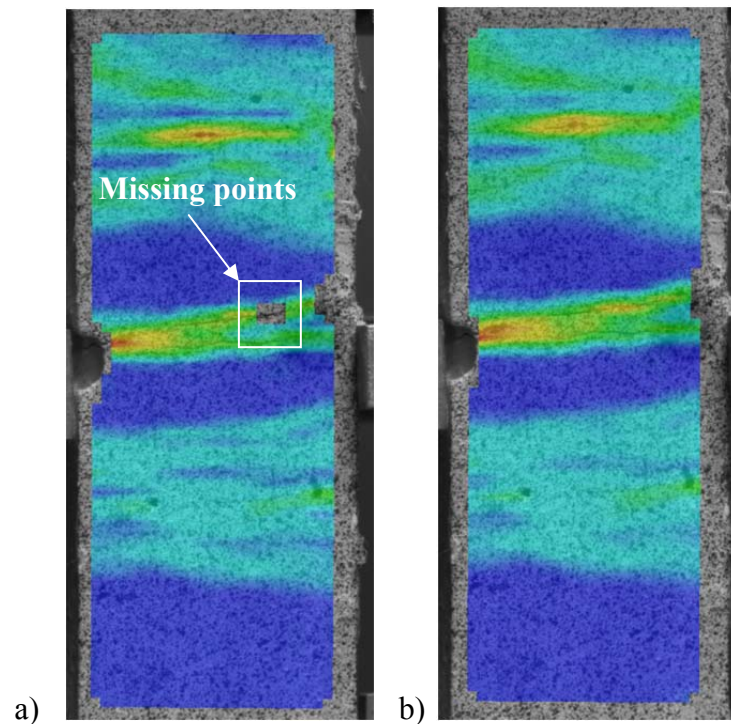


Figure 3.19: a) Shows a observed area analysed with a facet size 15 and step size 13. b) Shows the same observed area analyse with a facet size of 26 and step size 13.

From the results given above it can be concluded that to get accurate cracking data a minimum of five section lines, a facet size of 26 pixels and step size of 13 pixels must be used during the analysis of the data. With a step size of 13 pixels the distance between two adjacent coordinate points is 1 mm. Also a crack is defined as a local deformation between two adjacent points of more than 20 μm and the crack must cross one or more section lines.

CHAPTER 4

QUANTIFYING THE CRACKING BEHAVIOUR OF SHCC

4.1 Research Program

The scope of this research program includes the quantification of the cracking behaviour of SHCC. In this research program the cracking behaviour of SHCC is described by a crack width distribution model which is described by some descriptive statistical properties and a mathematical model that quantitatively describes the crack pattern of SHCC. The aim of this research topic was to find a statistical distribution model that describes the crack widths of SHCC and to find a mathematical method to quantitatively describe the crack pattern of SHCC. The same test setup and dogbone specimens that were used as in Chapter 3 were also applied here to collect the cracking data. The crack definition defined in Chapter 3 was also applied here to calculate the crack widths from the data compiled by the ARAMIS system.

4.1.1 Stochastic Description of the Crack Width Distribution

As briefly explained in Chapter 1, a crack width distribution model is needed to quantify the durability of SHCC. Boshoff and Adendorff (2010) stated that, although the average crack width is below a certain threshold where no penetration of substances can take place, it is probable that some of the cracks are larger than the average crack width where substances can penetrate the material. The approach to use the maximum crack width is also not applicable, because when observing a larger area of cracks the probability of finding a larger crack width increases. Different statistical distribution models were considered in order to

find a statistical distribution model that suitably describes the crack widths of SHCC. The model that best described the crack widths was chosen to represent the distribution of the crack widths of SHCC, see Section 2.2.2 for the different statistical distribution models that were used.

4.1.2 Mathematical Description of the Crack Pattern

As mentioned in Chapter 1, recent studies had shown that the crack pattern of SHCC has an effect on the durability of SHCC (Kato et al., 2005). In Section 4.3.3 a method is presented on how to quantify the crack pattern of SHCC. Figure 4.1 shows three different crack patterns at the same tensile strain.

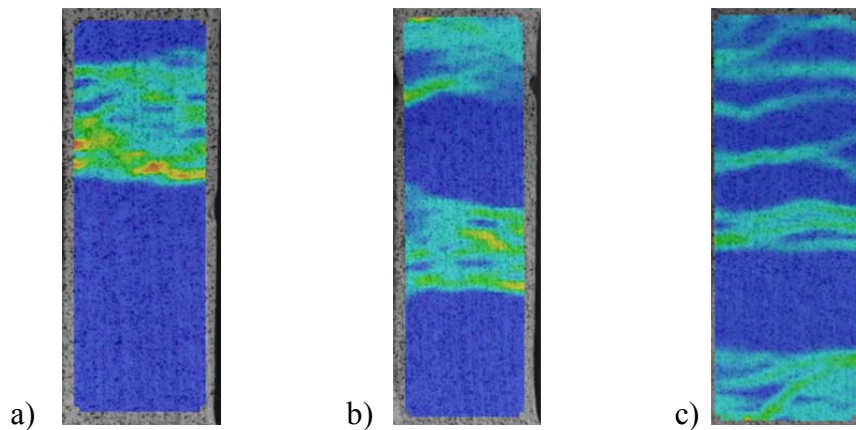


Figure 4.1: Three different crack patterns at the same tensile strain.

In Figure 4.1 a) all the cracks that formed are located at one area on the gauge length of the specimen and in Figure 4.1 c) the cracks are more evenly distributed over the gauge length of the specimen. The crack pattern in Figure 4.1 a) may have a larger effect on the durability of material than the crack patterns in Figure 4.1 b) and c), because the cracks in Figure 4.1 b) and c) are further apart from each other. The method presented in Section 4.3.3 quantifies the crack pattern in terms of crack spacing.

4.2 Experimental Test Program

The test setup used was the same as in Section 3.4. All tensile tests were done at a tensile loading rate of 0.02 mm/s. The specimens were loaded until failure.

4.2.1 Stochastic Description of the Crack Width Distribution

A total of fourteen specimens were tested that was prepared from three batches, but for the purposes of this research topic the results are reported as a single set. The deformations of the gauge length of the specimens were measured with the ARAMIS system.

4.2.2 Mathematical Description of the Crack Pattern

The same cracking data that was collected to find a statistical distribution model that describes the crack widths of SHCC were used to quantitatively describe the crack pattern of SHCC. It should be noted that only one side of the surface on the gauge length of the specimen was investigated during testing, with the assumption that the crack pattern will be similar on both sides of the surface on the gauge length of the specimen.

4.3 Results

In this section some descriptive statistical parameters, namely number of cracks per meter, average crack width, standard deviation and skewness are quantified at different strains. The descriptive statistical parameters were then used to find a statistical distribution that described the crack widths. A method to quantify the crack pattern is also presented.

4.3.1 Experimental results

In Figure 4.2 the stress-strain response of all fourteen specimens are given. The average first cracking stress was 2.42 MPa (Coefficient of variation of 12.58 %). The average ultimate tensile stress was 2.75 MPa (Coefficient of variation of 20.46 %) and the average ultimate tensile strain was 4.04 % (Coefficient of variation of 12.19 %).

The statistical parameters introduced in Section 2.2.1 were calculated for each specimen at the following tensile strains, 0.3 %, 0.6%, 1%, 1.5%, 2% and 2.5%. The averages with the minimum and maximum values and the coefficient of variation expressed in percentage for the following properties namely the number of cracks per metre, average crack width,

standard deviation of the crack widths and skewness of the crack widths are displayed in Figures 4.3 to 4.6 against the tensile strains mentioned above.

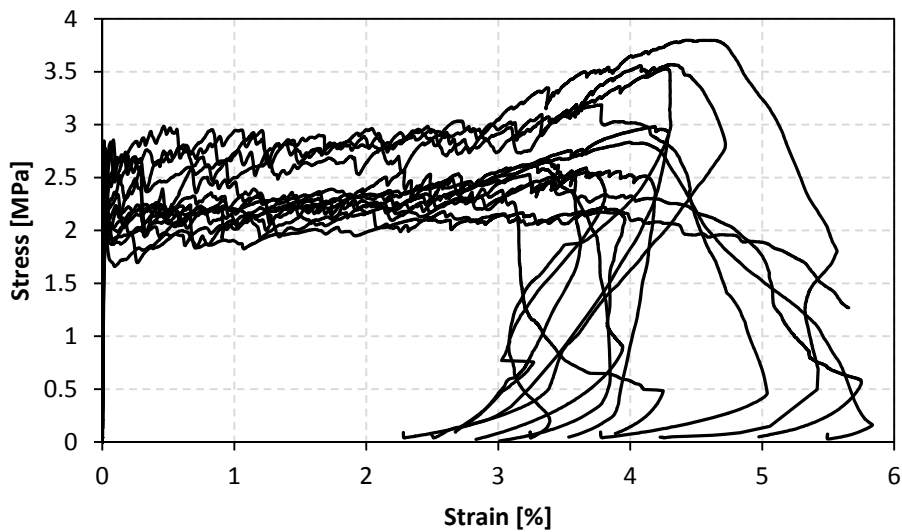


Figure 4.2: Stress-strain response of the quasi-static tensile tests.

The averages of the properties are fitted with a regression line and the coefficient of variation and the equation of the regression line are also displayed in the graphs. The data of the properties for each specimen at each tensile strain can be found in Appendix B.

Figure 4.3 shows the average number of cracks per metre also referred to as the crack intensity. Five section lines were used to calculate the average number of cracks per metre over the observed area. The observed area for each specimen differed slightly as a result of the manual masking that was done during the analysis of the data by the ARAMIS system. It can be seen in Figure 4.3 that the average number of cracks per metre increase linearly as the strain increase and is best described by a linear regression line. A stage will be reached where the average number of cracks should stabilise due to the phenomena of crack saturation even should there be a further increase in the tensile strain. This is not shown in Figure 4.3 as crack saturation is reached at a higher tensile strain than 2.5 %.

The average of the average crack width is shown in Figure 4.4 and it is evident that the average of the average crack width stays fairly constant as the strain increases. A 22.2 % increase in the average of the average crack width was found as the tensile strain increased from 0.3 % to 2.5 %.

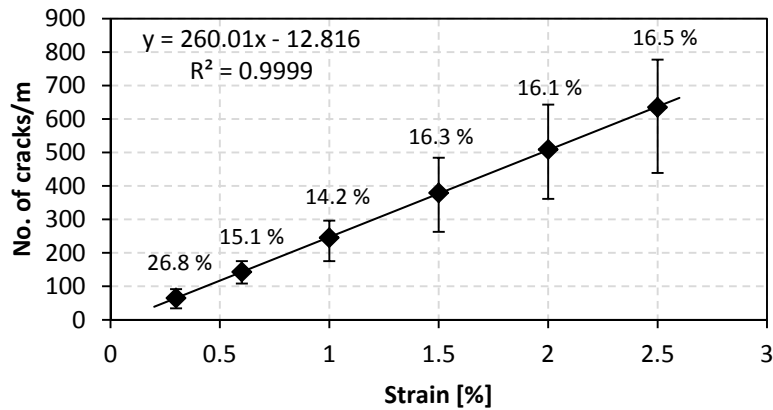


Figure 4.3: The average, maximum, minimum and coefficient of variation of the number of cracks per metre at different tensile strains.

This finding corresponds with the average number of cracks per metre as in order for the average number of cracks per metre to increase as the tensile strain increases, the average of the average crack width must stay constant. In the previous paragraph it was mentioned that the average number of cracks per metre should stabilise at a later tensile strain, this is not depicted on the graph. At this point the average of the average crack width should increase as the tensile strain increases. The average of the average crack width at the different tensile strains is best described by a logarithmic regression line as presented in Figure 4.4.

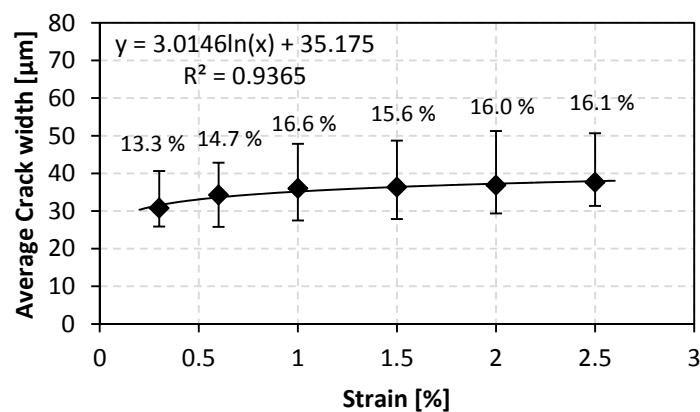


Figure 4.4: The average, maximum, minimum and coefficient of variation of the average crack width at different tensile strains.

The average standard deviation of the crack widths is shown in Figure 4.5. The standard deviation is a measurement of the dispersion of the crack widths around the average crack width. Figure 4.5 shows that the average standard deviation increases as the tensile strain increases. An 86.3 % increase in the average standard deviation was found as the tensile

strain increased from 0.3 % to 2.5 %. This increase of the average standard deviation can be explained by the phenomenon that at lower tensile strains the number of small cracks formed is much greater than the number of larger cracks that is formed. As the tensile strain increases new small cracks still form, but there is a significant increase in the number of larger cracks formed. This explains the reason why the average standard deviation increases as the tensile strain increases. The logarithmic regression line shown in Figure 4.5 best describes the average standard deviation at the different tensile strains.

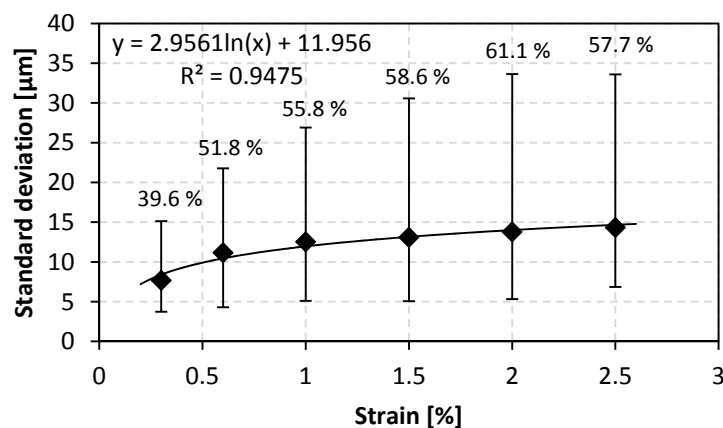


Figure 4.5: The average, maximum, minimum and coefficient of variation of the standard deviation at different tensile strains.

The average skewness of the crack widths are plotted in Figure 4.6. The skewness is a measurement of the asymmetry of a statistical distribution. A 121.7 % increase in the average skewness was found as the tensile strain increased from 0.3 % to 2.5 %. The same phenomenon that caused the average standard deviation to increase with the increase in the tensile strain caused the average skewness to increase. The explanation is that at lower tensile strains more small cracks in comparison to large cracks form. As the tensile strain increases small cracks still continue forming, but there is a significant increase in the number of large cracks formed. The histograms of the crack widths of a test at 1 % and 2.5 % tensile strain are shown in Figure 4.7 to demonstrate this phenomenon. It can be seen from Figure 4.7 that the skewness increased significantly from 1 % to 2.5 % tensile strain which explains why the average skewness increases with the increase in tensile strain as indicated in Figure 4.6. The average skewness is positive as the tensile strain increases, and indicates that the statistical distribution that will describe the crack widths will be skewed to the right. The average

skewness at the different tensile strains is best described by a logarithmic regression line, refer to Figure 4.6.

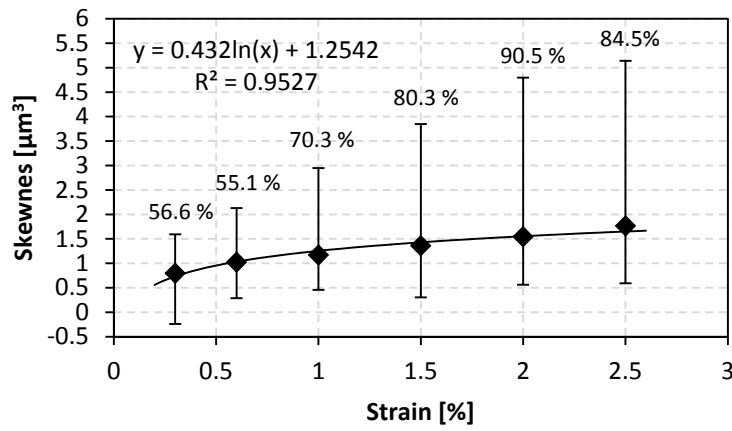


Figure 4.6: The average, maximum, minimum and coefficient of variation of the standard deviation at different tensile strains.

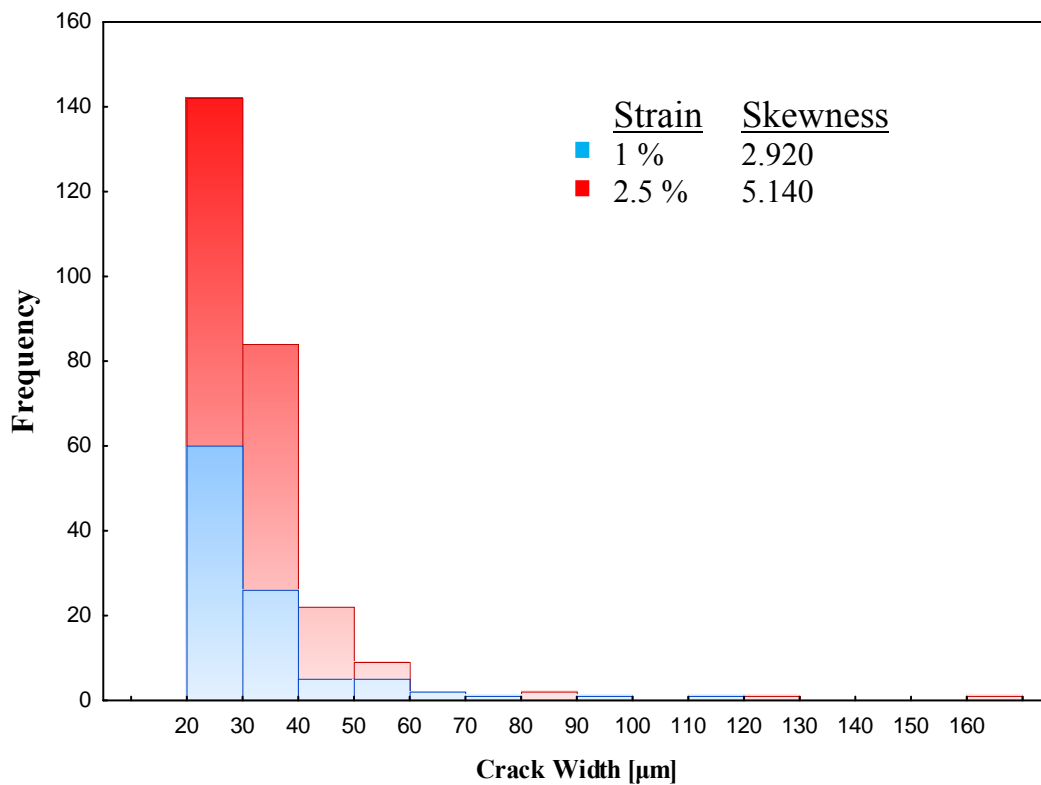


Figure 4.7: Histograms of a test at 1 % and 2.5 % tensile strain.

4.3.2 Stochastic Description of the Crack Width Distribution

The methods used to determine which statistical distribution will best represent the distribution of the crack widths were the Quantile-Quantile plot and Coefficient of Determination. The statistical distributions that were used and their parameters can be reviewed in Section 2.2.2. From the Quantile-Quantile plot data the Coefficient of Determination for each specimen at the tensile strain 0.3 %, 0.6 %, 1 %, 1.5 %, 2 % and 2.5 % are calculated. The calculation of the Coefficient of Determination is explained in Section 2.2.3.2. The average of all the Coefficient of Determinations for each test for the different statistical distributions at the different tensile strains is given in Table 4.1. In Figure 4.8 the average Coefficient of Determination for the different statistical distributions are plotted against the tensile strain.

Table 4.1: The average Coefficient of Determination for the different statistical distributions used to describe the distribution of the crack widths at the different tensile strains.

Distribution	Lower bound [μm]	Coefficient of determination R ²						
		Strain	0.30%	0.60%	1%	1.50%	2%	2.50%
Normal	-		0.913	0.897	0.891	0.875	0.859	0.843
Gamma	0		0.947	0.952	0.957	0.951	0.942	0.932
Gamma	20		0.959	0.965	0.975	0.975	0.971	0.966
Log-normal	0		0.951	0.955	0.959	0.951	0.940	0.932
Log-normal	20		0.826	0.803	0.799	0.795	0.811	0.795
Best			Gamma	Gamma	Gamma	Gamma	Gamma	Gamma

It was established that the Gamma distribution with a lower boundary, $x_0 = 20 \mu\text{m}$ is the most accurate statistical distribution to use when estimating the distribution of the crack widths of SHCC at the different tensile strains as shown in Figure 4.8 and Table 4.1.

The Coefficient of Determination determines how accurate a statistical distribution estimates the distribution of the crack widths, but it does not indicate which values are over estimated and under estimated. The Quantile-Quantile plots on the other hand give a graphical estimation on which values are over estimated and under estimated. In Appendix B the Quantile-Quantile plots for the Gamma distributions with a lower boundary, $x_0 = 20 \mu\text{m}$, are given at the different tensile strains for all the tests.

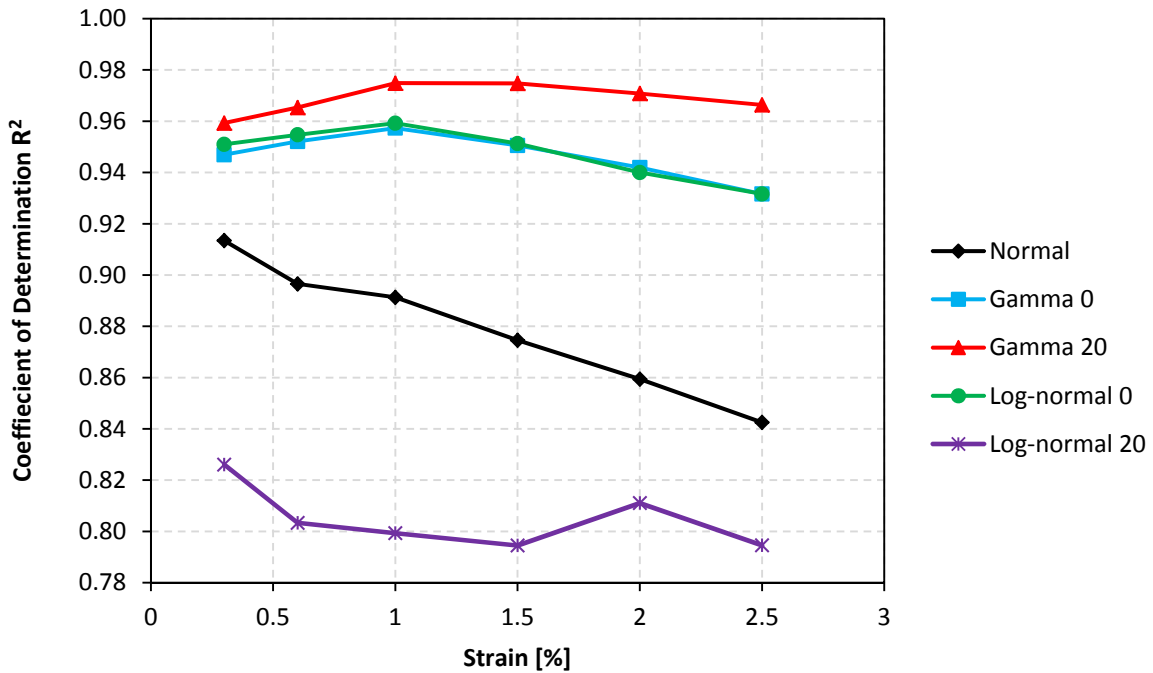


Figure 4.8: The average Coefficient of Determination plotted against the tensile strain for the different statistical distributions.

In Figure 4.9 a) to f) the Quantile-Quantile plots for the Gamma distribution with a lower boundary, $x_0 = 20 \mu\text{m}$, at the different tensile strains for Test 4 given in Appendix B are shown. It is observed that all the Quantile-Quantile plots for the Gamma distribution with lower boundary, $x_0 = 20 \mu\text{m}$, have similar shapes as indicated in Figure 4.9 a) to f). In the Quantile-Quantile plots for the Gamma distribution with a lower boundary, $x_0 = 20 \mu\text{m}$, it can be seen that both the small crack widths and the widest crack widths are over estimated whereas the mediate crack widths are fairly accurately estimated.

The Gamma distribution is dependent on two parameters, namely α and β , the equation for α and β is given in Equation 2.18. The parameters α and β is dependent on the mean (μ) and the standard deviation (σ) and the equations of the regression lines in Figures 4.4 and 4.5 were used to calculate both the mean and standard deviation at the different tensile strains. This in turn was used to determine the parameters α and β at the different tensile strains as shown in Table 4.2 that gives a summary for the parameters α and β at the different tensile strains. With the given Gamma parameters the Crack Width Distribution function (CWD_f) can be calculated and the probability of a certain crack width can be calculated at a certain tensile strain. Equation 4.1 gives the CWD_f for SHCC. Because α and β are dependent on the mean

and the standard deviation and the mean and the standard deviation are in turn dependant on the tensile strain, the only two variables in Equation 4.1 are the tensile strain and the crack width that are provided by the user.

$$CWD_f(x) = \frac{[x-20]^{\alpha-1}}{\beta^{\alpha}\Gamma(\alpha)} \exp\left[-\frac{(x-20)}{\beta}\right] \quad \text{Eq. 4.1}$$

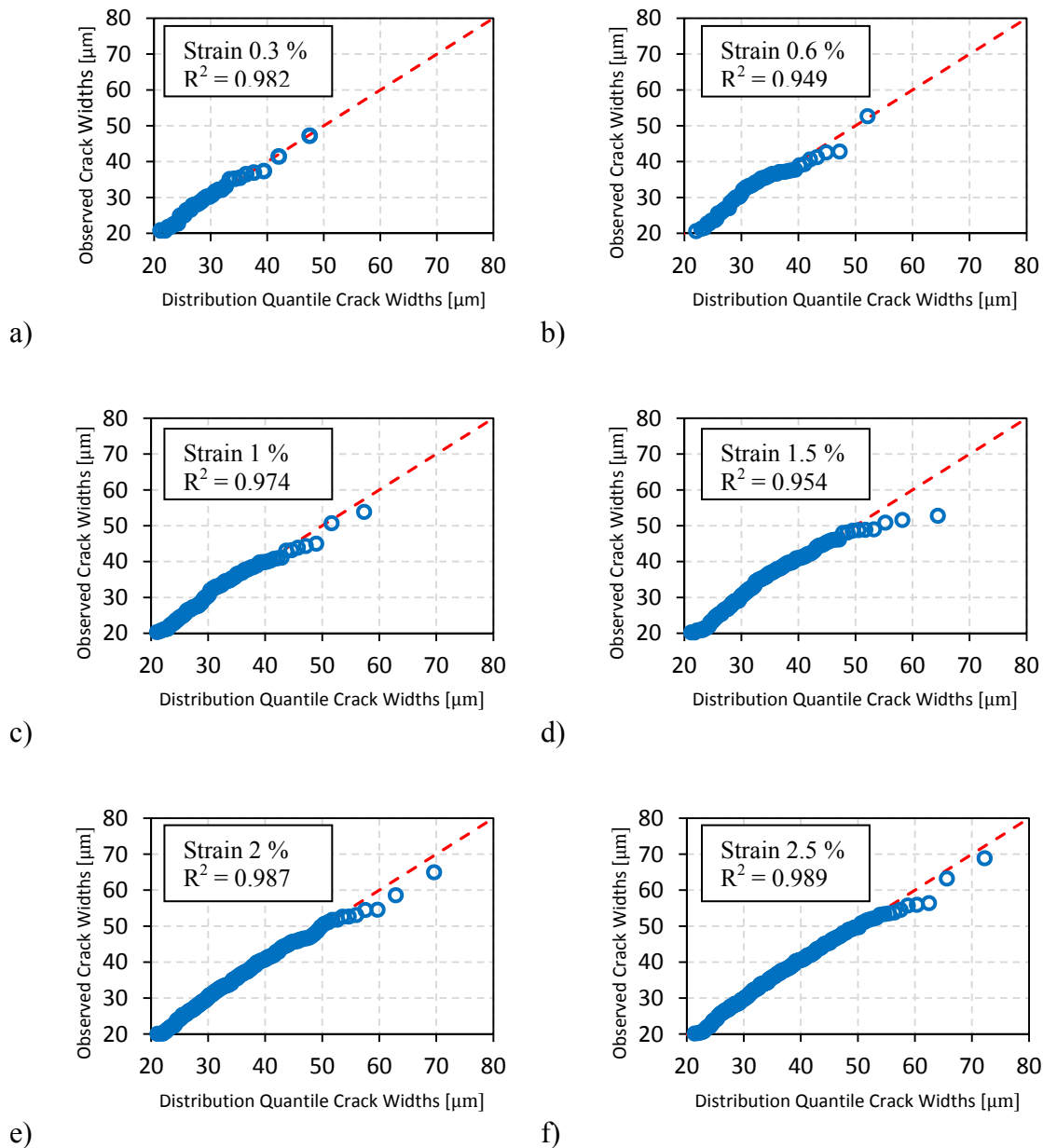


Figure 4.9: a) Quantile-Quantile plot at 0.3 % tensile strain. b) Quantile-Quantile plot at 0.6 % tensile strain. c) Quantile-Quantile plot at 1 % tensile strain. d) Quantile-Quantile plot at 1.5 % tensile strain. e) Quantile-Quantile plot at 2 % tensile strain. f) Quantile-Quantile plot at 2.5 % tensile strain.

Table 4.2: Summary of the dependant parameters for the Gamma distribution with lower bound, $x_0 = 20 \mu\text{m}$, at different tensile strains.

Strain [%]	α	β	$\Gamma(\alpha)$
0.3	1.891	6.107	0.959
0.6	1.704	8.003	0.909
1	1.611	9.420	0.895
1.5	1.554	10.553	0.889
2	1.520	11.361	0.887
2.5	1.496	11.989	0.886

In Figure 4.10 the CWD_f for the values in Table 4.2 are plotted. Figure 4.9 shows that the CWD_f is less steep and skewer at increasing tensile strain.

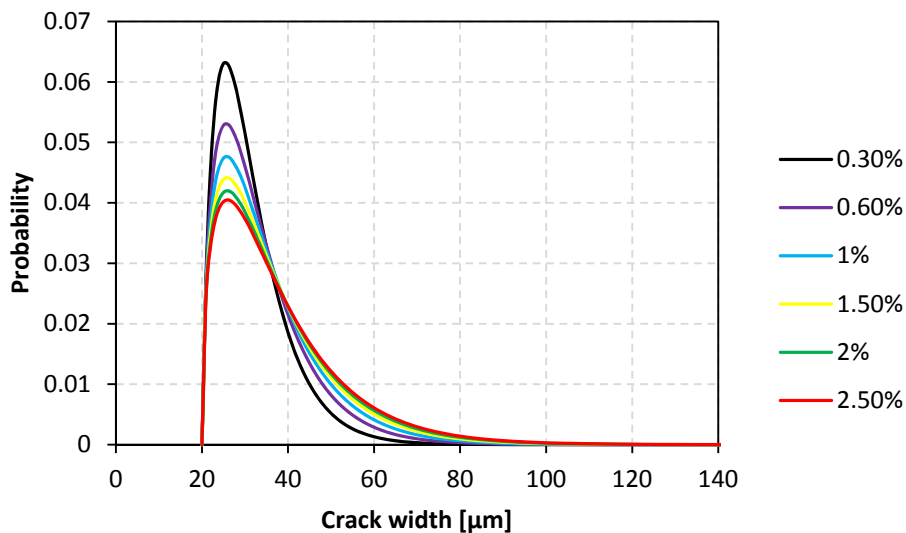


Figure 4.10: The CWD_f for SHCC at different tensile strains.

4.3.3 Mathematical Description of the Crack Pattern

The development of the crack pattern as the strain increases is not completely random but develops in a certain order. The order of the development of the cracks is not always the same and is dependent on the variations in the material, which makes it a difficult task to quantify the crack pattern development of SHCC. The crack pattern has an effect on the durability of the material and therefore needs to be quantified. Under this section a method is presented and demonstrated on how the crack pattern of SHCC can be quantified. A new parameter is

defined namely the Crack Proximity Index (*CPI*), which is a mathematical expression to describe the distances of the cracks to each other.

The expression for the *CPI* is based on the 2nd moment of inertia also known as the area moment of inertia. The mathematical expression of the 2nd moment of inertia has the form, $\int y^2 dA$. The distance y is the distance from the centroid of the infinitesimal area dA to the neutral axis. For more information and for the derivation of the 2nd moment of inertia refer to Hibbeler (2005).

Figure 4.11 shows the crack width along the specimen gauge length. The crack widths were calculated from the ARAMIS data for the middle section line.

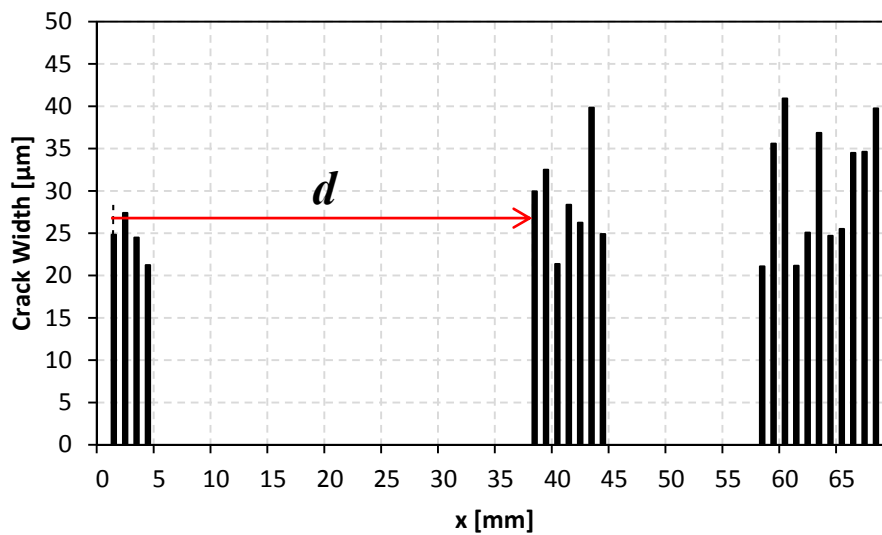


Figure 4.11: The crack width along the middle section line as function of position along the gauge length x .

The effect of a certain crack on the other cracks in terms of the crack spacing at a certain tensile strain can be determined as follows:

$$CPI_i = \sum_{j=1}^{n-1} C_{wi} \left(\frac{1}{d_j^2} \right) \quad \text{Eq. 4.2}$$

Where CPI_i is the crack proximity of a certain crack i relative to the other cracks j , C_{wi} is the width of the crack i , d is the distance from crack i to crack j and n is the number of cracks.

Note that in Equation 4.2 the distance from a crack i to the crack j is inversed $\left(\frac{1}{d_j^2} \right)$. The

explanation for this is that when the cracks are closer to each other the CP_i must increase and consequently where the cracks are further away from each other the CP_i must decrease; this is done by multiplying the width of crack i with the consecutive inverse distance squared $\left(\frac{1}{d_j^2}\right)$ of the other cracks j . The distance d is squared so that it represents a quadratic relationship. It still needs to be further investigated to which power it should be and would be determined by the effect the cracks has on each other, which is related to the distances between the cracks.

The CP_i for each crack was calculated using Equation 4.2, the average for all the CP_i was then calculated to obtain the CPI and is expressed as follows:

$$CPI = \frac{\sum_{i=1}^n CP_i}{n} = \frac{\sum_{i=1}^n \sum_{j=1}^{n-1} \left(c_{wi} \frac{1}{d_j^2} \right)}{n} \quad \text{Eq. 4.3}$$

The CPI as set out in Equation 4.3 was calculated for each specimen. In Figure 4.12 the average, minimum and maximum CPI values are plotted at different tensile strains. The coefficient of variation expressed in percentage at each tensile strain is also indicated. In Figure 4.12 the average CPI increases as the strain increases and it was established that a 117.66 % increase in the average CPI occurred as the strain increased from 0.3 % to 2.5 %. This increase in the CPI is ascribed to the fact that at lower strain levels the cracks are not closely spaced, but as the strain increases additional cracks form that are more closely spaced to each other. The average CPI in Figure 4.12 is best described by a logarithmic equation also given in Figure 4.12.

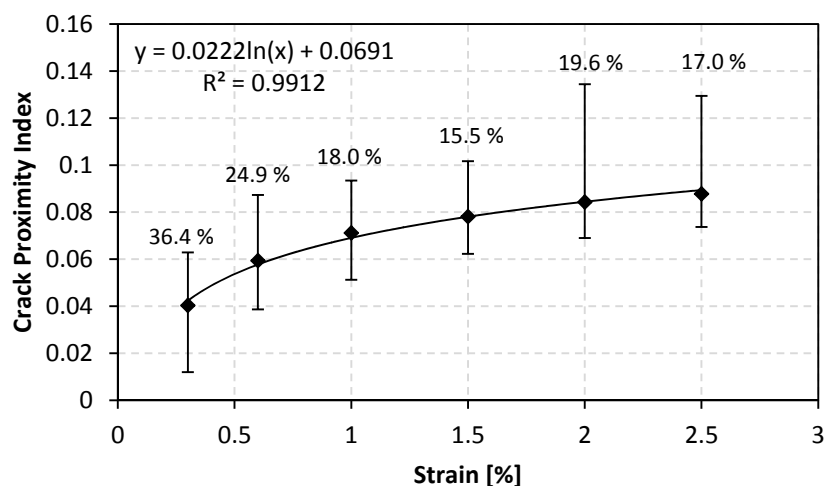


Figure 4.12: The average, maximum, minimum and coefficient of variation of the CPI at different tensile strains.

In Figure 4.13 the *CPI* for three different tests at different tensile strains are shown together with the strain surface contours at 1 % tensile strain, refer to Appendix B for the *CPI* test data for each test that was conducted.

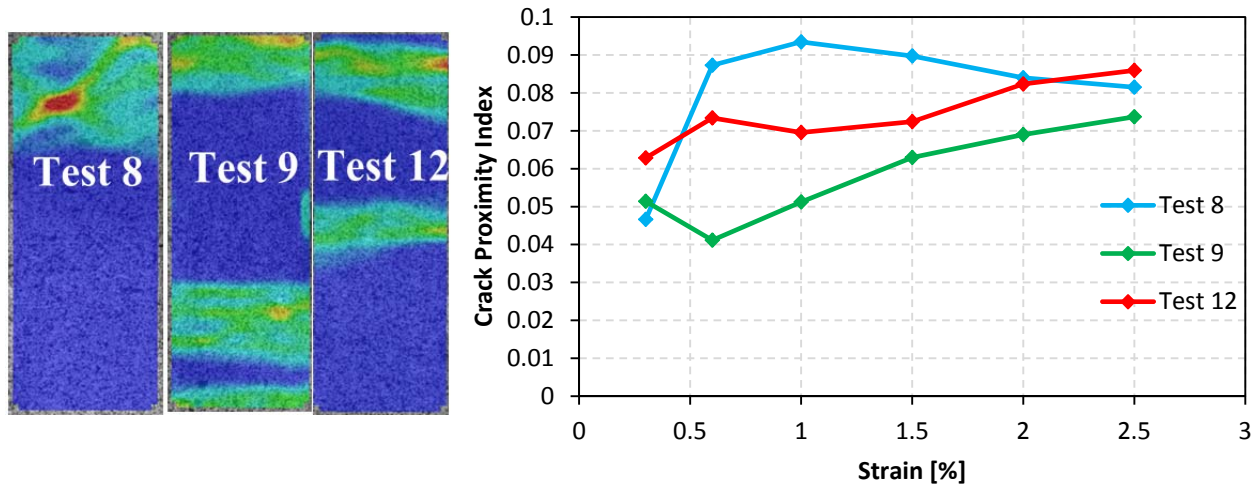


Figure 4.13: CPI for three different tensile tests and the surface contours at 1 % tensile strain.

Figure 4.13 indicates that at the same tensile strain different crack patterns can be observed. The crack patterns for the 3 different tests shown in Figure 4.13 differ significantly at 1 %. This is evident in the strain surface contours shown in Figure 4.13. The average *CPI* therefore cannot be used to quantify the crack pattern of SHCC at the different tensile strains as the crack pattern can differ significantly at the same tensile strain, thus a statistical distribution needs to be found that accurately describes the distribution of the *CPI* at different tensile strains. In Table 4.3 and Figure 4.14 the average Coefficient of Determination for the different statistical distributions are shown at the different tensile strains. The *CPI* of all fourteen specimens was used to find the most suitable statistical distribution that best describes the distribution of the *CPI* at the different tensile strains. The Log-normal distribution with lower boundary, $x_0 = 0$, describes the distribution of the *CPI* the best at the different tensile strains, except at 0.3 % tensile strain which is best described by the Normal distribution, however the Log-Normal distribution can also be used to describe the distribution of the *CPI* at 0.3 % tensile strain.

Table 4.3: The average Coefficient of Determination for the different statistical distributions used to describe the *CPI* at different tensile strains.

Distribution	Strain	Coefficient of Determination					
		0.3%	0.6%	1%	1.5%	2%	2.5%
Normal		0.973	0.953	0.965	0.951	0.720	0.795
Gamma		0.932	0.970	0.973	0.965	0.775	0.844
Log-Normal		0.754	0.971	0.973	0.968	0.799	0.863
Best		Normal	Log-Normal	Log-Normal	Log-Normal	Log-Normal	Log-Normal

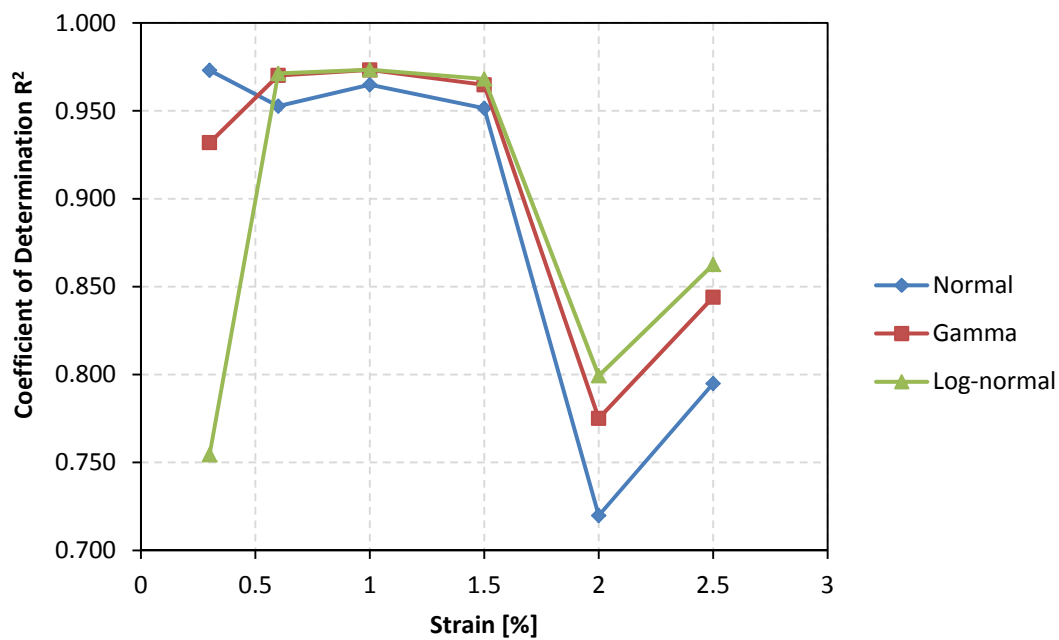


Figure 4.14: The average Coefficient of Determination plotted against the tensile strain for the different statistical distributions.

The Log-normal distribution is dependent only on two parameters, namely the mean (μ) and standard deviation (σ) and is the mean and standard deviation of $Y = \ln(x)$, refer Section 2.2.2.2 for a description of the parameters. In Table 4.4 the mean and standard deviation for the Log-Normal distribution is given at the different tensile strains.

Thus with the parameters given in Table 4.4 the probability that a certain *CPI* will occur at a certain tensile strain can be calculated, this is shown in Figure 4.15 for the distributions of the *CPI* at the different tensile strains.

Table 4.4: Summary of the dependent parameters for the Log-normal distribution with lower boundary, $x_0 = 0$ at different tensile strains.

Strain %	Mean μ	Stdev σ
0.3	-3.2927	0.4577
0.6	-2.8519	0.2464
1	-2.6580	0.1788
1.5	-2.5610	0.1527
2	-2.4881	0.1702
2.5	-2.4449	0.1537

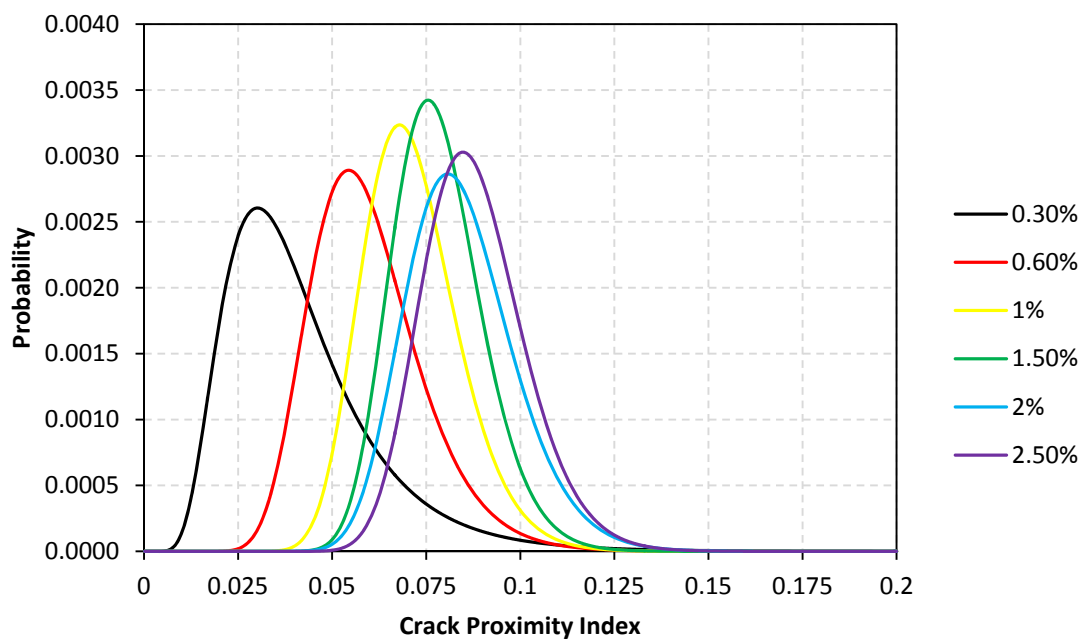


Figure 4.15: The distribution of the *CPI* (Log-normal distribution with lower boundary, $x_0 = 0$) at different tensile strains.

Figure 4.15 shows that the steepness increases as the tensile strain increases and that the standard deviation decreases as the tensile strain increases. The reason for this is that more cracks form when the tensile strain increases and the spacing between the cracks become more evenly spaced. This is explained in Figure 4.12, as the tensile strain increases the average *CPI* increases.

Figure 4.16 and 4.17 shows the average and the standard deviation of the *CPI* plotted against the average of the average crack width and is fitted with a linear regression line.

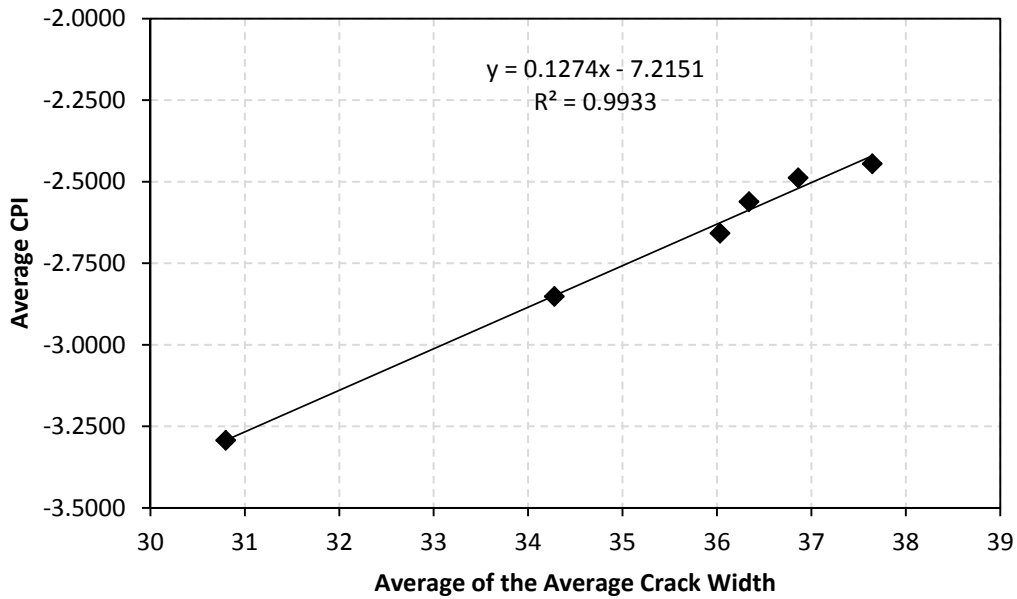


Figure 4.16: The mean of the *CPI* plotted against the average of the average crack width.

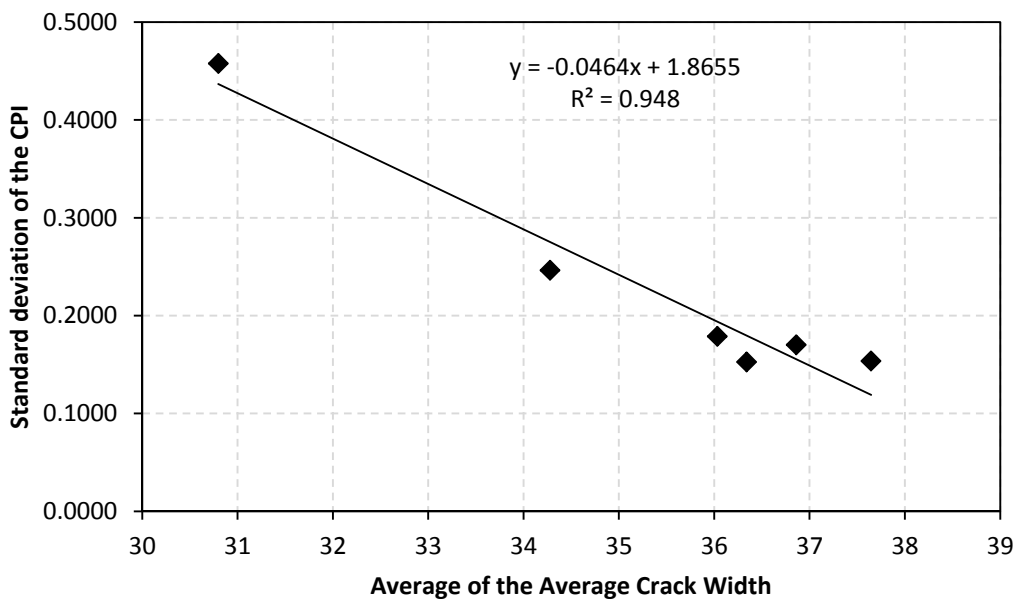


Figure 4.17: The standard deviation of the *CPI* plotted against the average of the average crack width.

Figure 4.16 and Figure 4.17 shows that the mean and the standard deviation of the *CPI* can be estimated from the average of the average crack width with reasonable accuracy. This means that the parameters of the Log-normal distribution that describes the distribution of the *CPI* can be calculated from the average of the average crack width.

4.4 Discussion

The coefficient of variation of the standard deviation and skewness is much higher than that of the average crack width and the number of cracks per meter. The explanation is that the standard deviation and skewness are the second central moment and third central moment respectively and thus are easily influenced by outliers.

In Table 4.1 it is shown that the Gamma distribution with a lower boundary, $x_0 = 20 \mu\text{m}$, is the best statistical distribution of the chosen distributions to describe the distribution of the crack widths. In Figure 4.10 the CWD_f is plotted at different tensile strains and the skewness increases as the strain increases. This is also supported in Figure 4.6 with the average skewness increasing as the tensile strain increases. The reason for this increase in skewness as the tensile strain increases is that at lower tensile strains more small cracks than larger cracks form. As the tensile strain increases new small cracks continue forming, but the number of larger cracks that is formed increases significantly that results in an increase in the standard deviation and the skewness. Figure 4.10 also shows that the steepness decreases as the tensile strain increases. This is because the probability that larger crack widths will form increases and the probability that small crack widths will form decreases as the tensile strain increases.

In Section 4.3.3 a method is presented on how to quantify the crack pattern and is termed the Crack Proximity Index (*CPI*). In Figure 4.12 the average *CPI* is plotted at different tensile strains and it was observed that the *CPI* increases as the tensile strain increase. The reason for this is that as the tensile strain increases the occurrence of additional cracks results in them being more frequently formed with less space between them and that is also why the coefficient of variation decreases as the tensile strain increases. In Figure 4.13 it is indicated that different crack patterns can be found at the same tensile strain and thus the average *CPI* is not a proper way to quantify the crack pattern. A statistical distribution model was therefore found to describe the *CPI* at different tensile strains. In Table 4.3 and Figure 4.14 it is proven that the Log-Normal distribution is the best distribution to describe the *CPI* at different tensile strains and in Figure 4.15 the distribution of the *CPI* (Log-normal distribution with lower boundary, $x_0 = 0$) at different tensile strains is plotted. The steepness increases and the standard deviation decreases as the tensile strain increases in Figure 4.15. This is attributed to the decrease in the crack spacing as the tensile strain increases. In Figure 4.16 and Figure 4.17 it is postulated that the parameters of the Log-normal distribution which

describes the *CPI* can be estimated from the average of the average crack width. This means that the *CPI* distribution of SHCC can easily be calculated from the experimental result, namely the average of the average crack width.

CHAPTER 5

APPLICATION OF QUASI-STATIC TENSILE MODELS ON BENDING

Concrete structural elements are mainly subjected to bending and not to direct tension, therefore the quantification of the cracking behaviour under flexural loading needs to be investigated. The scope of this research topic is to apply the tensile crack width distribution model (Gamma distribution with lower boundary, $x_0 = 20 \mu\text{m}$) on bending and to confirm whether the same crack width distribution model as in tension can be used for bending. An investigation was also conducted to check whether the crack pattern development in bending is the same as in tension. Four point bending tests were done on bending specimens to collect the cracking data. A four point bending setup was used, so that the central portion of the beam was subjected to pure bending moment. A brief description on four point bending is given in the next section.

5.1 Test Setup

Four point bending tests were performed in a Zwick Z250 Universal Materials Testing Machine in order for a comparison to be conducted against the theoretical tensile models. The Zwick four point bending setup was used that has a capacity of 250 kN. Figure 5.1 shows a photo of the four point bending test setup.

The loading points of the four point bending setup are designed to ensure that no extra moments will be transferred to the test specimen.

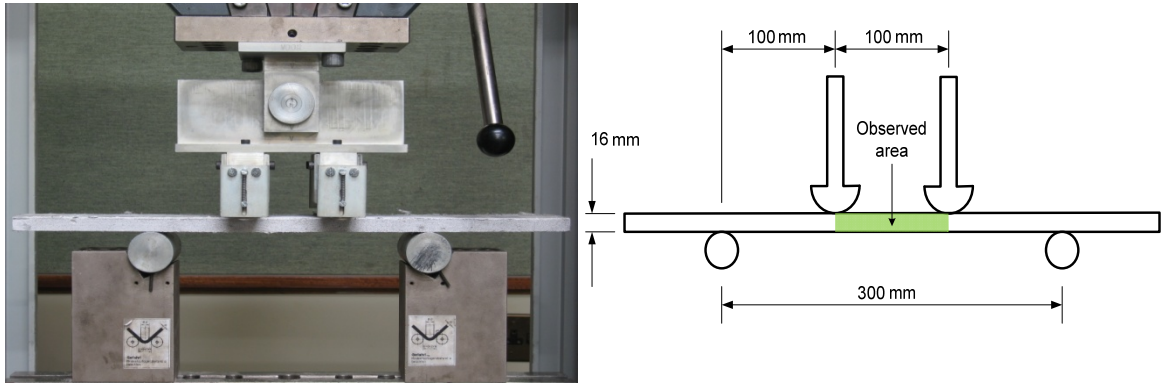


Figure 5.1: Four point bending setup with dimensions.

Thin beam specimens with a thickness of 16 mm were used during the four point bending test. The specimens were cast in steel beam moulds as shown in Figure 5.2 that includes the dimensions of the test specimens. The top side of the beam specimen during casting was retained as the top side of the beam during testing.

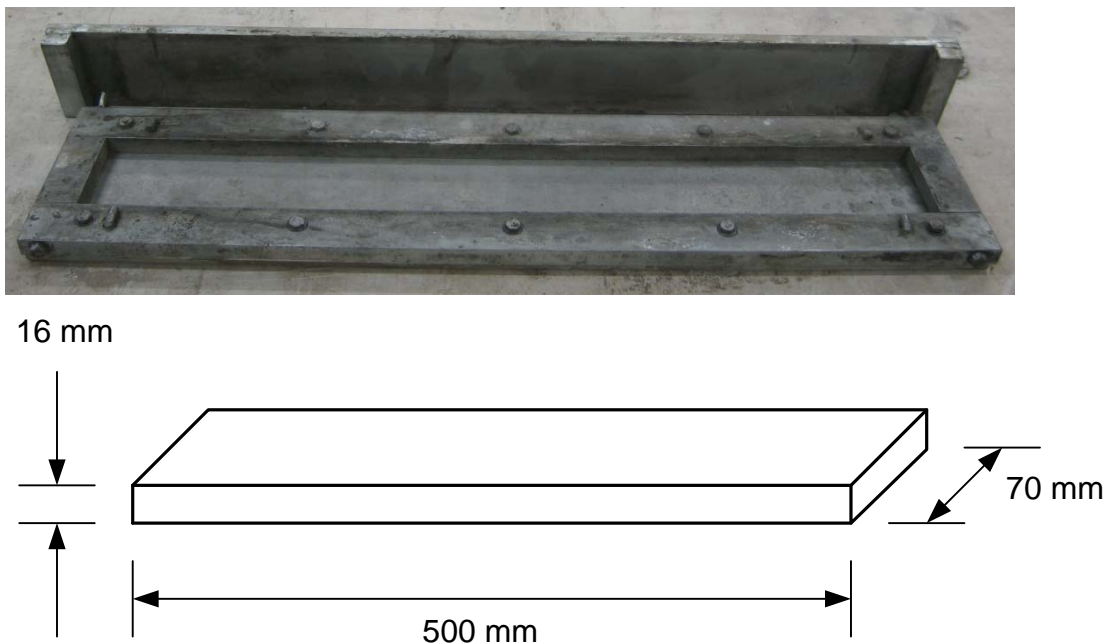


Figure 5.2: Picture of steel mould with dimensions of the beam specimens.

The tests were control by the displacement rate of the cross head of the Zwick and the load was measured using the load cell of the Zwick and the deflection was measured using the displacement of the cross head of the Zwick. The strain was measured with the aid of the

ARAMIS system. The same crack definition as in Chapter 3, with the exception of three section lines on the bottom side edge of the observed area, was used to calculate the crack widths. The observed area is shown in Figure 5.1. The strain was measured at the same position as where the crack widths were calculated. The strain was calculated by taking the average strain of the three section lines. Figure 5.3 shows a strain contour view of the observed area with an enlarged area to indicate where the section lines were chosen.

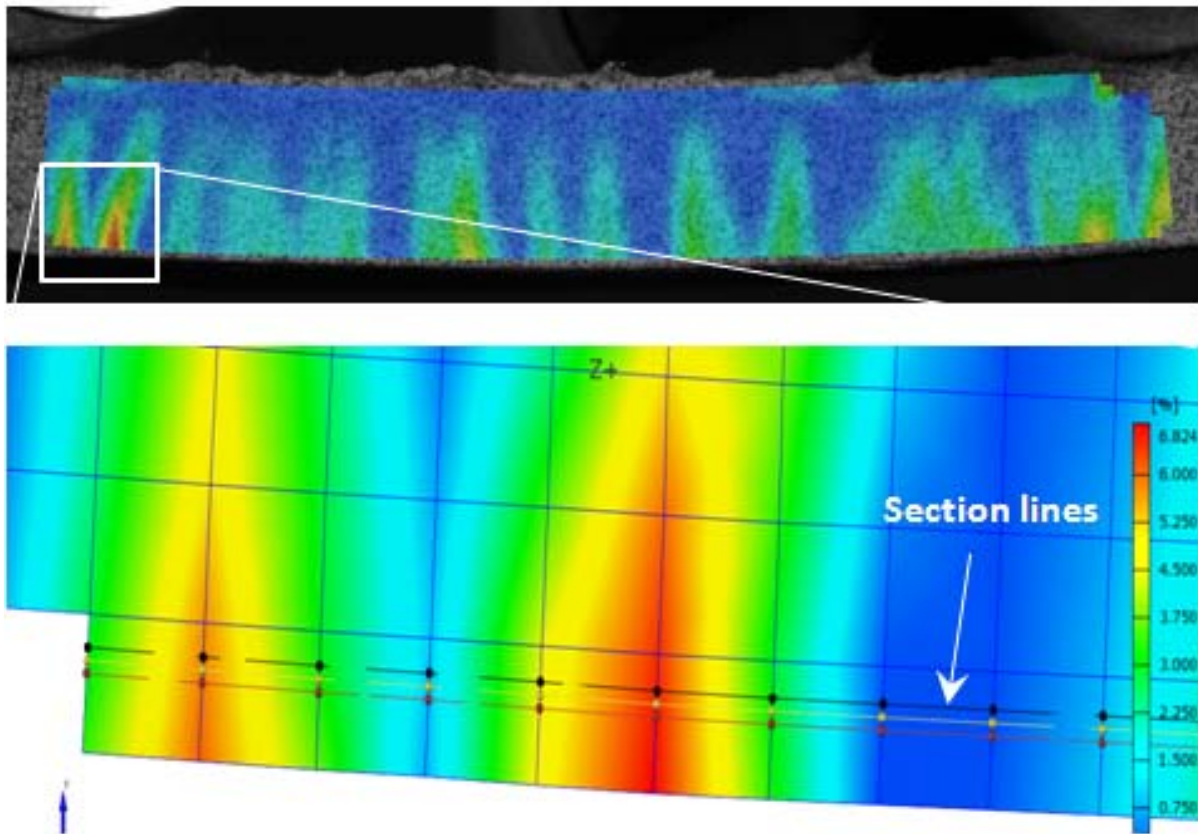


Figure 5.3: Strain contour view of a observed area and an enlarge view of the strain contour view to indicate where the section lines were chosen.

The shear force and bending moment diagrams of a typical four point bending test are as shown in Figure 5.4. The bending moment is constant between the two loading points. This means that the cracks that form in that area are pure flexural cracks. It was from this area that the cracking data was collected for comparison with the cracking behaviour under quasi-static tensile loading.

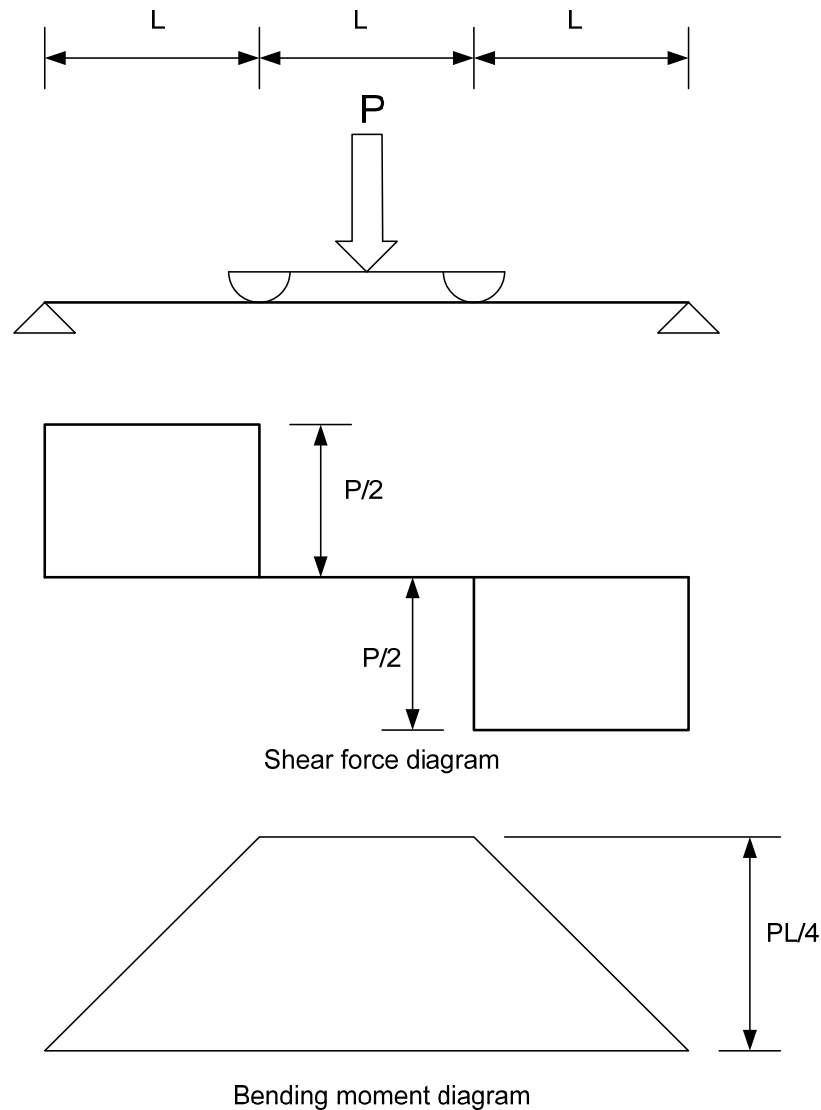


Figure 5.4: Shear force diagram and bending moment diagram for a four point bending setup.

5.2 Experimental Test Program

The specimens were prepared using the same mixing procedure and proportions as detailed in Section 3.3. Prior to testing the side of the beam was painted with a thin limestone layer onto which the speckle pattern was spray painted with black aerosol spray-paint to create a stochastic pattern. This was necessary for the ARAMIS system, refer to Section 3.1. Figure 5.5 shows a beam specimen with the limestone and the stochastic pattern. Four beam specimens were cast and tested. The flexural tests were done at a deflection rate of 0.02 mm/s.



Figure 5.5: Photo of a beam specimen with painted limestone and stochastic speckle pattern.

5.3 Results

The force-deflection responses of the four specimens are shown in Figure 5.6. The specimens were not loaded until failure due to the limitation of the ARAMIS system; it is only able to take 780 images with a frame rate of one image per second with the result that the test took a maximum of 13 minutes. At the selected loading rate the specimen had not failed before 13 minutes and the tests were subsequently terminated after 13 minutes had expired.

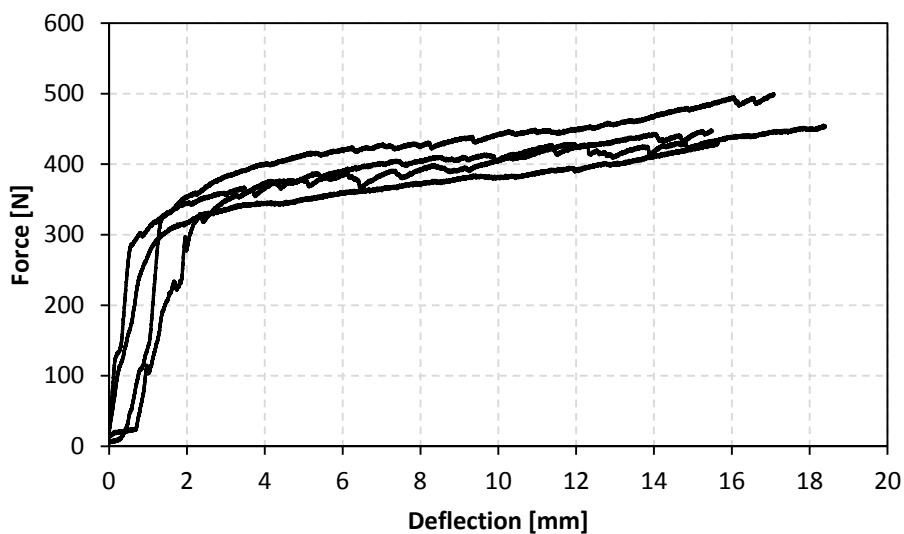


Figure 5.6: Force-deflection response of bending test specimens.

5.4 Bending Cracking Behaviour vs. Tensile Cracking Behaviour

In Figure 5.7 the average number of cracks formed during the bending tests is compared with the average number of cracks formed during the quasi-static tensile tests as was done in

Section 4.3.1. The number of cracks per metre at different strains for each bending test is shown in Appendix C. It is evident that the average number of cracks per metre in bending is lower than in tension for strains up to 1.5 % and for strains higher than 1.5 % the average number of cracks per metre is approximately the same in both bending and tension.

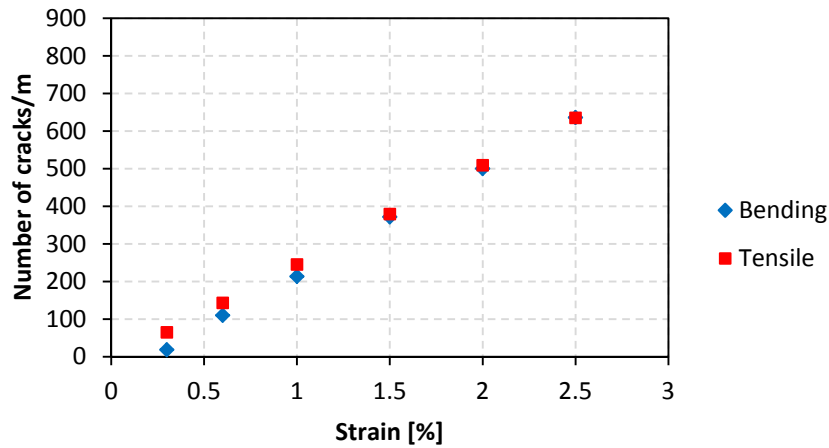


Figure 5.7: Comparison between the average number of cracks per metre for bending and tensile tests.

In Figure 5.8 the average of the average crack width of the bending tests is compared against the average of the average crack width of the quasi-static tensile tests as was done in Section 4.3.1. The average crack width at different strains for each bending test is shown in Appendix C. It was observed that the average of the average crack width in bending is lower than that found for tension for strains up to 1.5 %, whereas the average of the average crack width at strains higher than 1.5 % is about the same for both bending and tension.

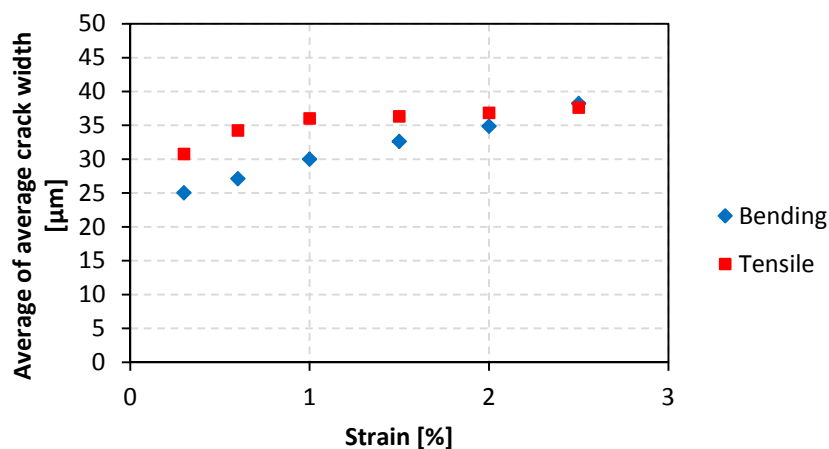


Figure 5.8: Comparison between the average of the average crack width for bending and tensile tests.

In Figure 5.9 the average standard deviation of the crack widths of the bending tests is compared against the average standard deviation of the crack widths of the quasi-static tensile tests as was done in Section 4.3.1. The standard deviation at different strains for each bending test is shown in Appendix C. The average standard deviation for bending is lower than in tension for strains up to 1.5 %, however at strains higher than 1.5 % it is about the same for bending and tension.

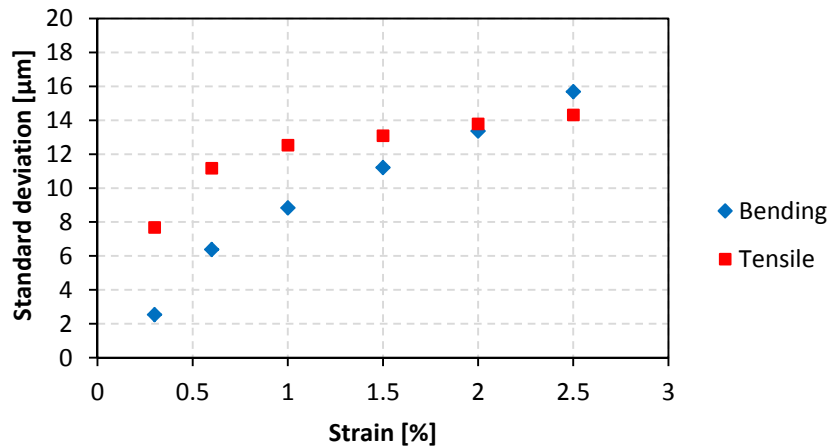


Figure 5.9: Comparison between the average standard deviation for bending and tensile tests.

In Figure 5.10 the average skewness of the crack widths of the bending tests is compared against the average skewness of the crack widths of the quasi-static tensile tests as was done in Section 4.3.1. It can be seen that the average skewness is lower in bending than in tension, for strains up to 2.5 %. The skewness at different strains for each bending test can be found in Appendix C.

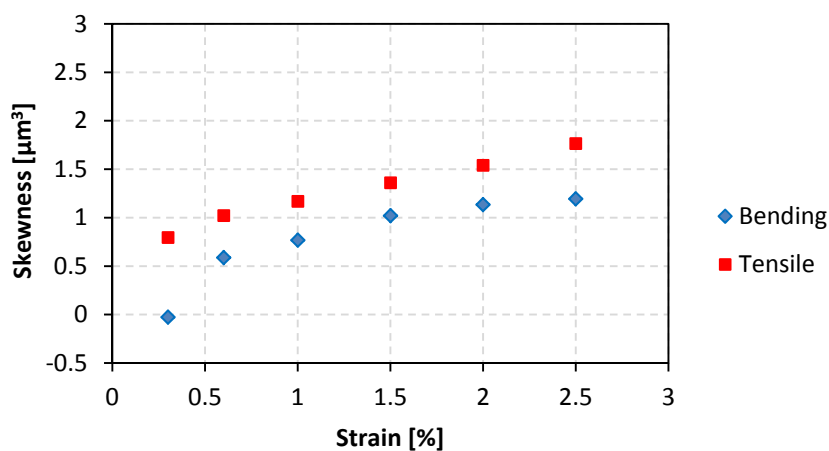


Figure 5.10: Comparison between the average skewness for bending and tensile tests.

In order to compare the tensile crack width distribution model (Gamma distribution with lower boundary, $x_0 = 20 \mu\text{m}$) with the crack widths calculated from the ARAMIS data for the flexural tests the Quantile-Quantile plots were used to calculate the Coefficient of Determination at different strains for each test. In the Quantile-Quantile plots the observed bending crack widths were plotted against the crack widths calculated from the theoretical tensile crack width distribution model (Gamma distribution with lower boundary, $x_0 = 20 \mu\text{m}$). If the theoretical tensile crack width distribution model determines the observed bending crack widths considerably, the data points can be fitted with the regression line, $y = x$. The Coefficient of Determination will thus give a good representation of how well the data fits on the line $y = x$. In Table 5.1 a summary of the Coefficient of Determination for each test at different strains is given.

In Figure 5.11 a) to d) the Quantile-Quantile plots at the different strains are given for each test. The Coefficient of Determination is given in brackets for each strain.

Table 5.1: A summary of the Coefficient of Determinations for each flexural test at different tensile strains.

Test no. \ Strain	Coefficient of Determination					
	0.30%	0.60%	1%	1.50%	2%	2.50%
1	0	0	0	0.642	0.895	-
2	0	0.245	0.289	0.522	0.684	0.911
3	0	0	0.456	0.819	0.938	0.940
4	0.519	0.484	0.881	0.963	0.944	0.920
Average	0.130	0.183	0.407	0.736	0.865	0.924

Table 5.1 and Figure 5.11, shows that for lower strains up to 1.5 % the Coefficient of Determination is relatively low compared to the Coefficient of Determination for strains higher than 1.5 %. This indicates that the theoretical tensile model (Gamma distribution with lower boundary, $x_0 = 20 \mu\text{m}$) is not a good representation of the crack width distribution for bending. It can also be seen in Figure 5.11 a) to d) that the theoretical tensile model over estimates the crack widths for bending at strains up to 1.5 % and Figure 5.8 confirms this, because it shows that the average of the average crack width is higher for tension than for bending at strains up to 1.5 %.

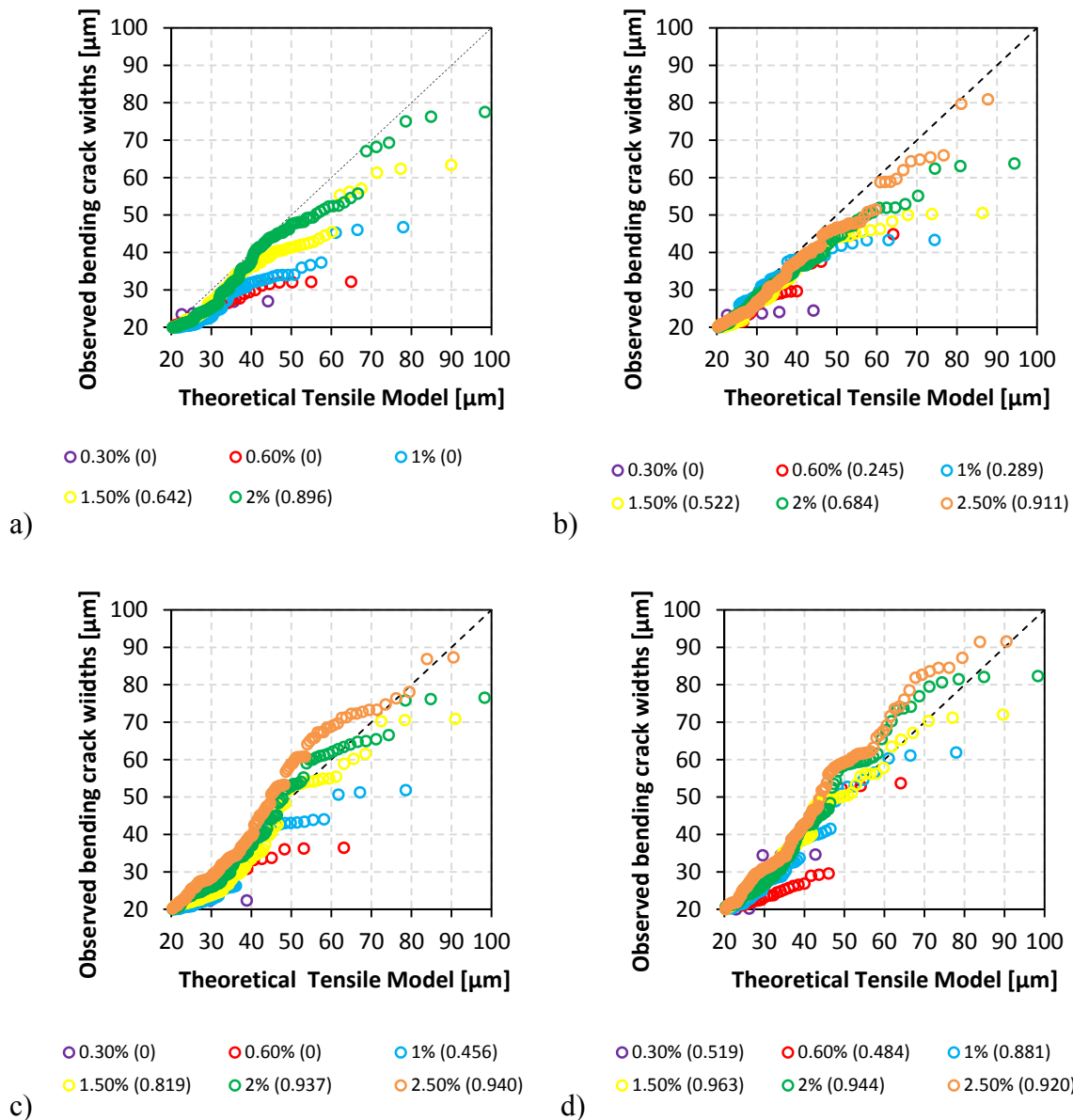


Figure 5.11 a) – d): The observed bending crack widths plotted against the theoretical tensile model for bending test 1, 2, 3 and 4, respectively.

5.5 Bending Crack Pattern vs. Tensile Crack Pattern

In Figure 5.12 the average crack proximity index (*CPI*) for bending is compared to the average *CPI* for tension as was done in Section 4.3.3. The *CPI* at the different strains for each bending test can be found in Appendix C. The *CPI* is lower for bending than for tension, which means that the cracks are more evenly spaced in bending than in tension.

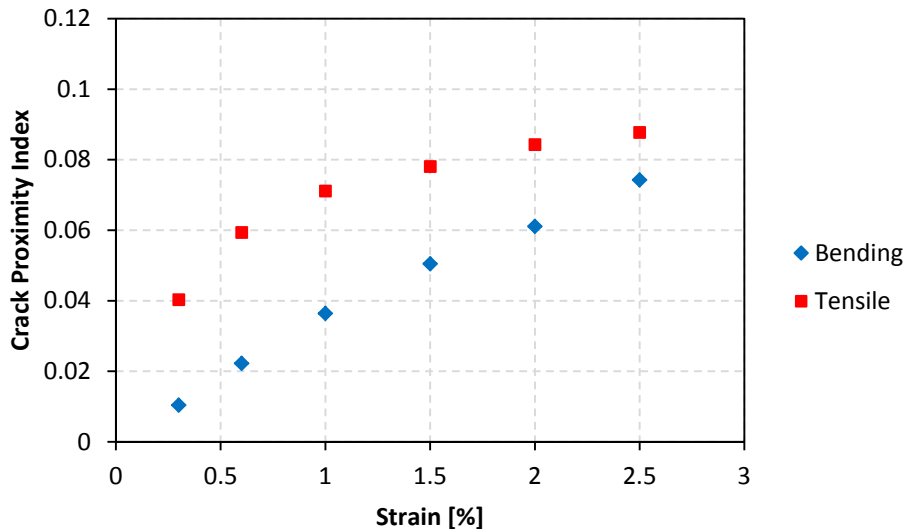


Figure 5.12: Comparison between the average CPI for bending and tensile tests.

5.6 Discussion

The average of the average crack width in bending is lower than in tension up to 1.5 % strain. At strains higher than 1.5 % the average of the average crack width is about the same for both bending and tension. This means that on a single crack level SHCC will be more durable in bending than it would be in direct tension for strains up to 1.5 %. The average number of cracks per metre is also lower in bending than in tension at strains up to 1.5 %; and for strains higher than 1.5 % it is about the same in both bending and in tension. The average standard deviation of SHCC is lower in bending than in tension for strains up and to 1.5 %. This indicates that the bending ratio between small and larger flexural cracks is higher when compared to those found in tension and explains why the average of the average crack width is also lower in bending than in tension at strains up to 1.5 %. This means that the probability that a larger crack will form is lower in bending than in tension. This assumption is supported by the skewness as the average skewness in bending is lower than in tension. This further explains why the average of the average crack width is smaller in bending than in tension as the lower the skewness the higher is the ratio between the number of small cracks to the number of larger cracks formed.

In Figure 5.11 the observed bending crack widths are plotted against the theoretical tensile model (Gamma distribution with lower boundary, $x_0 = 20 \mu\text{m}$) and it can be seen that the

theoretical tensile model over estimates the crack widths for strains up to 1.5 %. For strains higher than 1.5 % the theoretical tensile model gives a fairly accurate estimation of the crack widths observed in bending. This can be seen in Table 5.1 for the average Coefficient of Determination of the four tests. The explanation why the theoretical tensile model over estimates the flexural crack widths for strains up to 1.5 % is the difference in the mean and the standard deviation of the crack widths between bending and tension. The mean and standard deviation are used to calculate the parameters of the Gamma distribution which will result in the parameters in bending being different from the parameters in tension.

The average *CPI* is lower for bending than for direct tension, which means that the cracks are more evenly spaced in bending than in tension. The fact that the cracks are more evenly spaced in bending than in tension and that the average of the average crack width is lower in bending than for tension for strains up to 1.5 %, indicates that SHCC may be even more durable under flexural loading than in direct tension. A possible reason why the *CPI* in bending is smaller compared to tension is because a larger area of cracks was observed during the measuring of the flexural cracks.

It can be concluded that the theoretical tensile models that describe the crack widths (Gamma distribution with lower boundary, $x_0 = 20 \mu\text{m}$) and the *CPI* (Log-normal distribution with lower boundary, $x_0 = 0$) in this research project, cannot be used to describe the cracking behaviour of SHCC under flexural loading. A difference is found in the crack width, number of cracks and the crack pattern between bending and tension. The crack widths were measured from the side at the bottom edge of the specimen (see Figure 5.3) during the flexural tests. The alignment of the fibres at the edges is different than in the rest of the specimen and this may be a possible reason why the crack widths are different in bending compared to tension. In Figure 5.13 it is shown that not all the cracks can be measured from the side of the specimen and this is a possible reason why there is a slight difference in the number of cracks per metre. Further investigation under flexural loading needs to be done in the near future to better describe the cracking behaviour of SHCC. A test setup also needs to be designed so that the cracks can be observed from the bottom view during flexural testing as shown in Figure 5.13. This will give more accurate flexural cracking data compared to the cracking data that was measured during this research project.

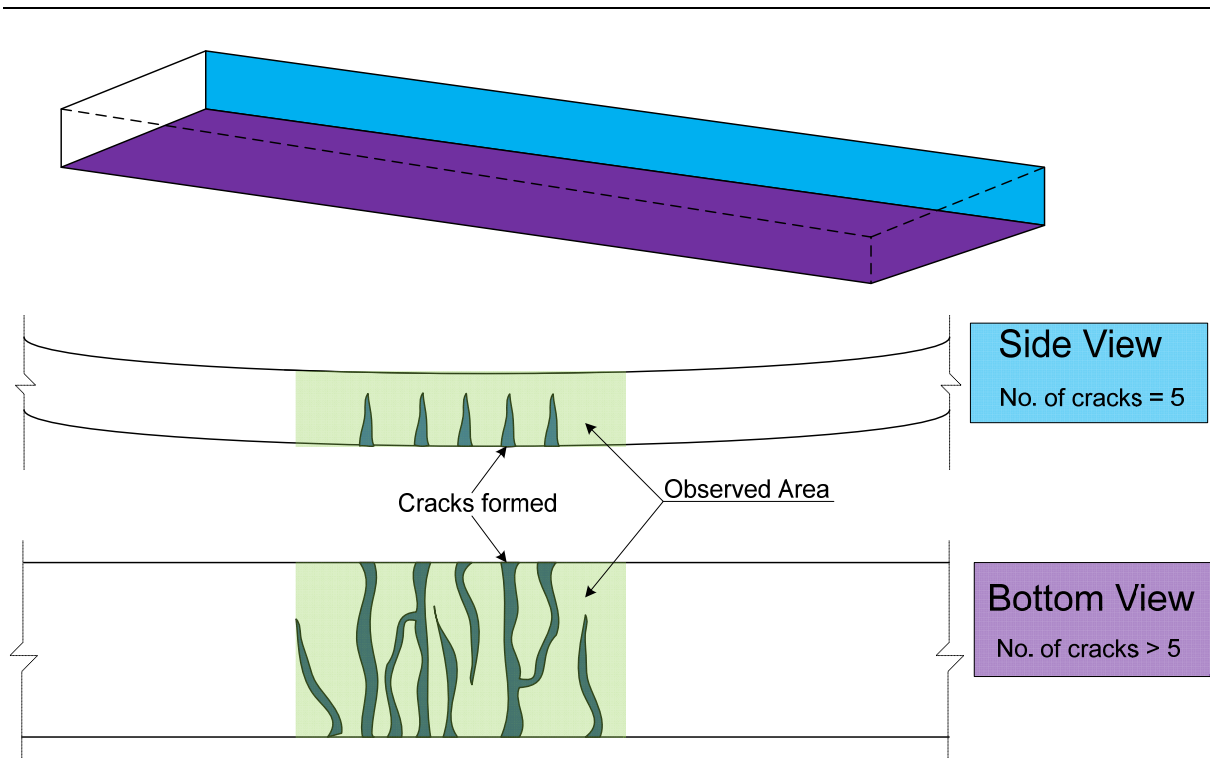


Figure 5.13: The difference between the number of the cracks at the side and bottom of the specimen.

CHAPTER 6

CONCLUSIONS AND FUTURE DEVELOPMENTS

6.1 Conclusions

The objective of this research project was to quantify the cracking behaviour of SHCC under quasi-static tensile loading. In order to achieve this, the cracking behaviour of SHCC is described by some descriptive statistical parameters that are used to find a statistical distribution to describe the crack width distribution and a mathematical expression to quantify the crack pattern.

The statistical distribution that best describes the crack width distribution of SHCC under quasi-static tensile loading is the Gamma distribution with a lower boundary, $x_0 = 20 \mu\text{m}$. It was however noticed that the Gamma distribution with lower boundary, $x_0 = 20 \mu\text{m}$, over estimates both the small crack widths and the widest crack widths and estimates the mediate crack widths fairly accurately.

A new parameter was defined by a mathematical expression that describes the distances of the cracks to each other namely the Crack Proximity Index (*CPI*). It was found that the *CPI* increases as the strain increases; this is an indication that more cracks form as the strain increases thus reducing the crack spacing. A large variation in the *CPI* was found at different tensile strains, thus the average *CPI* could not be used to quantify the crack pattern of SHCC. To quantify the *CPI* a statistical distribution model was derived that best describes the *CPI* at different tensile strains, namely the Log-Normal distribution, with lower boundary, $x_0 = 0$. It is shown that the dependant parameters of the Log-normal distribution can be calculated from the average of the average crack width. This means that the *CPI* distribution of SHCC can be calculated from the experimental result, namely the average of the average crack width.

Concrete structures are mostly subjected to bending rather than direct tensile loading. A study was done to compare the cracking behaviour of quasi-static tensile loading against the cracking behaviour of bending to establish whether the tensile models can be used to describe the bending cracking behaviour. It was found that the cracking behaviour is different in bending than in tension and that the tensile models are not a good representation of the cracking behaviour in bending.

6.2 Future Developments

This research project gave rise to research work that must be done in the future so that SHCC can be used efficiently and for the correct purpose. The following are identified as important matters that should be further investigated.

- All specimens were tested at an age of 14 days. A few older specimens were tested and it was found that the specimens were more brittle than the 14 day old specimens. To get a more accurate representation of the cracking behaviour of SHCC over time, cracking data should also be collected on older specimens.
 - The observed area of the specimen was 80 x 30 mm. The thickness of the observed area of the specimen was 15 mm. The results of this specimen size would be a good representation of thin structural elements, but for thicker structural elements, larger and thicker specimen should be investigated. These specimens may show a different cracking behaviour because of the difference in fibre orientation between a thin specimen and a thick specimen. In a thin specimen the fibres are forced in a certain direction but in a thicker specimen the fibres are more randomly distributed.
 - In this research project only the crack widths were taken in to consideration, but the crack depth will also have an effect on the durability and should be included in future investigations. This is even more significant in flexure.
-

CHAPTER 7

REFERENCES

- Adendorff, C.J., 2009. *Time-Dependant Cracking Behaviour of Strain Hardening Cement-based Composite*. MSc Thesis. Stellenbosch University.
- Adendorff, C.J., Boshoff, W.P. & van Zijl, G.P.A.G., 2010. Characterisation of crack distribution of Strain-Hardening Cement Composites (SHCC) under imposed strain. *Advanced in Cement-based Materials*, 1(1), pp.215 - 221.
- Boshoff, W.P., 2007. *Time-Dependant Behaviour of Engineered Cement-based Composites*. PhD Thesis. University of Stellenbosch.
- Boshoff, W.P. & Adendorff, C.J., 2010. Modelling SHCC Cracking for Durability. *Fracture and Damage of Advanced Fibre-reinforced Cement-based Materials*, 1(1), pp.195-202.
- Bulmer, M.G., 1965. *Principles of Statistics*. United States of America, New York: Oliver & Boyd.
- Hibbeler, R.C., 2005. Moment of Inertia for an Area. In R.C. Hibbeler, ed. *Mechanics of Materials*. 6th ed. Singapore: Prentice-Hall. pp.799-802.
- Holicky, M., 2009. *Reliability analysis for structural design*. 1st ed. South Africa, Stellenbosch: SUN MeDIA Stellenbosch.
- Kato, E., Kato, Y. & Uomoto, T., 2005. Development of Simulation Model of Chloride Ion Transportation in Cracked Concrete. *Journal of Advanced Concrete Technology*, 3(1), pp.85-94.

-
- Lepech, M.D. & Li, V.C., 2009. Water permeability of engineered cementitious composites. *Cement & Concrete Composites*, 31, p.744–753.
- Li, V.C., 1992. Performance Driven Design of Fiber Reinforced Cementitious Composites. In Swamy, R.N., ed. *Proceedings of the 4th RILEM International Symposium on Fiber Reinforced Concrete.*, 1992. Chapman and Hall.
- Li, V.C., 2003. On Engineered Cementitious Composites. *Journal of Advanced Concrete Technology*, 1(3), pp.215 - 230.
- Li, V.C. et al., 2000. Repair and retrofit with Engineered Cementitious Composites. *Journal of Engineering Fracture Mechanics*, 65(2-3), pp.317 - 334.
- Lin, Z. & Li, V.C., 1997. Crack Bridging in Fibre Reinforced Cementitious Composites with Slip-Hardening Interfaces. *J. Mech. Phys.Solids*, 45(5), pp.763-87.
- Li, V.C., Wang, S. & Wu, C., 2001. Tensile Strain-Hardening Behaviour of Polyvinyl Alcohol Engineerd Cementitious Composites (PVA-ECC). *ACI Materials Journal*, 98(6), pp.483 - 492.
- Mechtcherine, V., Lieboldt, M. & Altmann, F., 2007. Preliminary Tests On Air-Permeability and Water Absorption of Cracked and Uncracked Strain Hardening Cement-Based Composites. *Proceeding of the International RILEM Workshop on Transport Mechanisms in Cracked Concrete*, pp.55-66.
- Montgomery, D.C. & Runger, G.C., 2007. *Applied Statistics and Probability for Engineers*. 4th ed. Bruce Spatz.
- Silva, F.A. et al., 2010. Mechanical behaviour of Strain-Hardening Cement-Based Composites (SHCC) under low and High tensile strain rates. *Fracture and Damage of Advanced Fibre-reinforced Cement-based Materials*, 1(1), pp.23-30.
-

APPENDIX A

MIX DESIGN

A.1 Introduction

The aim was to design a SHCC mix that would give an average strain capacity of more than 4 %. This mix will then be used to quantify the cracking behaviour of SHCC. The specimen preparation and the test setup was the same as described in Sections 3.3 and 3.4. The mix that gave the highest average strain capacity was selected as the mix that will be used throughout all the tests to quantify the cracking behaviour of SHCC.

In this appendix the different mixes that were used during the mix design process will be given and also the graphs indicating the stress-strain responses of the different mixes have been included.

A.2 Methodology

In this section the method used to design the different mixes is explained. Table A.1 gives a summary of the constituents and mix proportions that were used to prepare the different mixes. Mix 1 was the base mix from which all the other mixes were designed from. The mix proportions of the base mix were chosen from research that had been done on previous mixes. All the mixes had a water/cement ratio of 1. The add mixtures, namely the Super Plasticiser and Viscous Modification Agent, were added by increments of 0.2 % and 0.1 % of the cement weight, respectively. The add mixtures were increased with these given amounts until the right workability were found. Refer to Section 3.3 for the explanation on how the workability is determined. The proportions of the add mixtures for each mix is given in Table A.1. The cement volume in Mix 1 was decreased by a proportional amount to get the cement

volume for Mix 2. The cement volume that was decreased in the volume of Mix 1 was added to the volume of fly ash of Mix 1 to get the volume of fly ash for Mix 2. The cement volume in Mix 1 was increased by an amount to get the cement volume for Mix 3. The volume that was increased in the cement volume of Mix 3 was deducted from the volume of fly ash of Mix 1 to get the volume of fly ash required for Mix 3. The percentage of fibres used in Mix 1, 2 and 3 was 2 % of the total volume of the mix. In Mix 4 and 5 the proportions are the same as the base mix (Mix 1), but the percentage of fibres was increased to 2.2 % and 2.4 % respectively.

Table A.1: Summary of constituents and mix proportions for the different mixes

Constituents	Type	Mix 1 Kg/m³	Mix 2 Kg/m³	Mix 3 Kg/m³	Mix 4 Kg/m³	Mix 5 Kg/m³
Cement	Portland CEM I 42.5N	350	320	380	350	350
Fly Ash	Ratio of 1 : 0.37 to mass of cement	769.78	860.76	678.81	769.78	769.78
Sand	Silica sand; Particle size < 600 µm; Silica Console sand no. 2	530	530	530	530	530
Water	-	350	320	380	350	350
Fibres	PVA-RECS 15; Length = 12 mm; Diameter = 40 µm;	26	26	26	28.6	31.2
Viscous Modification Agent	Aqua Beton	0.35	1.6	1	0.35	1.05
Super Plasticiser	Premia 310	0.7	2.27	1.5	1.05	2.1

A.3 Results

For each mix four dogbone specimens were cast and the specimens were tested at a tensile loading rate of 0.02 mm/s. Figures A.1 to A.5 show the stress-strain responses of the different mixes.

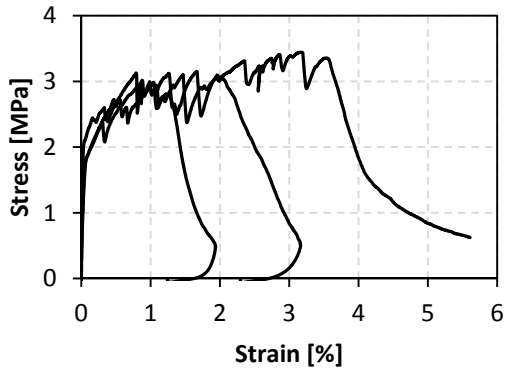


Figure A.1: Stress-strain response of Mix 1.

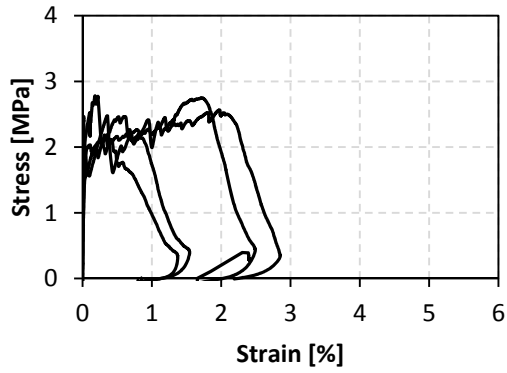


Figure A.2: Stress-strain response of Mix 2.

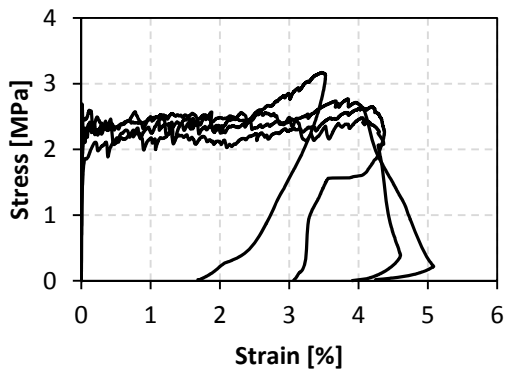


Figure A.3: Stress-strain response of Mix 3.

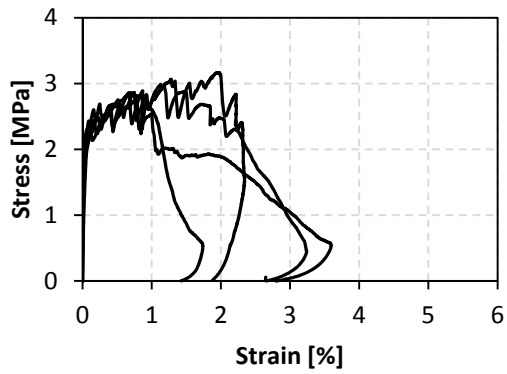


Figure A.4: Stress-strain response of Mix 4.

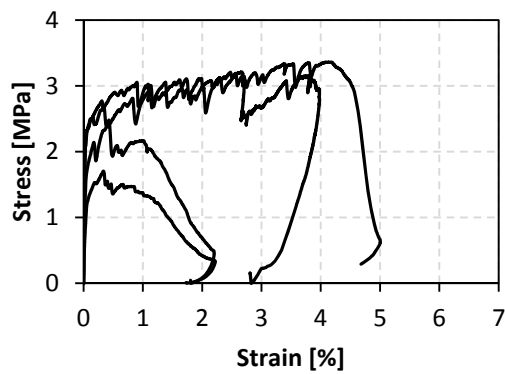


Figure A.5: Stress-strain response of Mix 5.

A.4 Discussion

In the stress-strain responses given in the previous section it can be seen that Mix 3 gave the highest strain capacity. Mix 3 was therefore selected as the mix that would be used to quantify the cracking behaviour of SHCC.

APPENDIX B

THE CRACKING BEHAVIOUR DATA FOR QUASI-STATIC TENSILE TESTS

B.1 Crack Width Data

B.1.1 Test 1

Table B.1: Summary of cracking data for test 1.

Test 1	Strain [%]					
	0.3	0.6	1	1.5	2	2.5
No. Cracks on section lines	25.00	46.00	101.00	158.00	206.00	263.00
Avg. No. Cracks	5.00	9.20	20.20	31.60	41.20	52.60
No. of cracks/m	68.41	125.88	276.39	432.38	563.73	719.72
Avg. Crack Width [μm]	29.60	33.44	31.97	32.37	32.31	32.53
Standard deviation [μm]	6.86	11.78	14.45	14.69	14.34	14.08
Skewness [μm^3]	0.81	1.73	2.92	3.85	4.79	5.14

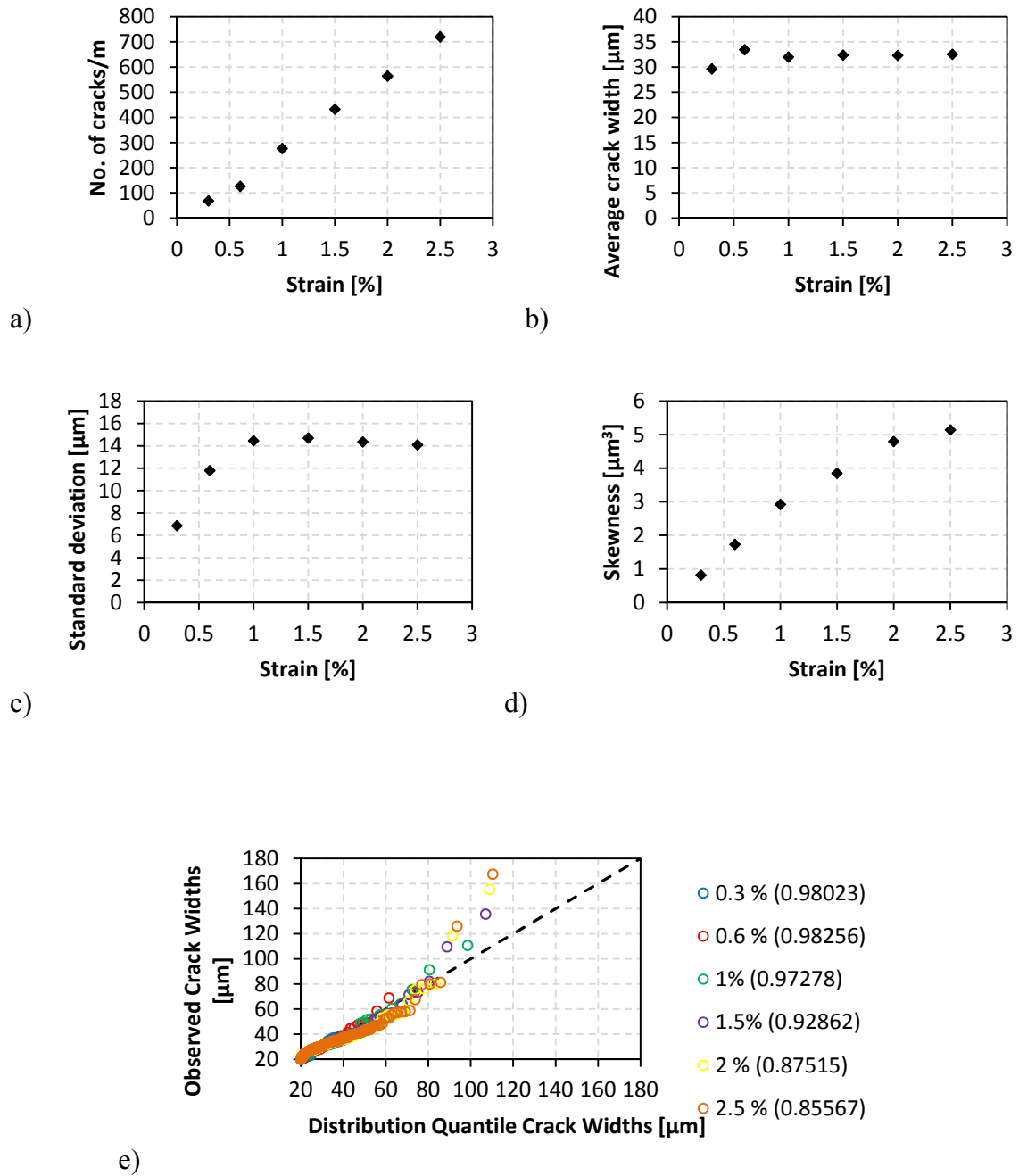


Figure B.1: a) The number of cracks per meter against the tensile strain for test 1, b) The average crack width against the tensile strain for test 1, c) The standard deviation against the tensile strain for test 1, d) The skewness against the tensile strain for test 1, e) The Quantile-Quantile plots at the different tensile strain stages for test 1.

B.1.2 Test 2

Table B.2: Summary of cracking data for test 2.

Test 2	Strain [%]					
	0.3	0.6	1	1.5	2	2.5
No. Cracks on section lines	22.00	58.00	91.00	140.00	192.00	251.00
Avg. No. Cracks	4.40	11.60	18.20	28.00	38.40	50.20
No. of cracks/m	60.21	158.73	249.04	383.13	525.44	686.91
Avg. Crack Width [μm]	30.94	31.79	35.20	35.21	34.17	34.47
Standard deviation [μm]	10.84	8.85	10.69	11.41	11.15	11.06
Skewness [μm^3]	1.59	1.38	1.15	1.11	1.45	1.51

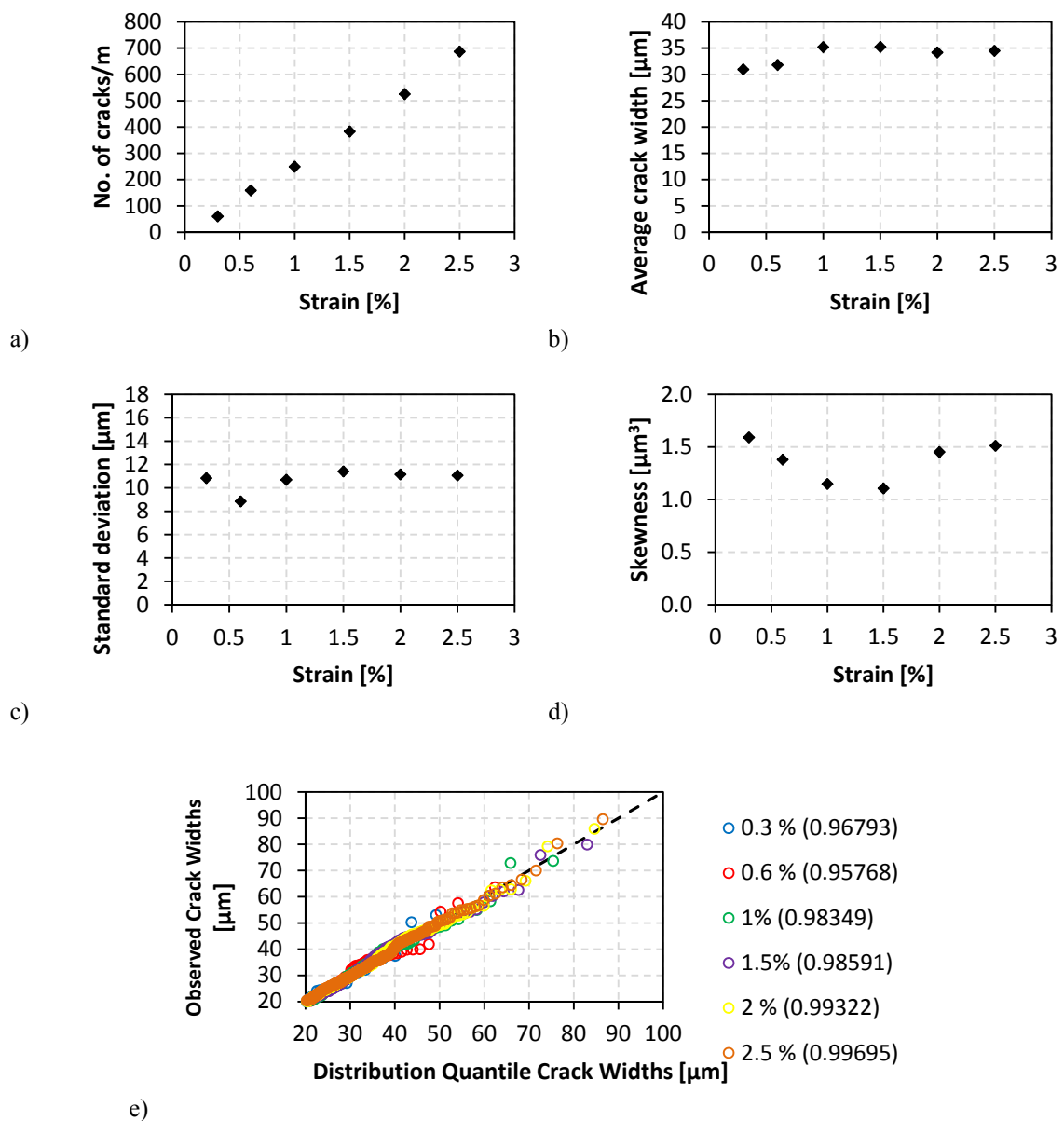
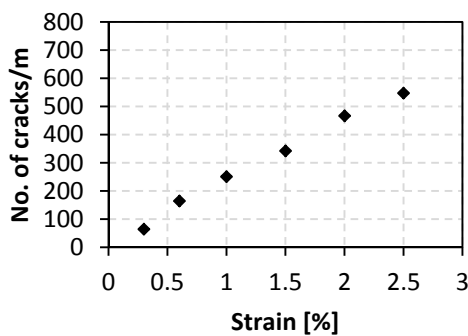


Figure B.2: The number of cracks per meter against the tensile strain for test 2, b) The average crack width against the tensile strain for test 2, c) The standard deviation against the tensile strain for test 2, d) The skewness against the tensile strain for test 2, e) The Quantile-Quantile plots at the different tensile strain stages for test 2.

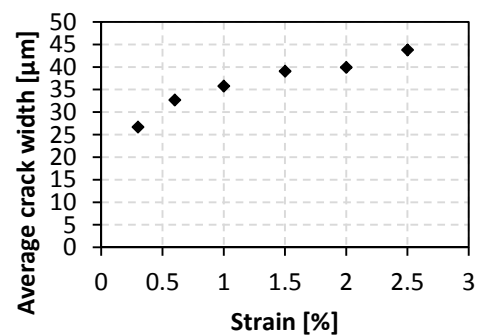
B.1.3 Test 3

Table B.3: Summary of cracking data for test 3.

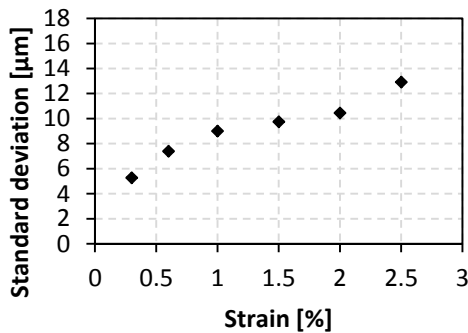
Test 3	Strain [%]					
	0.3	0.6	1	1.5	2	2.5
No. Cracks on section lines	24	61	93	127	173	203
Avg. No. Cracks	4.8	12.2	18.6	25.4	34.6	40.6
No. of cracks/m	64.731	164.5247	250.8328	342.5351	466.6029	547.5167
Avg. Crack Width [μm]	26.6918	32.68762	35.76453	39.06952	39.925	43.82061
Standard deviation [μm]	5.27899	7.396804	9.004576	9.747323	10.4521	12.92265
Skewness [μm^3]	0.89241	0.509589	0.456439	0.505784	0.730964	1.007051



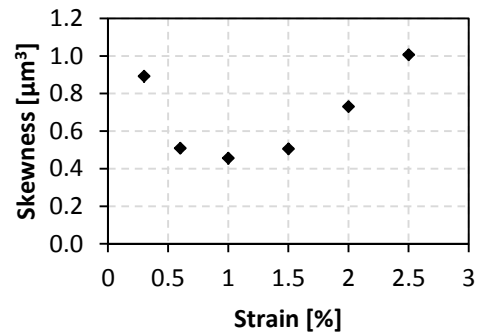
a)



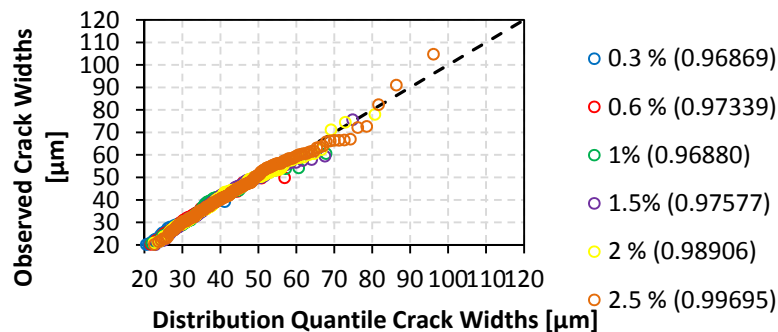
b)



c)



d)



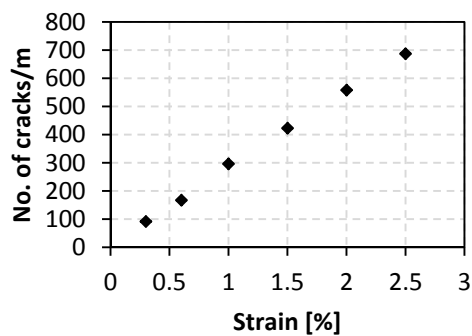
e)

Figure B.3: a) The number of cracks per meter against the tensile strain for test 3, b) The average crack width against the tensile strain for test 3, c) The standard deviation against the tensile strain for test 3, d) The skewness against the tensile strain for test 3, e) The Quantile-Quantile plots at the different tensile strain stages for test 3.

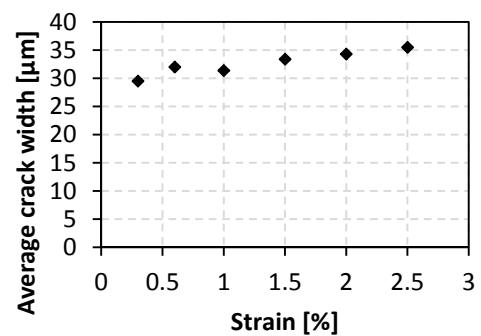
B.1.4 Test 4

Table B.4: Summary of cracking data for test 4.

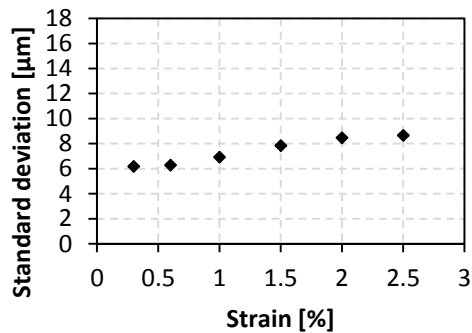
Test 4	Strain [%]					
	0.3	0.6	1	1.5	2	2.5
No. Cracks on section lines	34	62	110	157	207	255
Avg. No. Cracks	6.8	12.4	22	31.4	41.4	51
No. of cracks/m	91.6697	167.1625	296.5786	423.2985	558.1069	687.523
Avg. Crack Width [μm]	29.5129	31.99883	31.3667	33.39905	34.29979	35.49693
Standard deviation [μm]	6.18188	6.290325	6.930526	7.843601	8.467845	8.663718
Skewness [μm^3]	0.74516	0.35701	0.564047	0.304847	0.6648	0.663379



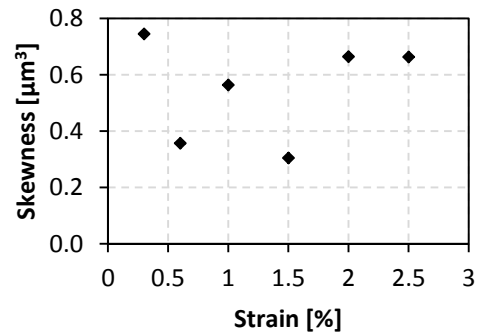
a)



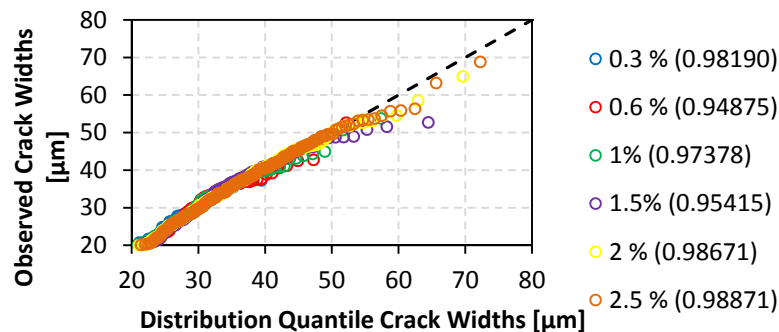
b)



c)



d)



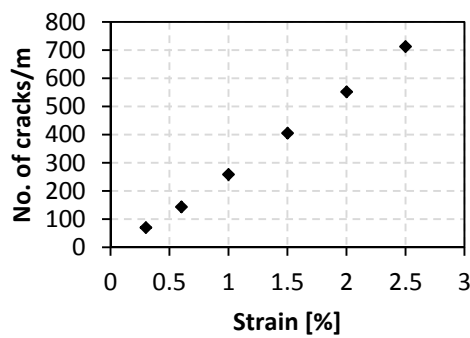
e)

Figure B.4: a) The number of cracks per meter against the tensile strain for test 4, b) The average crack width against the tensile strain for test 4, c) The standard deviation against the tensile strain for test 4, d) The skewness against the tensile strain for test 4, e) The Quantile-Quantile plots at the different tensile strain stages for test 4.

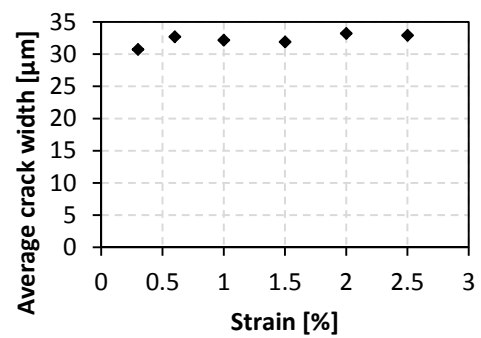
B.1.5 Test 5

Table B.5: Summary of cracking data for test 5.

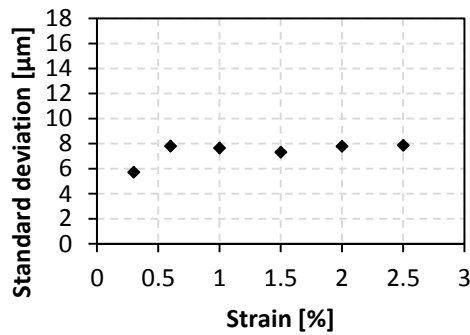
Test 5	Strain [%]					
	0.3	0.6	1	1.5	2	2.5
No. Cracks on section lines	25	51	92	144	196	253
Avg. No. Cracks	5	10.2	18.4	28.8	39.2	50.6
No. of cracks/m	70.4247	143.6663	259.1628	405.6461	552.1295	712.6977
Avg. Crack Width [μm]	30.7455	32.71352	32.18634	31.90655	33.23141	32.93258
Standard deviation [μm]	5.71904	7.810876	7.65338	7.3176	7.798286	7.874697
Skewness [μm^3]	0.79236	0.286154	0.704625	0.807384	0.736662	0.728559



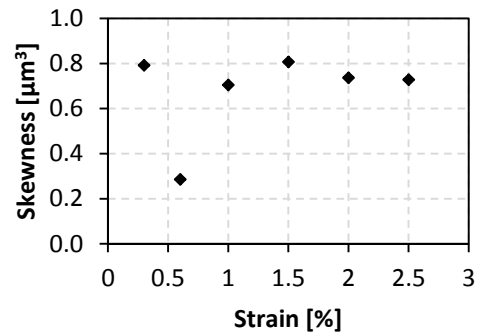
a)



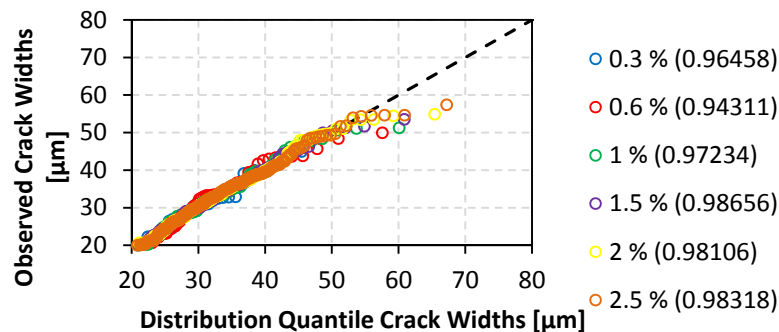
b)



c)



d)



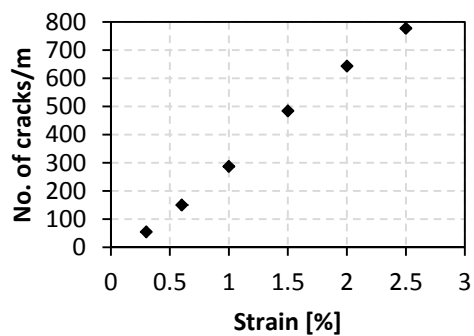
e)

Figure B.5: a) The number of cracks per meter against the tensile strain for test 5, b) The average crack width against the tensile strain for test 5, c) The standard deviation against the tensile strain for test 5, d) The skewness against the tensile strain for test 5, e) The Quantile-Quantile plots at the different tensile strain stages for test 5.

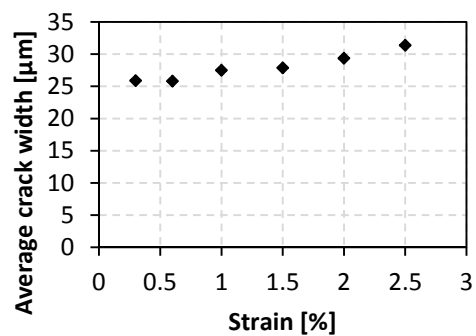
B.1.6 Test 6

Table B.6: Summary of cracking data for test 6.

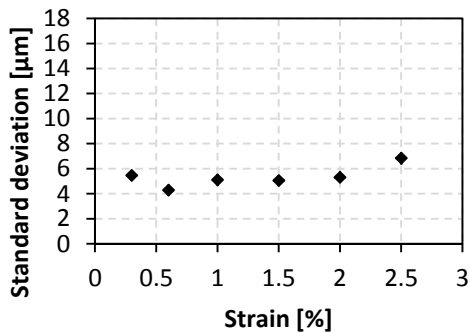
Test 6	Strain [%]					
	0.3	0.6	1	1.5	2	2.5
No. Cracks on section lines	20	55	105	177	235	284
Avg. No. Cracks	4	11	21	35.4	47	56.8
No. of cracks/m	54.7432	150.5438	287.4018	484.4773	643.2326	777.3534
Avg. Crack Width [μm]	25.8835	25.80896	27.50604	27.87634	29.3772	31.37341
Standard deviation [μm]	5.46982	4.295172	5.103798	5.054936	5.319967	6.843837
Skewness [μm^3]	0.93859	1.016153	0.662337	0.763743	0.563319	1.797157



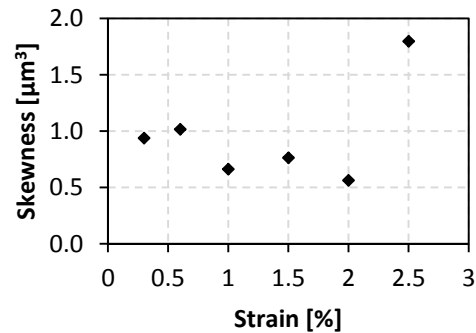
a)



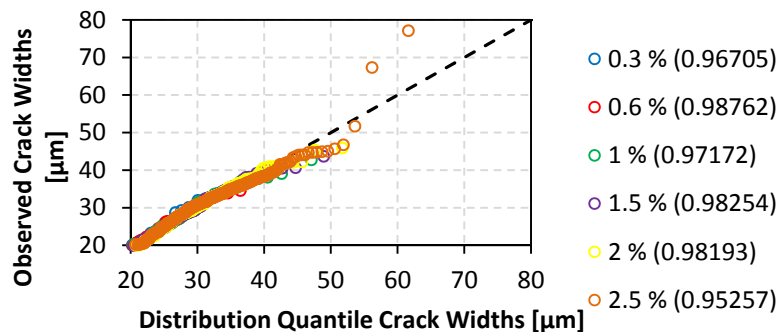
b)



c)



d)



e)

Figure B.6: a) The number of cracks per meter against the tensile strain for test 6, b) The average crack width against the tensile strain for test 6, c) The standard deviation against the tensile strain for test 6, d) The skewness against the tensile strain for test 6, e) The Quantile-Quantile plots at the different tensile strain stages for test 6.

B.1.7 Test 7

Table B.7: Summary of cracking data for test 7.

Test 7	Strain [%]					
	0.3	0.6	1	1.5	2	2.5
No. Cracks on section lines	31	66	96	155	222	276
Avg. No. Cracks	6.2	13.2	19.2	31	44.4	55.2
No. of cracks/m	82.427	175.4897	255.2578	412.135	590.2837	733.8662
Avg. Crack Width [μm]	32.4423	30.82741	35.22343	33.81209	32.2589	32.76553
Standard deviation [μm]	8.66208	8.458011	7.909575	7.98334	8.004049	7.689108
Skewness [μm^3]	0.80755	1.096965	0.916308	0.827556	0.96441	0.93465

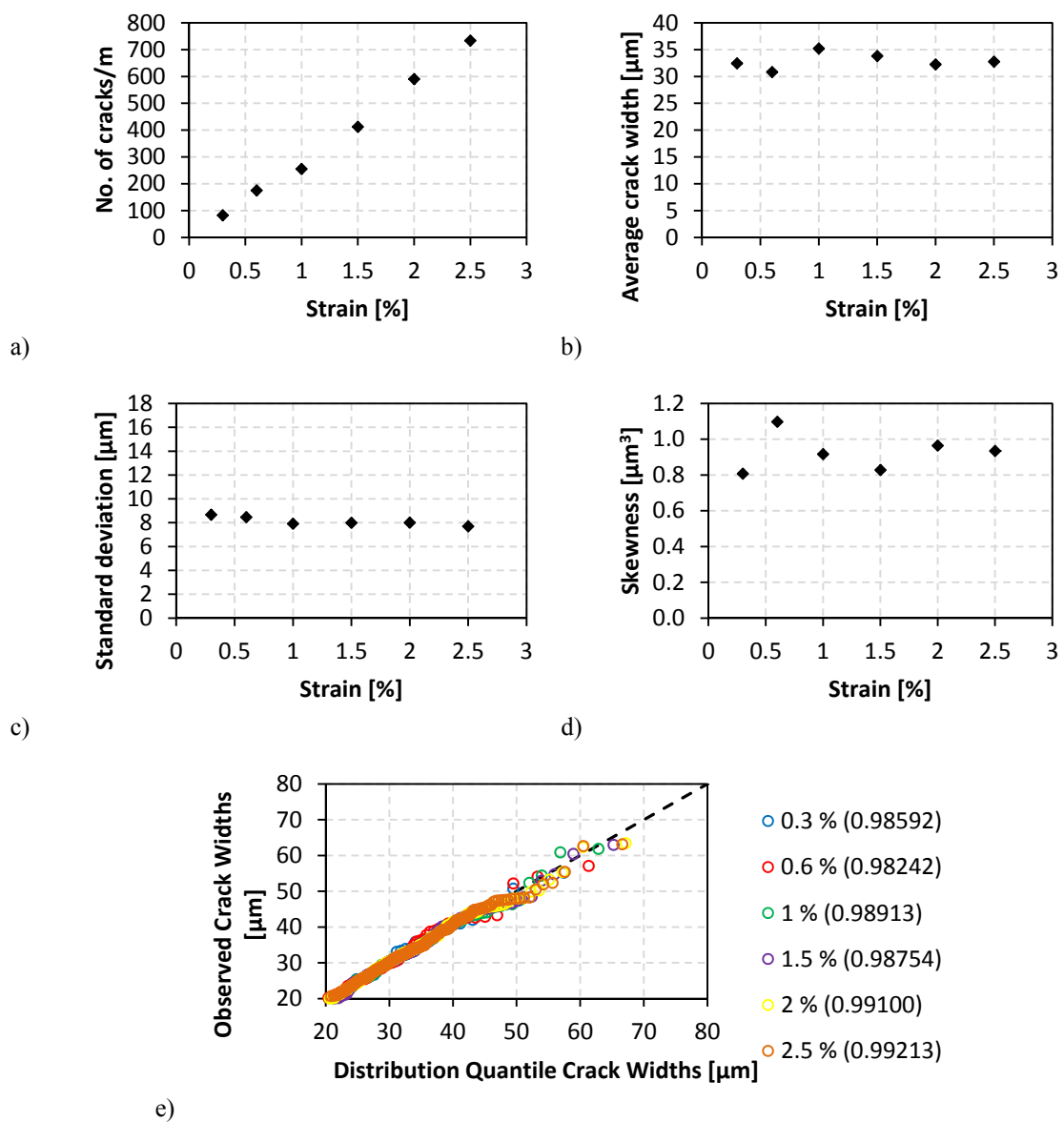


Figure B.7: a) The number of cracks per meter against the tensile strain for test 7, b) The average crack width against the tensile strain for test 7, c) The standard deviation against the tensile strain for test 7, d) The skewness against the tensile strain for test 7, e) The Quantile-Quantile plots at the different tensile strain stages for test 7.

B.1.8 Test 8

Table B.8: Summary of cracking data for test 8.

Test 8	Strain [%]					
	0.3	0.6	1	1.5	2	2.5
No. Cracks on section lines	11	35	67	98	141	179
Avg. No. Cracks	2.2	7	13.4	19.6	28.2	35.8
No. of cracks/m	34.1043	108.5136	207.7261	303.8381	437.1549	554.9696
Avg. Crack Width [μm]	40.6245	40.256	41.783	40.24727	38.28995	37.73244
Standard deviation [μm]	15.1354	21.78019	23.44295	23.92003	23.74799	22.30676
Skewness [μm^3]	0.60843	2.128519	2.94769	3.54687	4.171429	4.430929

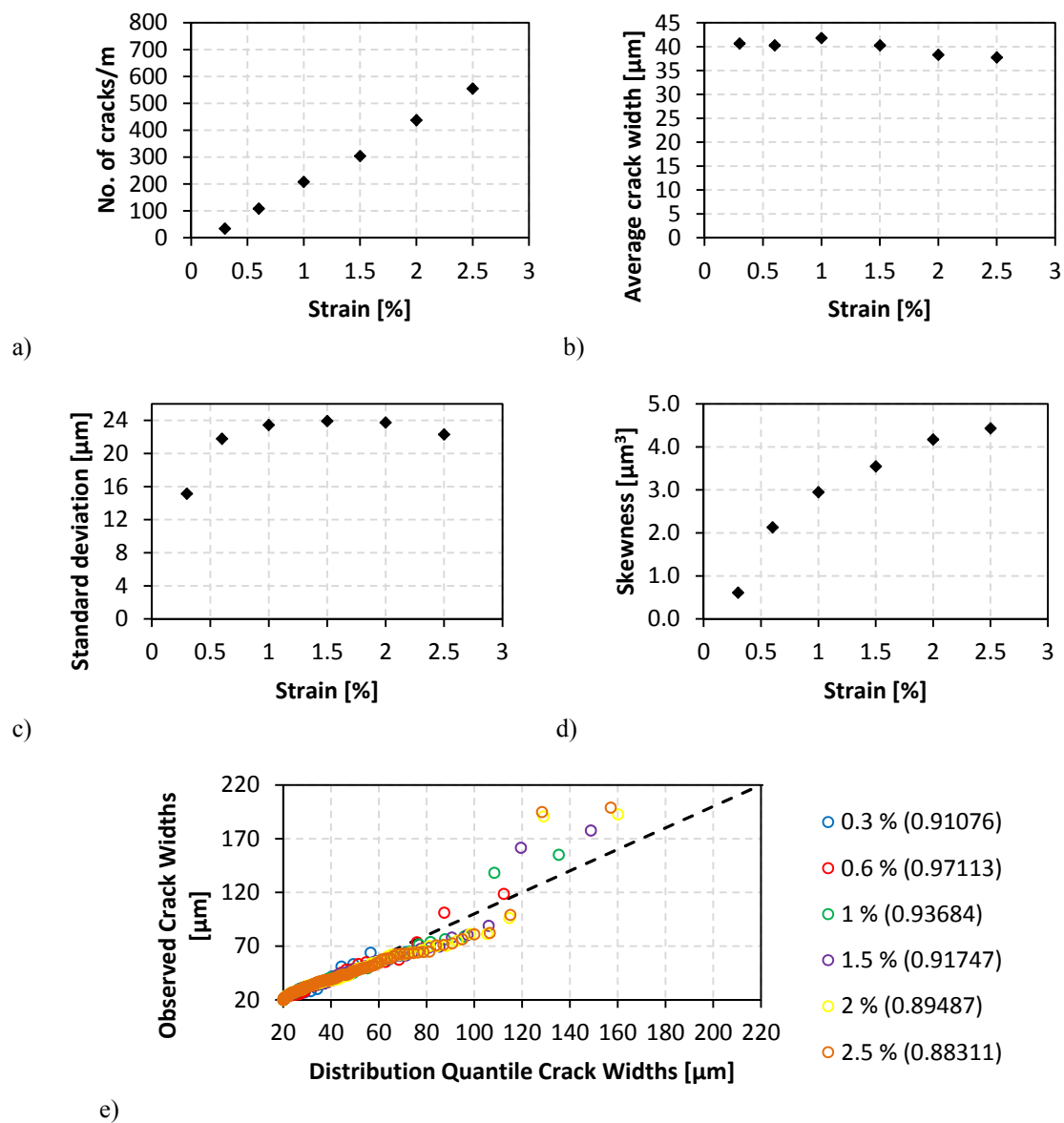


Figure B.8: a) The number of cracks per meter against the tensile strain for test 8, b) The average crack width against the tensile strain for test 8, c) The standard deviation against the tensile strain for test 8, d) The skewness against the tensile strain for test 8, e) The Quantile-Quantile plots at the different tensile strain stages for test 8.

B.1.9 Test 9

Table B.9: Summary of cracking data for test 9.

Test 9	Strain [%]					
	0.3	0.6	1	1.5	2	2.5
No. Cracks on section lines	29	54	94	155	206	255
Avg. No. Cracks	5.8	10.8	18.8	31	41.2	51
No. of cracks/m	81.9225	152.5453	265.5419	437.8616	581.9322	720.353
Avg. Crack Width [μm]	29.3175	29.52565	29.95096	30.97619	31.61384	32.12825
Standard deviation [μm]	7.13553	6.440465	6.57455	6.786435	6.568524	6.918368
Skewness [μm^3]	1.04338	0.767049	0.712246	0.705795	0.70937	0.637055

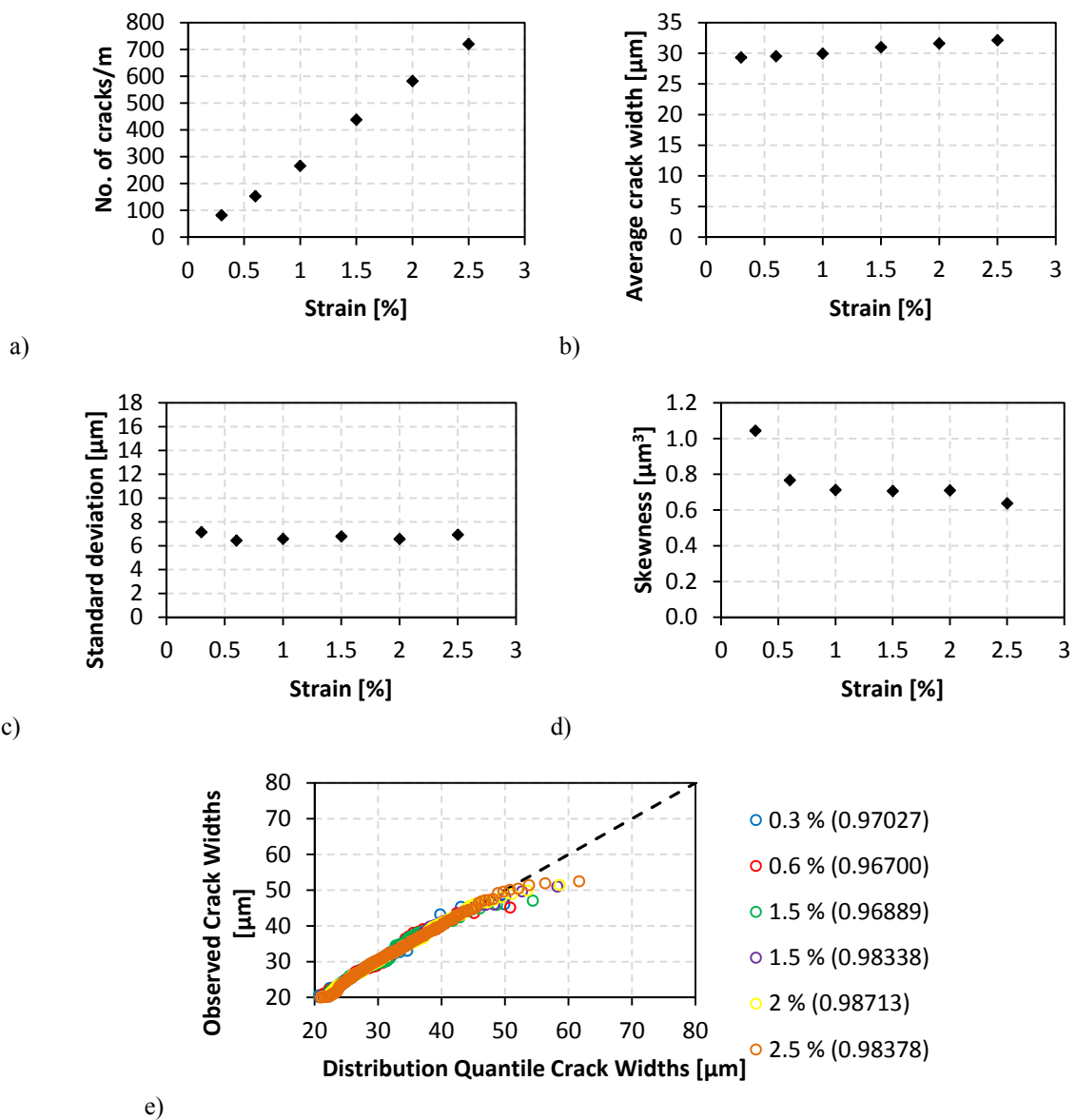


Figure B.9: a) The number of cracks per meter against the tensile strain for test 9, b) The average crack width against the tensile strain for test 9, c) The standard deviation against the tensile strain for test 9, d) The skewness against the tensile strain for test 9, e) The Quantile-Quantile plots at the different tensile strain stages for test 9.

B.1.10 Test 10

Table B.10: Summary of cracking data for test 10.

Test 10	Strain [%]					
	0.3	0.6	1	1.5	2	2.5
No. Cracks on section lines	18	59	98	151	197	253
Avg. No. Cracks	3.6	11.8	19.6	30.2	39.4	50.6
No. of cracks/m	48.6914	159.5997	265.0979	408.4671	532.9008	684.3853
Avg. Crack Width [μm]	27.4372	30.40883	32.55211	33.85876	35.20505	34.27501
Standard deviation [μm]	6.2422	6.889771	7.329374	7.775857	8.750709	9.803798
Skewness [μm^3]	1.33657	0.986238	0.664662	0.775125	0.733739	1.15842

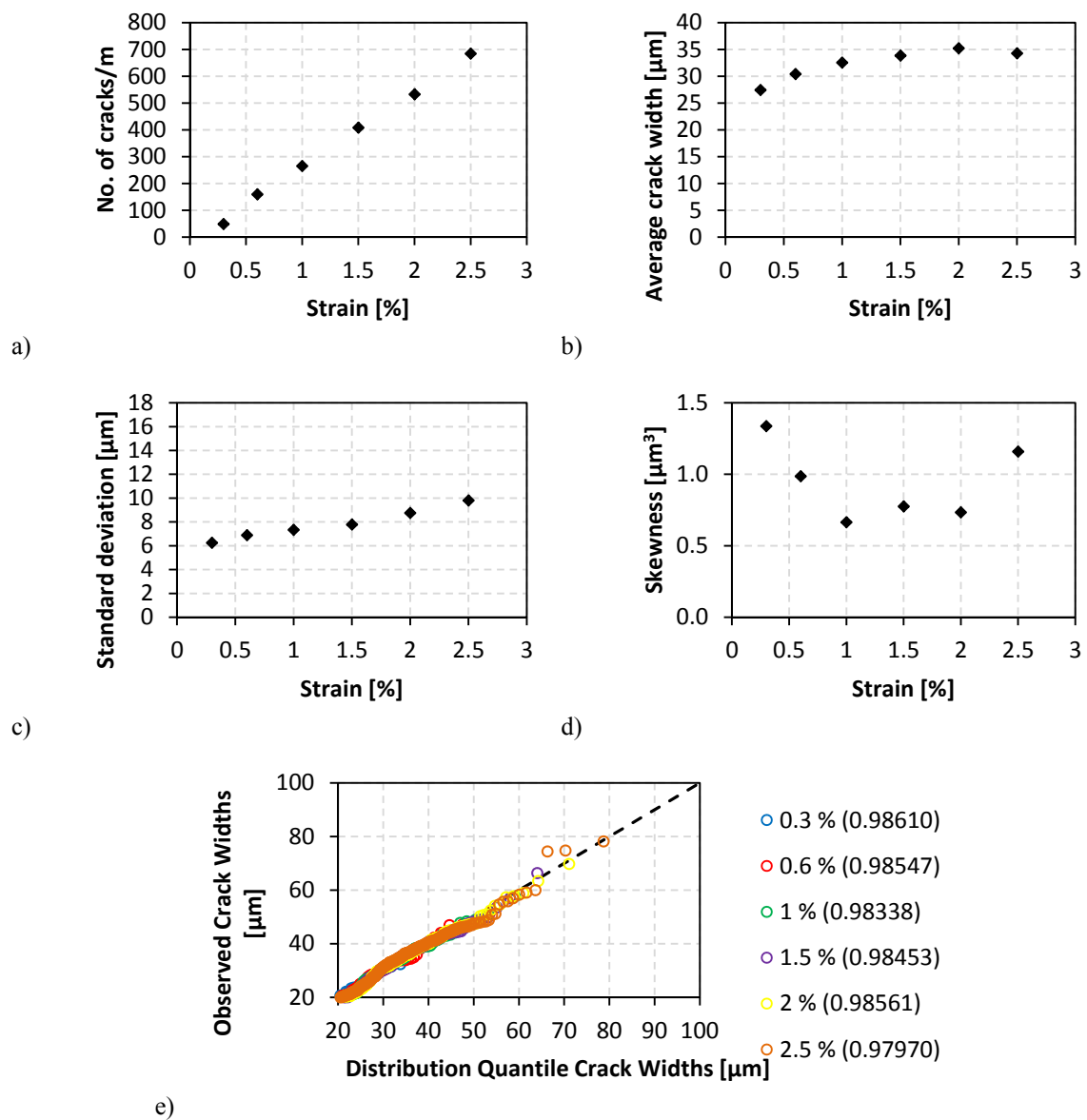


Figure B.10: a) The number of cracks per meter against the tensile strain for test 10, b) The average crack width against the tensile strain for test 10, c) The standard deviation against the tensile strain for test 10, d) The skewness against the tensile strain for test 10, e) The Quantile-Quantile plots at the different tensile strain stages for test 10.

B.1.11 Test 11

Table B.11: Summary of cracking data for test 11.

Test 11	Strain [%]					
	0.3	0.6	1	1.5	2	2.5
No. Cracks on section lines	32	50	71	105	126	153
Avg. No. Cracks	6.4	10	14.2	21	25.2	30.6
No. of cracks/m	91.7575	143.3711	203.587	301.0793	361.2952	438.7156
Avg. Crack Width [μm]	30.8496	39.98799	47.84508	48.72861	51.27492	50.65386
Standard deviation [μm]	8.75528	18.49031	22.05361	23.01426	26.02352	26.83439
Skewness [μm^3]	1.12438	1.183819	0.936196	1.333656	1.194055	1.375315

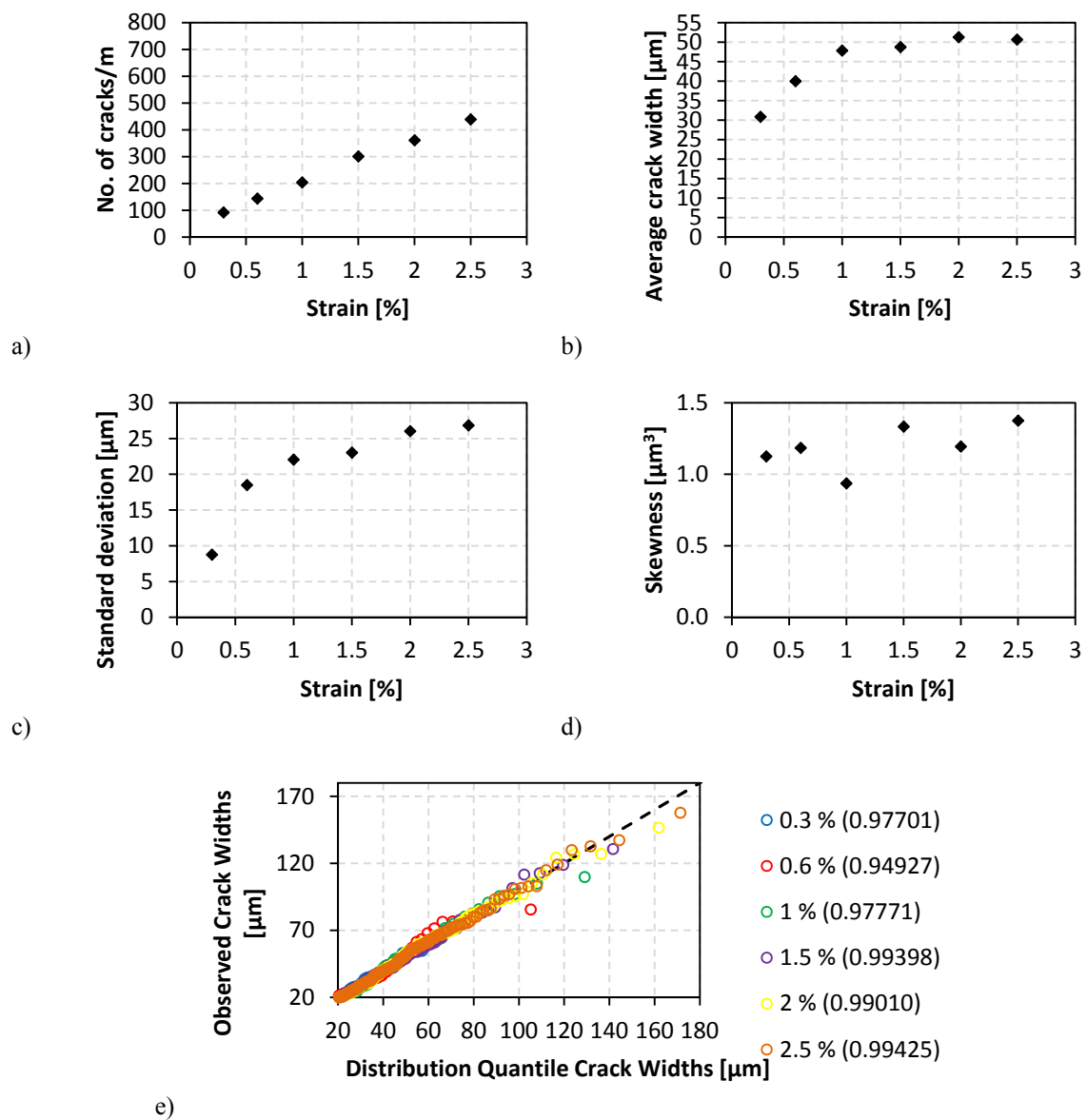


Figure B.11: a) The number of cracks per meter against the tensile strain for test 11, b) The average crack width against the tensile strain for test 11, c) The standard deviation against the tensile strain for test 11, d) The skewness against the tensile strain for test 11, e) The Quantile-Quantile plots at the different tensile strain stages for test 11.

B.1.12 Test 12

Table B.12: Summary of cracking data for test 12.

Test 12	Strain [%]					
	0.3	0.6	1	1.5	2	2.5
No. Cracks on section lines	20	39	69	113	155	190
Avg. No. Cracks	4	7.8	13.8	22.6	31	38
No. of cracks/m	63.0627	122.9722	217.5662	356.304	488.7356	599.0953
Avg. Crack Width [μm]	37.5857	41.01188	39.80535	37.61535	38.16468	39.5456
Standard deviation [μm]	11.5265	14.02586	12.70434	11.79705	11.77307	12.12627
Skewness [μm^3]	0.34096	0.630338	0.797252	0.884092	0.67967	0.591196

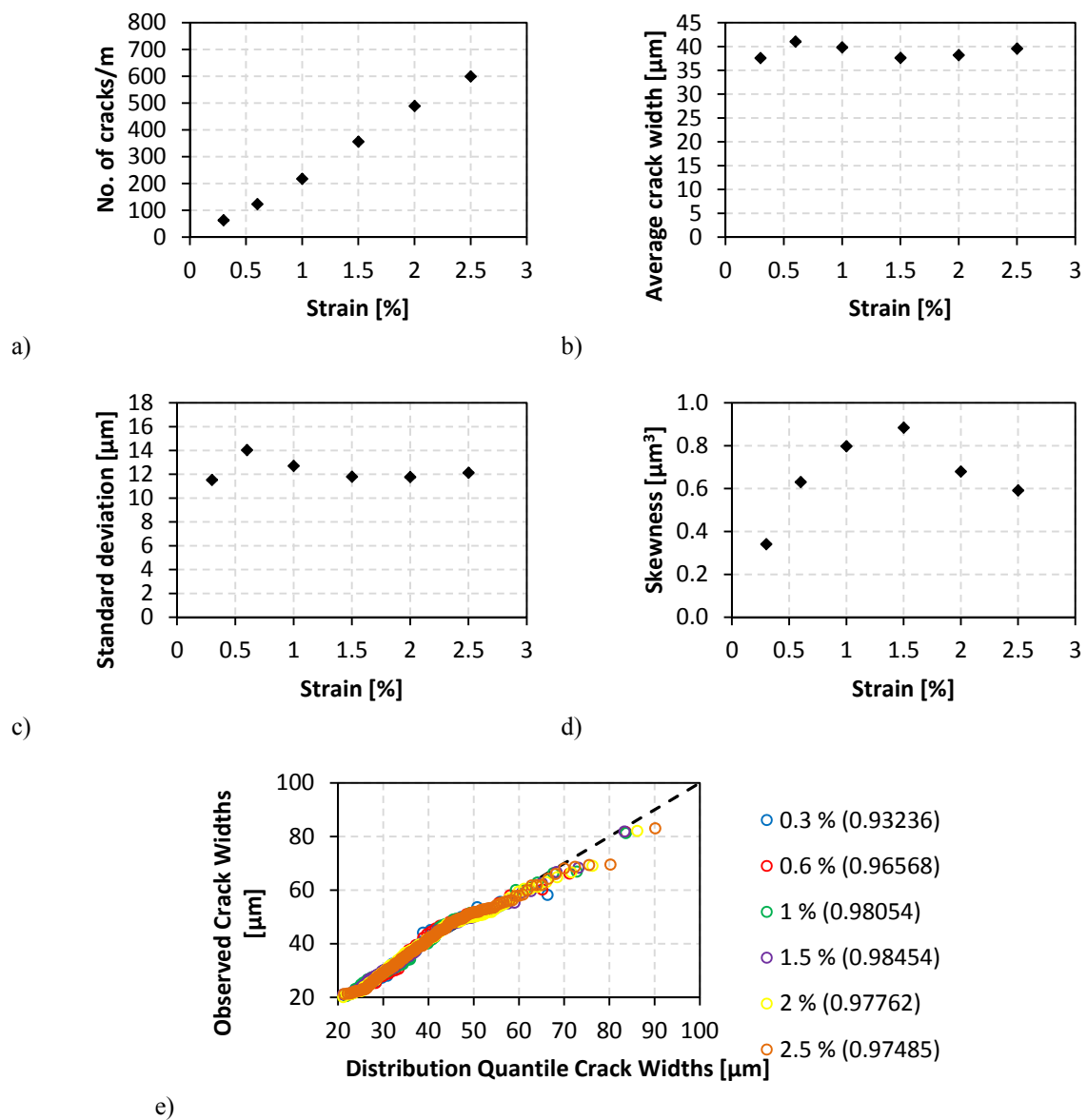


Figure B.12: a) The number of cracks per meter against the tensile strain for test 12, b) The average crack width against the tensile strain for test 12, c) The standard deviation against the tensile strain for test 12, d) The skewness against the tensile strain for test 12, e) The Quantile-Quantile plots at the different tensile strain stages for test 12.

B.1.13 Test 13

Table B.13: Summary of cracking data for test 13.

Test 13	Strain [%]					
	0.3	0.6	1	1.5	2	2.5
No. Cracks on section lines	18	40	60	90	130	171
Avg. No. Cracks	3.6	8	12	18	26	34.2
No. of cracks/m	52.6182	116.9294	175.3941	263.0911	380.0205	499.8731
Avg. Crack Width [μm]	32.1591	42.82007	46.01937	45.22404	44.26694	44.45337
Standard deviation [μm]	6.11087	21.61581	26.91084	30.57914	33.63573	33.58607
Skewness [μm^3]	-0.2411	1.736307	1.862747	2.201692	2.983984	3.582905

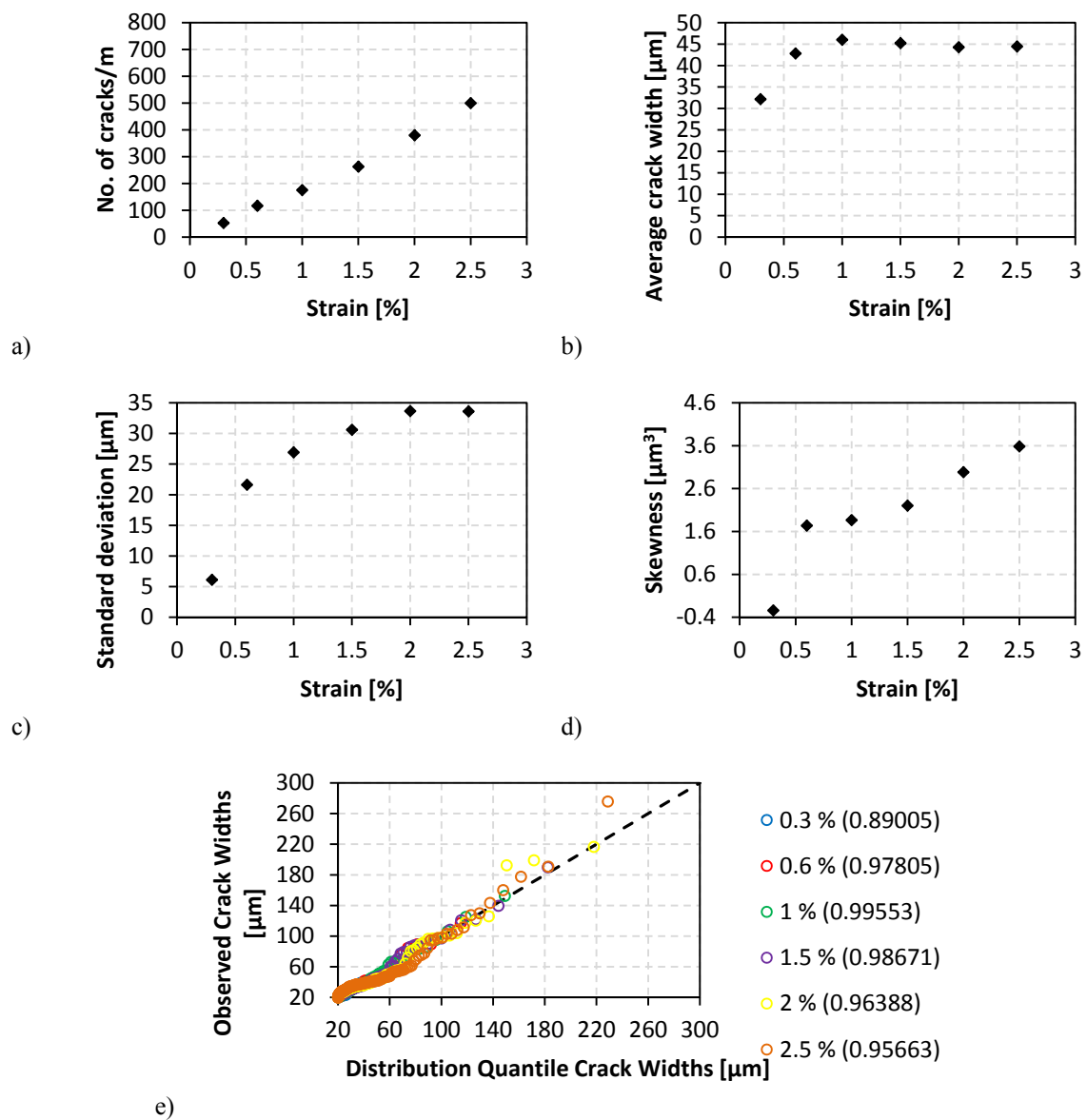


Figure B.13: a) The number of cracks per meter against the tensile strain for test 13, b) The average crack width against the tensile strain for test 13, c) The standard deviation against the tensile strain for test 13, d) The skewness against the tensile strain for test 13, e) The Quantile-Quantile plots at the different tensile strain stages for test 13.

B.1.14 Test 14

Table B.14: Summary of cracking data for test 14.

Test 14	Strain [%]					
	0.3	0.6	1	1.5	2	2.5
No. Cracks on section lines	16	41	79	127	158	187
Avg. No. Cracks	3.2	8.2	15.8	25.4	31.6	37.4
No. of cracks/m	45.197	115.8172	223.16	358.7509	446.32	528.2395
Avg. Crack Width [μm]	27.3845	36.6165	37.292	38.46249	41.66715	44.85279
Standard deviation [μm]	3.72202	12.36041	14.81249	15.4417	17.11492	19.83594
Skewness [μm^3]	0.35528	0.510457	1.075004	1.436104	1.195777	1.160852

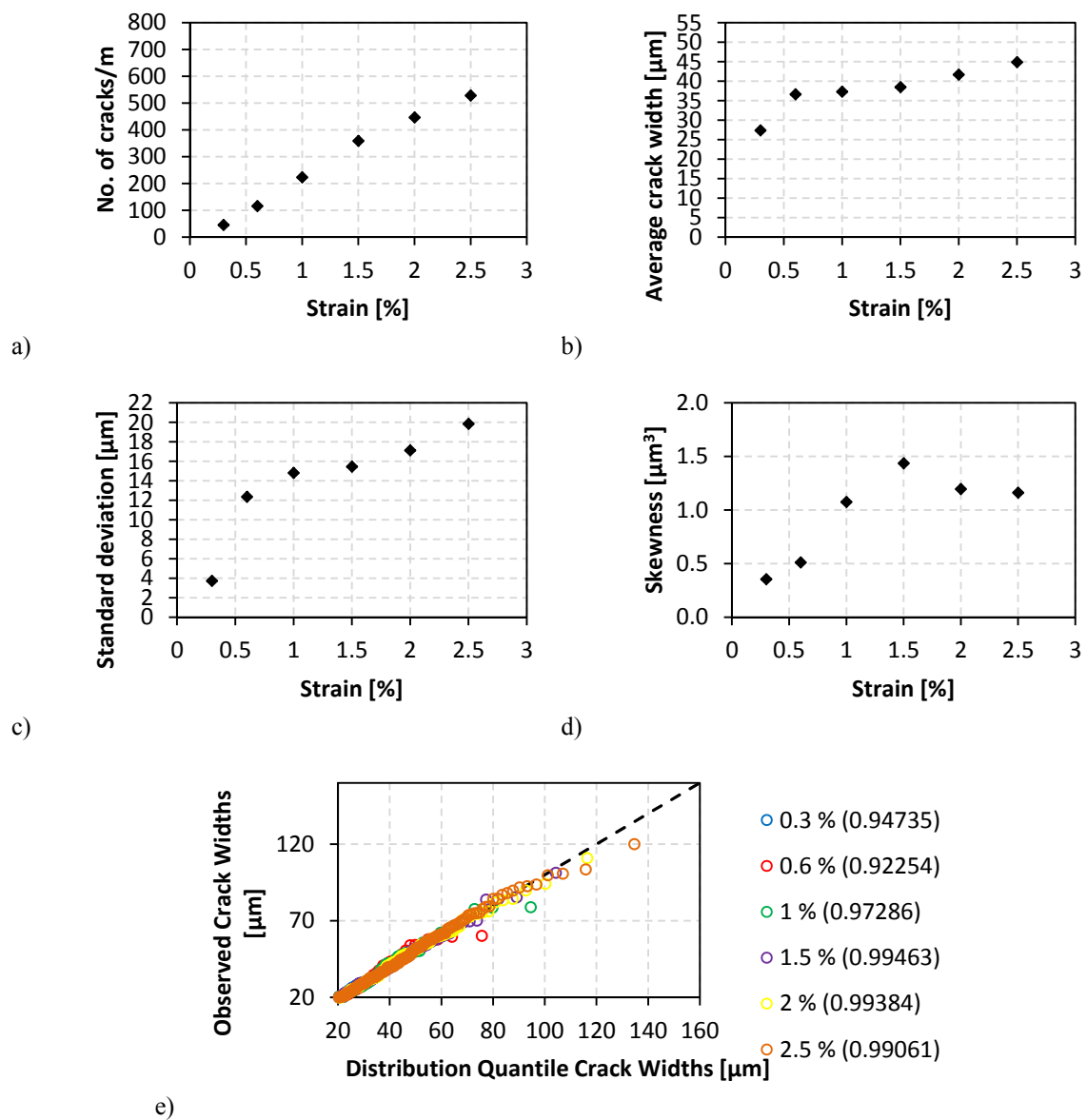


Figure B.14: a) The number of cracks per meter against the tensile strain for test 14, b) The average crack width against the tensile strain for test 14, c) The standard deviation against the tensile strain for test 14, d) The skewness against the tensile strain for test 14, e) The Quantile-Quantile plots at the different tensile strain stages for test 14.

B.2 Crack Proximity Index Data

Table B.15: Summary of *CPI* data for all tests.

Test No.	Strain [%]					
	0.3	0.6	1	1.5	2	2.5
1	0.061793	0.07379	0.061283	0.068624	0.071872	0.075286
2	0.030427	0.058188	0.075748	0.082624	0.08425	0.088772
3	0.051052	0.080874	0.081865	0.090541	0.095509	0.10501
4	0.042318	0.053527	0.060664	0.071553	0.077219	0.083886
5	0.035046	0.054093	0.062364	0.066711	0.077464	0.081292
6	0.030289	0.038622	0.057397	0.062264	0.069344	0.078422
7	0.042122	0.05648	0.07191	0.072239	0.073196	0.075018
8	0.046645	0.087293	0.093424	0.089719	0.083969	0.081481
9	0.051405	0.041144	0.05124	0.062951	0.069003	0.073674
10	0.018313	0.051949	0.072927	0.082668	0.083911	0.080302
11	0.035777	0.051775	0.091297	0.101678	0.134434	0.12942
12	0.062848	0.073367	0.069529	0.072401	0.082349	0.08592
13	0.044402	0.065317	0.083133	0.092443	0.086307	0.094683
14	0.01199	0.045034	0.06313	0.076672	0.091362	0.095364

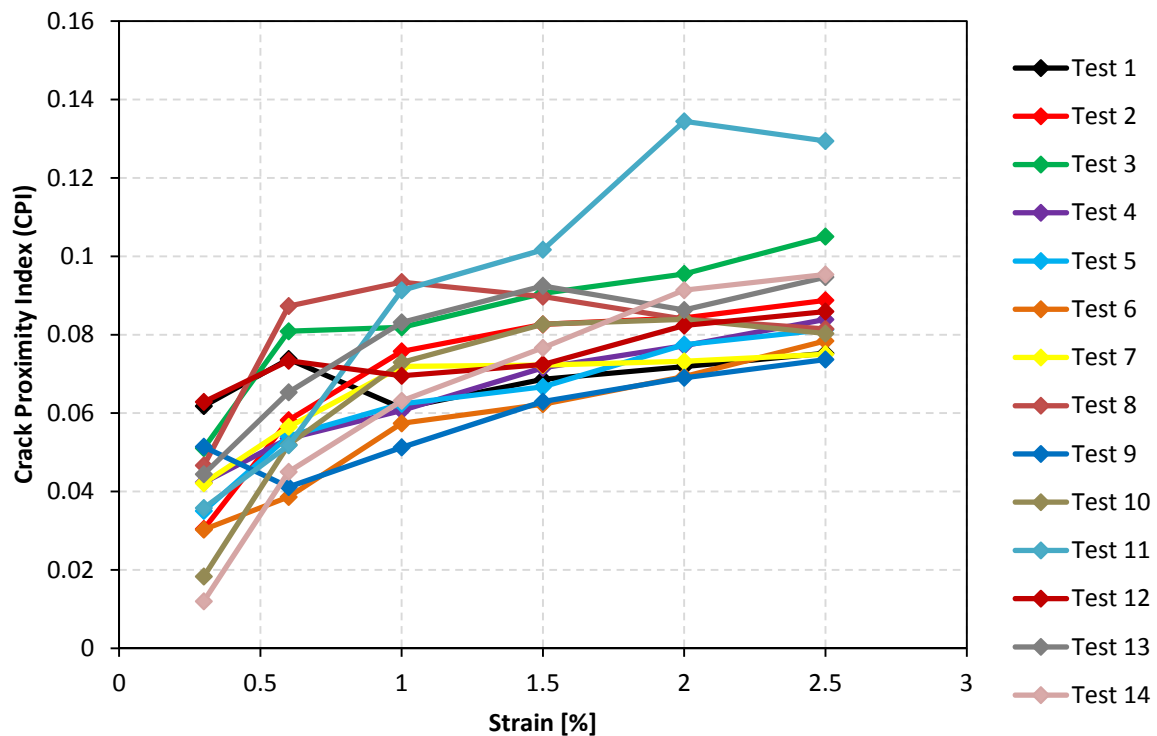


Figure B.15: *CPI* plots against the strain for all tests.

APPENDIX C

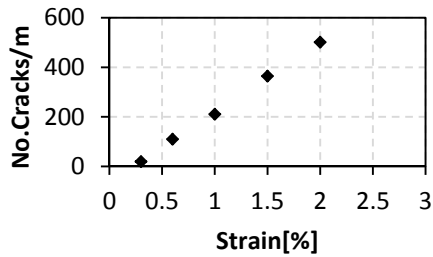
FOUR POINT BENDING RESULTS

C.1 Crack Width Data

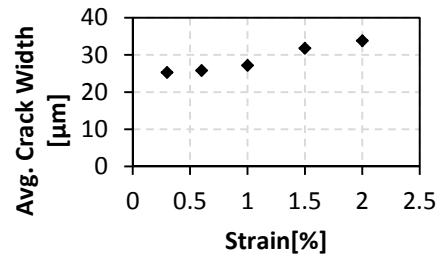
C.1.1 Test 1

Table C.1: Summary of cracking data for flexural test 1.

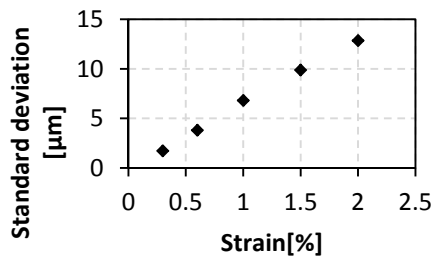
Test 1	Strain [%]				
	0.3	0.6	1	1.5	2
No. Cracks on section lines	6	33	63	109	150
Avg. No. Cracks	2	11	21	36.33333	50
No. of cracks/m	20.05637	110.3101	210.5919	364.3575	501.4094
Avg. Crack Width [μm]	25.30177	25.81616	27.18766	31.79154	33.81842
Standard deviation [μm]	1.720224	3.804694	6.80568	9.872476	12.83848
Skewness [μm^3]	-0.02261	0.455159	1.004527	1.13036	1.199382



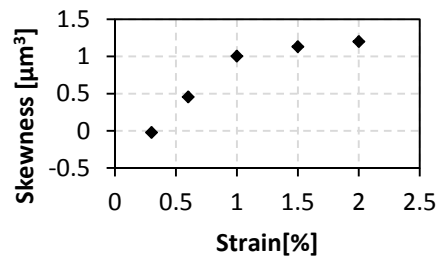
a)



b)



c)



d)

Figure C.1: a) The number of cracks per meter against the tensile strain for flexural test 1, b) The average crack width against the tensile strain for flexural test 1, c) The standard deviation against the tensile strain for flexural test 1, d) The skewness against the tensile strain for flexural test 1.

C.1.2 Test 2

Table C.2: Summary of cracking data for flexural test 2.

Test 2	Strain [%]					
	0.3	0.6	1	1.5	2	2.5
No. Cracks on section lines	6	30	45	80	108	148
Avg. No. Cracks	2	10	15	26.66667	36	49.333333
No. of cracks/m	27.57141	137.8571	206.7856	367.6188	496.2854	680.0949
Avg. Crack Width [μm]	23.74827	28.17465	31.56139	31.08784	33.11226	34.64707
Standard deviation [μm]	0.46453	7.448301	7.267784	9.096976	10.25236	13.09863
Skewness [μm^3]	0.854533	1.119816	0.020158	0.57855	1.007973	1.381172

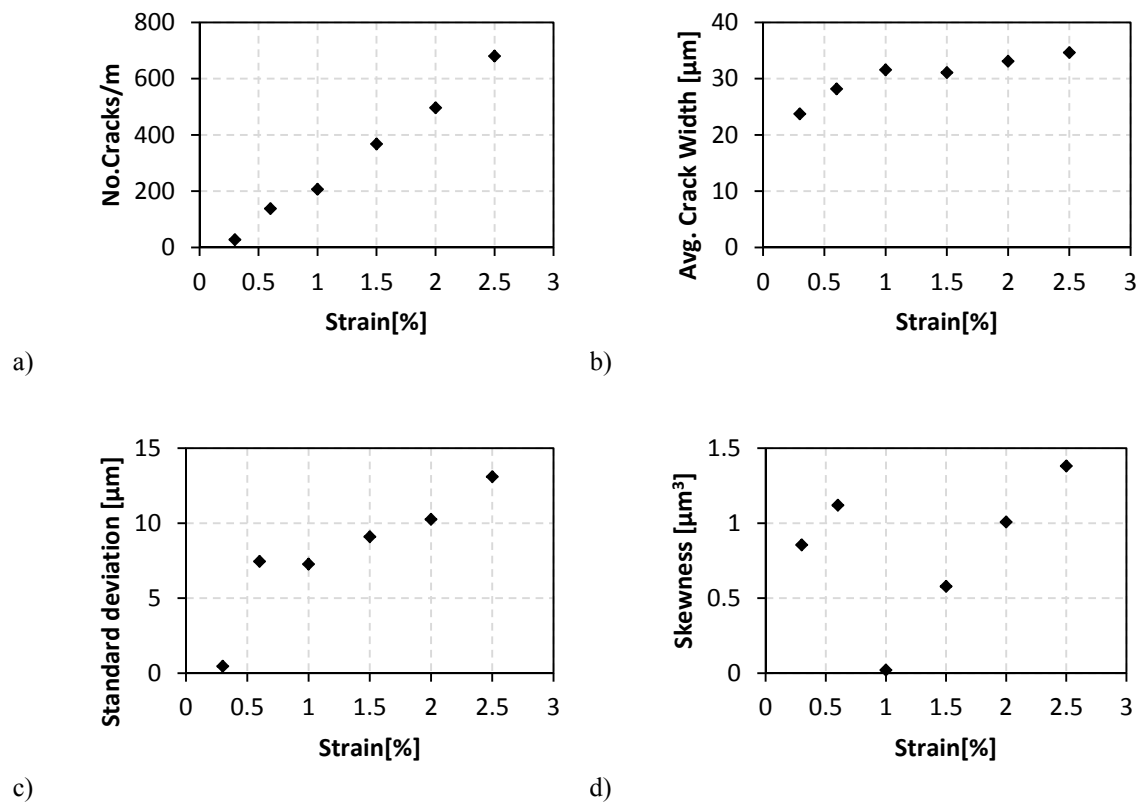
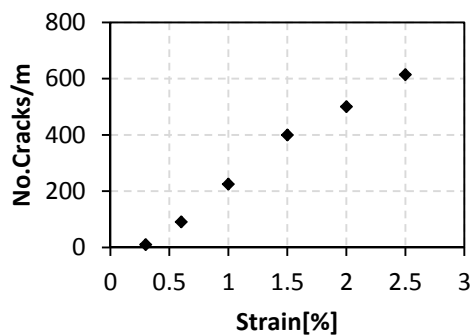


Figure C.2: a) The number of cracks per meter against the tensile strain for flexural test 2, b) The average crack width against the tensile strain for flexural test 2, c) The standard deviation against the tensile strain for flexural test 2, d) The skewness against the tensile strain for flexural test 2.

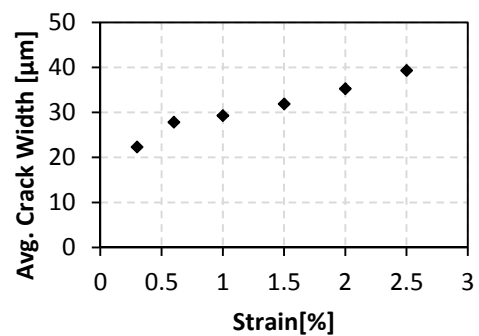
C.1.3 Test

Table C.3: Summary of cracking data for flexural test 3.

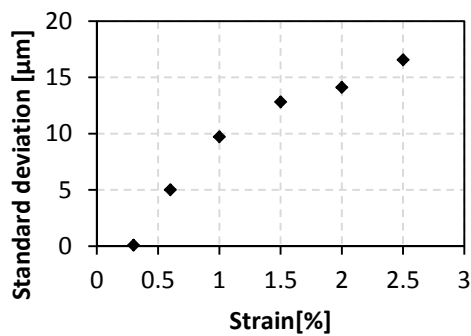
Test 3	Strain [%]					
	0.3	0.6	1	1.5	2	2.5
No. Cracks on section lines	3	27	67	119	149	183
Avg. No. Cracks	1	9	22.33333	39.66667	49.66667	61
No. of cracks/m	10.07078	90.63705	224.9141	399.4744	500.1822	614.3178
Avg. Crack Width [μm]	22.30963	27.80709	29.29871	31.87108	35.2668	39.30573
Standard deviation [μm]	0.08943	5.006604	9.715957	12.82035	14.11025	16.56208
Skewness [μm^3]	-0.332	0.189659	0.841562	1.398914	1.174458	1.073522



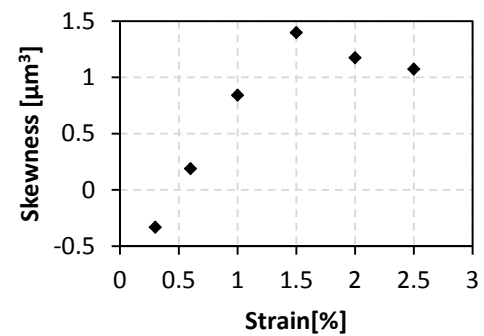
a)



b)



c)



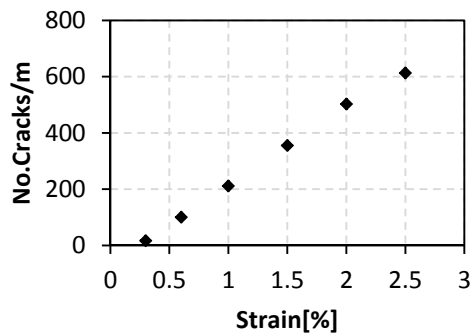
d)

Figure C.3: a) The number of cracks per meter against the tensile strain for flexural test 3, b) The average crack width against the tensile strain for flexural test 3, c) The standard deviation against the tensile strain for flexural test 3, d) The skewness against the tensile strain for flexural test 3.

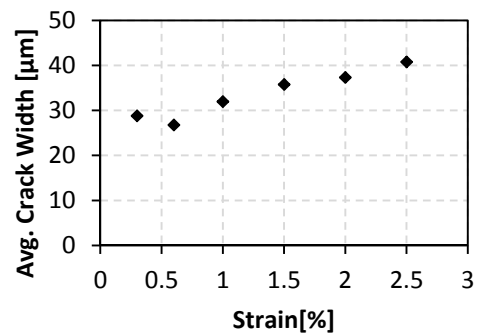
C.1.4 Test 4

Table C.4: Summary of cracking data for flexural test 4.

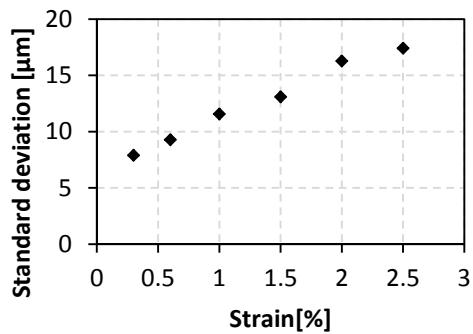
Test 4	Strain [%]					
	0.3	0.6	1	1.5	2	2.5
No. Cracks on section lines	5	30	63	106	150	183
Avg. No. Cracks	1.666667	10	21	35.333333	50	61
No. of cracks/m	16.74885	100.4931	211.0355	355.0756	502.4654	613.0078
Avg. Crack Width [μm]	28.79442	26.74446	31.95837	35.76684	37.33734	40.76714
Standard deviation [μm]	7.896834	9.273457	11.57289	13.09816	16.28305	17.41367
Skewness [μm^3]	-0.60855	2.435885	1.201722	0.973122	1.154093	1.127553



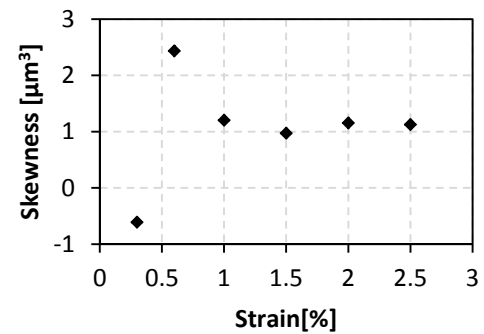
a)



b)



c)



d)

Figure C.4: a) The number of cracks per meter against the tensile strain for flexural test 4, b) The average crack width against the tensile strain for flexural test 4, c) The standard deviation against the tensile strain for flexural test 4, d) The skewness against the tensile strain for flexural test 4.

C.2 Crack Proximity Index Data

Table C.5: Summary of *CPI* data for all flexural tests.

Test No.	Strain [%]					
	0.3	0.6	1	1.5	2	2.5
1	2.53E-05	0.01796	0.031676	0.051788	0.063611	-
2	0.018272	0.027821	0.037912	0.048143	0.057109	0.072914
3	0	0.023472	0.030349	0.043567	0.05699	0.070652
4	0.02341	0.019749	0.045733	0.058507	0.066837	0.079247

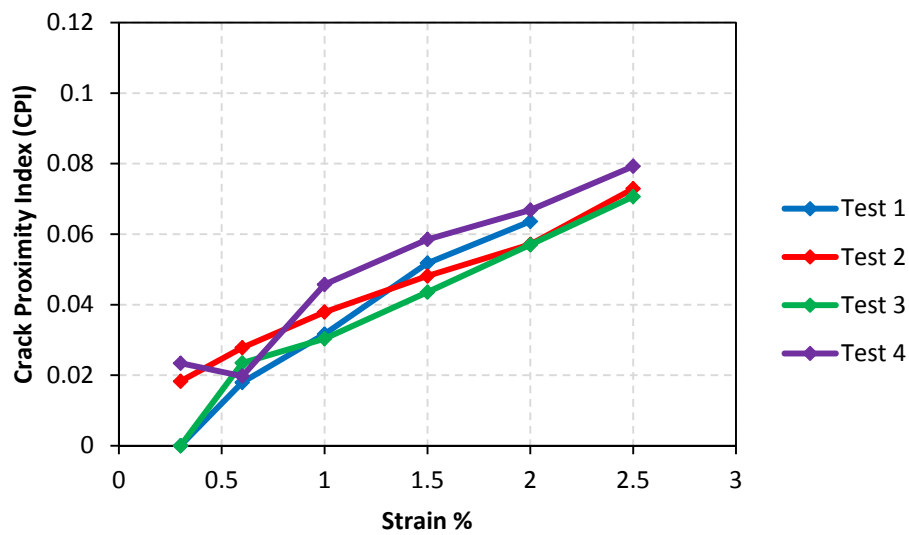


Figure C.5: *CPI* plots against the strain for all flexural tests.